ELECTROCHEMICAL AND MORPHOLOGICAL CHARACTERIZATION OF THE INTERFACE AT NEGATIVE ELECTRODES IN AQUEOUS METAL-ION BATTERIES

"GAS EVOLUTION & ELECTRODEPOSITION EFFICIENCY"

Vom Fachbereich Produktionstechnik
der
UNIVERSITÄT BREMEN

zur Erlangung des Grades
Doktor-Ingenieur
Genehmigte

Dissertation
von
M.Sc. Amir Bani Hashemi

Gutachter:
Prof. Fabio La Mantia
Prof. Mauro Pasta (University of Oxford)

Tag der mündlichen Prüfung: 23.01.2018

To Maryam,

the most precious treasure I have on earth.

Declaration

The work presented in this Ph.D. thesis was carried out during my doctoral studies from September 2014 to September 2017 in the group of Prof. Fabio La Mantia. Here I confirmed that:

- The work was carried out without any unauthorized third party assistance,

- No other sources or aids than the ones specified have been used,

- Those works/text passages which have been included word by word or by content accordingly from other sources have been indicated.

Date: 7. September 2017

Amir Bani Hashemi

Abstract

Providing a sufficient amount of energy is a primary problem for current and future societies. To achieve this goal, it is essential to expand the use of renewable energy sources such as the sun and wind, as soon as possible. These energy sources are inherently intermittent. Thus, appropriate grid-scale energy storage systems are required to store high amount of energy in a very short period of time. One possible choice for stationary applications in which volumetric and gravimetric energy densities are not primary factors is aqueous metal-ion batteries. Recently, aqueous zinc-ion batteries based on copper hexacyanoferrate with an average potential of 1.73 V have been developed. The main limiting factors for this new family of batteries include a low electrodeposition efficiency and hydrogen evolution on the negative electrode. These problems are related to the use of zinc as the negative electrode, in which the electrochemical reduction potential is sufficiently low that, at least thermodynamically, hydrogen evolution becomes favorable. Hydrogen evolution negatively influences the electrodeposition efficiency of the electrode and performance of the battery, hindering the power density, and lowering the overall energy efficiency. Therefore, decreasing the level of hydrogen evolution and increasing the electrodeposition efficiency are of primary importance in this type of battery.

In the first part of this dissertation, a new electrochemical cell was designed for *in-operando* characterization of gas evolution in batteries via differential electrochemical mass spectrometry (DEMS). Different parameters such as the position, size, and shape of the electrodes, flow of the carrier gas, contact between the current connectors and electrodes, sealing of the cell, and setup to run the DEMS measurements were all discussed. The performance of the cell for DEMS measurements was validated by investigating the gas evolution at the graphite electrode in an organic electrolyte. To do so, cyclic voltammetry (CV) was combined with the DEMS method. Moreover, the ability of the cell to perform electrochemical impedance spectroscopy (EIS) measurements was confirmed. Subsequently, the cell was used to study hydrogen evolution on negative electrodes in an aqueous zinc-ion battery based on Prussian blue derivatives. To accomplish this goal, galvanostatic cycling with potential limitation (GCPL) was combined with the DEMS method. The results showed that increasing the concentration of the electrolyte could suppress the level of hydrogen evolution.

The second part of this dissertation studied the morphology of zinc electrodeposition on the negative electrode at different current densities. Several constant current densities were applied and the surface morphology investigated via SEM and color 3D laser microscopy. The results showed that below the limiting current density, no preferential growth was observed on the surface of the electrode. However, above the limiting current density, large hexagonal crystals were formed all over the surface. Thereafter, the effect of Branched Polyethyleneimine (BPEI) as an electrolyte additive on the zinc electrodeposition mechanism was studied. It was determined that the presence of BPEI in the range of 30 ppm inside the electrolyte could suppress the growth of hexagonal crystals and stabilize the electrodeposition efficiency of zinc.

The third part of this dissertation focused the application of layered double hydroxide (LDH) as a substrate for zinc electrodeposition. To do so, GCPL was used and the electrodeposition efficiency of zinc on different substrates serving as the negative electrode was examined. The results showed that the appropriate ratio of zinc to LDH as a substrate considerably enhanced the efficiency of zinc electrodeposition in 500 mM of zinc sulfate, from 88% to 98%. Moreover, LDH suppressed the intense potential drop at the beginning of the reduction reaction that could be attributed to the elimination of hydrogen evolution. LDH, in an appropriate combination with zinc, was determined to be a very good alternative for use as a negative electrode in aqueous zinc-ion batteries.

Finally, water in salt solution was employed to improve the electrochemical stability window of the electrolyte. To accomplish this, a constant current density technique was applied instead of cyclic voltammetry, and 21 m of aqueous LiTFSI solution was used as the electrolyte. It was observed that the electrochemical stability window of the electrolyte depended on the working electrode. In the case of platinum as the working electrode, the electrochemical stability window increased up to 2.68 V; it was 3.33 V when glassy carbon was used as the working electrode. Although the electrochemical stability window of an aqueous electrolyte is less than that of organic electrolytes, applying a highly-concentrated electrolyte seems to be an excellent step forward towards improving the performance of grid-scale energy storage systems.

Kurzfassung

Die Gewährleistung einer verlässlichen Bereitstellung von Energie stellt eine der wichtigsten Aufgaben der heutigen Gesellschaft dar und wird auch zukünftig immer mehr an Bedeutung gewinnen. Um dieses Ziel erreichen zu können, muss die Nutzung erneuerbarer Energiequellen, wie Solar- und Windenergie ausgeweitet werden. Diese Energiequellen können jedoch keine stabile und ununterbrochene Stromversorgung gewährleisten. Daher werden geeignete Energiespeicher benötigt, die große Mengen an Energie in kürzester Zeit speichern können. Metall-Ionen Batterien werden bereits in stationären Systemen angewendet, da diese nicht primär von volumetrischen und gravimetrischen Energiedichten abhängig sind. Für diesen Anwendungsbereich, wurden kürzlich wässrige Zink-Ionen Batterien auf der Basis von Kupferhexacyanoferrat entwickelt, die eine Durchschnittsspannung von 1.73 V aufweisen. Eine niedrige Elektrodepositionseffizienz, sowie die Wasserstoffentwicklung an der negativen Elektrode, stellen die Hauptlimitierungsfaktoren dieser neuen Art von Batterien dar, wenn Zink als negatives Elektrodenmaterial genutzt werden soll, da in diesem Fall das elektrochemische Reduktionspotential so gering ist, dass die Freisetzung von Wasserstoff thermodynamisch begünstigt ist. Die Wasserstoffentwicklung hat einen negativen Einfluss auf die Elektrodepositionseffizienz und somit auf die Leistungsfähigkeit der Batterie, da die Stromdichte und somit die gesamte Energieeffizienz verringert werden. Daher sind der Grad der Wasserstofffreisetzung, sowie die Verbesserung der Elektrodepositionseffizienz für diese Art von Batterien von enormer Wichtigkeit.

Der erste Teil dieser Dissertation befasst sich mit der Entwicklung einer neuen, elektrochemischen Zelle, für die *in-operando* Charakterisierung von Gasentwicklung in Batterien, mit Hilfe von differentieller elektrochemischer Massenspektroskopie (DEMS). Dabei werden verschiedene Parameter, wie die Position, Größe und Form der Elektroden, der Fluss des Trägergases, der Kontakt zwischen Stromanschlüssen und den Elektroden, die Abdichtung der Zelle, sowie der Versuchsaufbau diskutiert. Die Leistungsfähigkeit der Zelle in DEMS Messungen wurde durch die Untersuchung der Gasentwicklung an Graphitelektroden in organischen Lösungsmitteln überprüft. Dabei wurde Zyklische Voltammetrie (CV) mit der DEMS Methode kombiniert. Darüber hinaus, konnte demonstriert werden, dass die Zelle die Durchführung von Elektrochemischer Impedanzspektroskopie (EIS) ermöglicht. Mit Hilfe der Zelle wurde die Wasserstoffentwicklung an negativen Elektroden in wässrigen Zink-Ionen Batterien, die auf Preußischblau-Derivaten basieren, untersucht. Dazu wurde die galvanostatische Zyklisierung mit Potentiallimitierung (GCPL) mit der DEMS-Methode gekoppelt, wobei deutlich wurde, dass der Grad der Wasserstofffreisetzung durch eine Erhöhung der Elektrolytkonzentration reduziert werden konnte.

Im zweiten Teil dieser Abhandlung wurde die Morphologie der Elektrodeposition von Zink an der negativen Elektrode bei unterschiedlichen Stromdichten untersucht. Mehrere konstante

Stromdichten wurden angelegt, wobei die Oberflächenbeschaffenheit mit Hilfe von Rasterelektronenmikroskopie (SEM) und Farb-3D-Lasermikroskopie untersucht wurde. Die Ergebnisse haben gezeigt, dass unterhalb der limitierenden Stromdichte keine bevorzugte Richtung für das Kristallwachstum ermittelt werden konnte, wohingegen oberhalb der limitierenden Stromdichte große, hexagonale Kristalle auf der gesamten Elektrodenoberfläche gebildet wurden. Anschließend wurde der Effekt von Polyethylenimin (PEI) als Additiv in der Elektrolytlösung auf den Mechanismus der Elektrodeposition von Zink untersucht. Dabei wurde ermittelt, dass das Wachstum hexagonaler Kristalle durch eine PEI-Konzentration von etwa 30 ppm in der Elektrolytlösung unterdrückt werden konnte, wodurch die Effizienz der Elektrodeposition von Zink erhöht wurde.

Im dritten Teil dieser Dissertation wurde die Verwendung von ‚Layered Double Hydroxide' (LDH) als Substrat für die Zink-Elektrodeposition diskutiert. Dabei wurde die Elektrodepositionseffizienz von Zink auf unterschiedlichen Substraten mit Hilfe von GCPL getestet. Die Ergebnisse haben gezeigt, dass ein Substrat, mit einer Zusammensetzung aus Zink und LDH in geeignetem Verhältnis, die Elektrodepositionseffizienz in 500 mM Zinksulfatlösung von 88% auf 98% steigern kann. Darüber hinaus, konnte durch den Zusatz von LDH die Wasserstofffreisetzung unterdrückt werden, wodurch der drastische Spannungsabfall zu Beginn der Reduktionsreaktion gemindert wurde. Die Kombination aus LDH und Zink in einem geeigneten Verhältnis dient somit als eine sehr gute Alternative zur Verwendung als negatives Elektrodenmaterial in Zink-Ionen-Batterien.

Zum Schluss wurde eine ‚Wasser in Salz'-Lösung verwendet, um das elektrochemische Stabilitätsfenster des Elektrolyten zu verbessern. Dazu wurde anstelle von Zyklischer Voltammetrie eine Technik mit konstanter Stromdichte verwendet, wobei eine 21 m Lösung von wässrigem LiTFSI als Elektrolyt verwendet wurde. Dabei wurde beobachtet, dass das elektrochemische Stabilitätsfenster des Elektrolyten von der Arbeitselektrode abhängt. Bei der Verwendung von Platin als Arbeitselektrode lag das Stabilitätsfenster bei 2.68 V, wohingegen bei der Verwendung einer Glaskohlenstoffelektrode ein Stabilitätsfenster von 3.33 V beobachtet wurde. Obwohl das elektrochemische Stabilitätsfenster in wässrigen Elektrolyten kleiner ist als in organischen Elektrolyten, kann die Verwendung von hochkonzentrierten Elektrolyten einen bedeutenden Faktor darstellen, um die Leistungsfähigkeit von Energiespeichersystemen zu verbessern.

Acknowledgements

During my work on my PhD, I greatly developed my scientific knowledge, enjoyed strong personal growth, and collected many achievements. None of that would have been possible without the motivation, support, and help of many people. I would like to thank all who contributed in some way to the work described in this thesis.

First and foremost, I would like to thank my first supervisor, Prof. Fabio La Mantia, for giving me the opportunity to work in his group. During this doctoral research, he advocated for me by giving me the intellectual freedom to engage in my work, supported my attendance at various conferences, encouraged my research, engaged me in the pursuit of new ideas, and demanded high quality in all of my endeavors. It has been my honor to be his graduate student. I have learned so much from him from all of our scientific and non-scientific discussions. Additionally, I would like to thank Prof. Mauro Pasta for his interest in this research and his decision to be my second supervisor. I would also like to thank Prof. Dr. Wolfgang Schuhmann for giving me the opportunity to begin this research in his laboratory, and Prof. Dr. Matthias Busse for his support at Fraunhofer, IFAM, in Bremen. Moreover, I would like to thank Prof. Mohammad Mehdi Salari Rad, Prof. Nader Parvin, Prof. Dr. Steffen Strehle, and Prof. Dr. Ulrich Herr for the help they gave me before and during this doctoral process.

Every result explained in this work was obtained with the support of colleagues and collaborators. A very special word of gratitude goes to Ghoncheh Kasiri for her rigorous scientific discussions and kind friendship. Special thanks also goes to Dr. Mu Fan for the discussion leading to the design of the DEMS cell, Dr. Rafael Trócoli for teaching me about batteries, and Dr. Anastasia Dushina for her practical advice in the laboratory. My sincere thanks goes to Dr.-Ing. Julian Schwenzel, and Prof. Dr. Robert Kun, who provided me access to their laboratory and research facilities. Without their valuable support, it would not have been possible to conduct this research. I am also thankful to Marcus Schmerling for introducing me to the SEM and 3D laser microscope at Fraunhofer Oldenburg. I am grateful to Jens Glenneberg for providing me with a number of useful SEM images and EDX analyses at Fraunhofer Bremen. I gained so much from his vast knowledge in the field of electron microscopy. I would also like to acknowledge Frederieke Langer for teaching me how to work with the XRD device and Dr. Jelena Stojadinovic and Dr. Edyta Madej for their support in working with the mass spectrometer.

I would also like to acknowledge my dear friends Dominque Koster and Collins Erinmwingbovo for their priceless friendship. I am also grateful to all of my colleagues: Dr. Giorgia Zampardi, Dr. Guoqing Du, Dr. Doriano Brogioli, Dr. Ingo Bardenhagen, Andjela

Petkovic, Maria Sofia Palagonia, Michael Gockeln, Timo Hemmers, Magdalena Werner, Mari Angeles González, Elena Crespo, Vera Eßmann, and Dr. Sara Borhani Haghighi.

Many thanks to Miriam Gutjahr, Bettina Arena, Bettina Stetzka, and Monika Niggemeyer for their administrative support and all the patience they showed me throughout the years. Thanks to Dr. Thomas Erichsen, Dr. Kirill Sliozberg, Kurt Neumeister, Johannes Schröder, and Sebastian Jenzsch for their technical and IT support. Thanks as well to Armin Lindner, Dieter Brüns, and their team for their effort and close collaboration in fabricating the DEMS cells.

I would also like to express my gratitude to my family: my father Reza Bani Hashemi, my mother Maryam Motamed, my father-in-law Reza Sasani, my mother-in-law Simin Mostafa, my sister Maedeh Bani Hashemi and her husband Mostafa Rezvani, my brother Sajjad Bani Hashemi and his wife Negin Nomani, my sister-in-law Fatemeh Sasani and her husband Mohammad Vaheb, and my brother-in-law Ali Sasani and his wife Motahhareh Rabbani.

Finally, I owe a debt of gratitude to the most precious treasure in my life, Maryam Sasani, who has accompanied me through hard times and supported me in so many critical conditions. Thank you, Maryam, for loving me so much and unconditionally. You are, and have always been, a great inspiration to me. Thank you for your deep love, support, understanding, and encouragement. Without you, I would not have finished this PhD. There are no words to express what you mean to me.

CONTENTS

Abbreviations & Symbols

Abbreviations:

AA CAES	Advanced Adiabatic Compressed Air Energy Storage
AC	Alternative Current
AFM	Atomic Force Microscopy
AMIB	Aqueous Metal-Ion Batteries
APM	Application Mode
BPEI	Branched Polyethyleneimine
CAES	Compressed Air Energy Storage
CE	Counter Electrode
CNT	Carbon Nanotube
CuHCF	Copper Hexacyanoferrate
CV	Cyclic Voltammetry
DC	Direct Current
DEMS	Differential Electrochemical Mass Spectrometry
DLC	Double Layer Capacitor
DMC	Dimethyl Carbonate
EC	Ethylene Carbonate
EDX	Energy-Dispersive X-ray Spectroscopy
EIS	Electrochemical Impedance Spectroscopy
EMC	Ethyl Methyl Carbonate
EQCM	Electrochemical Quartz Crystal Microbalance
ESS	Energy Storage System
FES	Flywheel Energy Storage
GC	Glassy Carbon
GCPL	Galvanostatic Cycling with Potential Limitation
H_2	Molecular Hydrogen or Hydrogen Storage
HFB	Hybrid Flow Batteries
LA	Lead Acid Batteries
LDH	Layered Double Hydroxide
LFP	Lithium Iron Phosphate
LiTFSI	lithium bistrifluoromethanesulfonimidate
LNMO	Lithium Nickel Manganese Oxide
LPEI	Linear Polyethyleneimine
LTO	Lithium Titanium Oxide
Me-air	Metal-Air Batteries
MWCNT	Multi Wall Carbon Nanotube
NaNiCl	Sodium Nickel Chloride (Zebra) Batteries
NaS	Sodium Sulfur Batteries
NBR	Acrylonitrile Butadiene Rubber
NiCd Vented	Nickel Cadmium Batteries
NiMH	Nickel Hybrid Batteries

NMC	Lithium Nickel Manganese Coblat Oxide
NMP	N-Methyl-2-pyrrolidone
PBA	Prussian Blue Analogues
PC	Propylene Carbonate
PCR	Primary Control Reserve
PEEK	Polyether Ether Keton
PEI	Polyethyleneimine
PHS	Pumped Hydroelectric Storage
PPS	Polyphenylene Sulfide
PPy	Polypyrrole
PS	Propane Sultone
PSB	Polysulfide Bromide Batteries
PTFE	Polytetrafluoroethylene
PV	Photovoltaic
PVDF	Polyvinylidene Fluoride
RE	Reference Electrode
RES	Renewable Energy Source
RFB	Redox Flow Batteries
SCCM	Standard Cubic Centimeters per Minute
SCR	Secondary Control Reserve
SECM	Scanning Electrochemical Microscopy
SEI	Solid Electrolyte Interphase
SEM	Scanning Electron Microscopy
SHE	Standard Hydrogen Electrode
SMES	Superconducting Magnetic Energy Storage
SNG	Synthetic Natural Gas
TCR	Tertiary Control Reserve
TES	Thermal Energy Storage
TMB	Trimethylboroxine
UPS	Uninterrupted Power Supply
VC	Vinylene Carbonate
VEC	Vinyl Ethylene Carbonate
VRB	Vanadium Redox Batteries
WE	Working Electrode
XPS	X-Ray Photoelectron Spectroscopy
XRD	X-Ray Diffraction
ZnBr	Zinc Bromine Batteries
ZnHCF	Zinc Hexacyanoferrate

Symbols:

$[Ox]$	Concentration of Oxidant
$[Red]$	Concentration of Reductant
$\|Z\|$	Impedance magnitude
Δt_H	The Time Difference Between the Starting Point of the CuHCF Oxidation and Hydrogen Evolution
A	Frequency Factor
a, q	Dimensionless Parameters to Find the Stability Region of Quadrupole Filter
$C65$	Carbon Black
C_B	Bulk Concentration
C_i	Concentration of Species *i*
D	Diffusion Coefficient
δ	Thickness of the Nernst Layer
E	Energy of the Reaction
E^0	Standard Energy of the Reaction at equilibrium Condition
E_A^0	Activation Energy at Equilibrium Condition
E_A	Activation Energy
E_a	Oxidation Potential
E_c	Reduction Potential
F	Faraday Constant
i_L	limiting Current
K_i	Reaction Rate Constant for Species *i*
n	number of Electrons Transferred During the Electrochemical Reaction
nC *rate*	a Rate of nC Represents a Full Charge or Discharge in 1/n Hours
Q	Charge
R	Universal Gas Constant
r_0	Field Radius
r_i	Reaction Rate for Species *i*
T	Temperature
U_{quad}	Electrical Voltage of Quadrupole Mass Spectrometer
α	Transfer Coefficient
φ	Phase Shift Between the AC Current and the AC Potential in the EIS Measurements
ω	Angular Frequency

List of Figures

List of Tables

1. Introduction

1.1. Energy Storage

The most significant challenges in the current century involve compensating for the global energy demand, decelerating population growth, and controlling global warming. Among these, it is believed that providing a sufficient amount of energy is the primary problem facing future societies [1]. Solving this issue may be the key to eliminating the other two. The second challenge is the population increase now seen all over the world. The world experienced a 4.5-fold growth between 1990 and 2014; the global population reached 7.2 billion that same year. By 2100, the world's population will be more than 11 billion, and this will require a similar growth in energy production. Right now, the primary source of the world's energy supply is fossil fuels, the combustion of which has led to global warming. Global warming is a critical issue, and increases in temperature should be limited to < 2°C to prohibit an environmental disaster [2,3]. To achieve this goal, it is of primary importance that fossil fuel use is restricted, since it is one of the main causes of global warming and pollution [4]. Moreover, it is essential to expand the use of renewable energy sources (RES) as soon as possible. If fossil fuels are used without limitation, a global temperature of 42°C will be unavoidable in the near future [5].

Currently, about 30% of the electricity required around the world is provided by RES [6]. To maintain a global warming rate of less than 2°C, more than 45% of this energy should be provided via RES by 2035 [6,7]. By 2100, this contribution should be more than 85% [7]. Figure 1-1 illustrates the different RES levels needed for energy provision in the future. Wind and solar photovoltaic (PV) are two RES that should be capable of providing more than 40% of the energy needed in the next twenty years. These types of energy sources are inherently intermittent (i.e., volatile, remote, and distributed all over the world). In addition, the following two features have led to significant interest in the development of improved energy storage systems (ESSs) [8]:

1- The amount of electricity generation should at any time be adjustable to meet the level of electricity consumption. Any inequality between the two may harm sensitive devices.
2- Due to the various distances between suppliers and consumers, transmission congestion may occur. This can undermine grid stability and lead to high-priced outages.

Therefore, a profitable ESS and powerful network are key to stabilizing energy distribution across the electric grid.

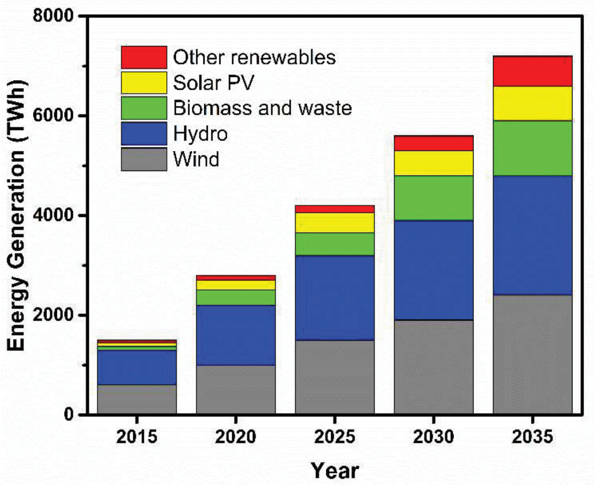

Figure 1-1: Global electricity production based on renewable sources [9].

To develop a quality ESS, certain parameters must be considered:

1- Economics: the economy is the main limitation on how fast an ESS can be implemented in the electric grid. Customers prefer reliable, low-cost energy sources. Therefore, capital, operating, and lifetime costs are decisive [6].

2- Design: this includes storage media, the area needed to build up the system, grid-level control, and power for the electronic conversion. The environmental friendliness of the system and safety issues should also be considered [6].

3- Performance: the system should technologically provide all features necessary for the proposed applications. There are certain parameters that should be taken into account in any potential choice of grid-scale energy storage, as follows:

    a. Power rating: the maximum power output of a system when working under normal circumstances [10].

    b. Discharge duration: the time necessary to completely discharge with the power rating during one cycle [10].

    c. Lifetime discharge: the number of discharge cycles which the ESS can deliver more than 80% of the energy discharged during its first cycle. This factor is especially important for batteries that degrade during cycling.

    d. Charge and discharge rates (response time): these two parameters define the minimum time an ESS needs for a complete charge and discharge. Response time is especially important in the electric grid. Due to large fluctuations between peak and off-peak periods, an ESS should be capable of quick responses to balance the grid [10].

e. Power and energy density: power density is a normalized power rating per unit of mass or volume. Similarly, energy density is the total energy that can be stored per volume or mass unit [10]. Figure 1-2 compares different ESS technologies based on their power and energy densities. These factors are very important when designing a grid in conditions where the area or weight is limited.

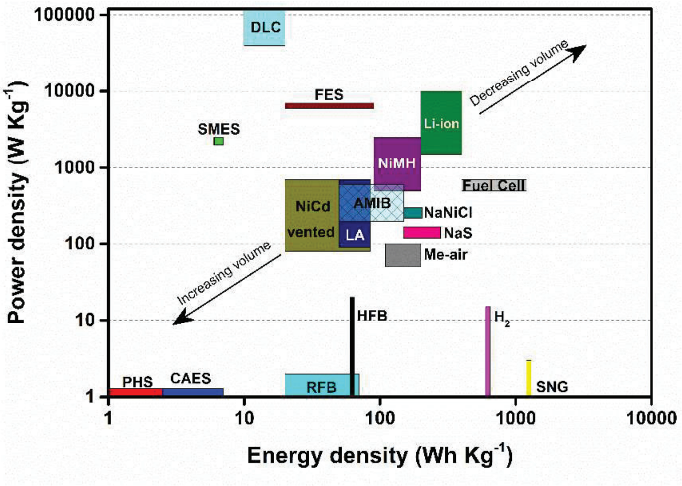

Figure 1-2: Comparison of different ESS technologies based on their power and energy densities. PHS: Pumped Hydroelectric Storage; CAES: Compressed Air Energy Storage; RFB: Redox Flow Batteries; HFB: Hybrid Flow Batteries; H_2: Hydrogen Storage; SNG: Synthetic Natural Gas; NiCd Vented: Nickel Cadmium Batteries; LA: Lead-Acid Batteries; AMIB: Aqueous Metal-Ion Batteries (under investigation); NaS: Sodium Sulfur Batteries; Me-air: Metal Air Batteries; NaNiCl: Sodium Nickel Chloride (Zebra) Batteries; NiMH: Nickel Metal Hydride Batteries; Li-ion: Lithium-Ion Batteries; FES: Flywheel Energy Storage; SMES: Superconducting Magnetic Energy Storage; and DLC: Double Layer Capacitor [11,12].

f. Cycle efficiency: this is the ratio of the output to input energy of an ESS. In batteries, this parameter is called energy efficiency; it shows energy loss after an appropriate number of cycles [12]. Figure 1-3 shows the cycle efficiencies for different ESS technologies.

g. Standby losses and energy retention: the amount of energy lost during the standby time of an ESS is called its standby loss. Electrochemical energy storage systems lose their energy during standby mode via self-discharge. For pumped hydroelectric storage systems, the main reason for standby losses is water evaporation. This factor is very important when an ESS is used as supporting device in an electric grid.

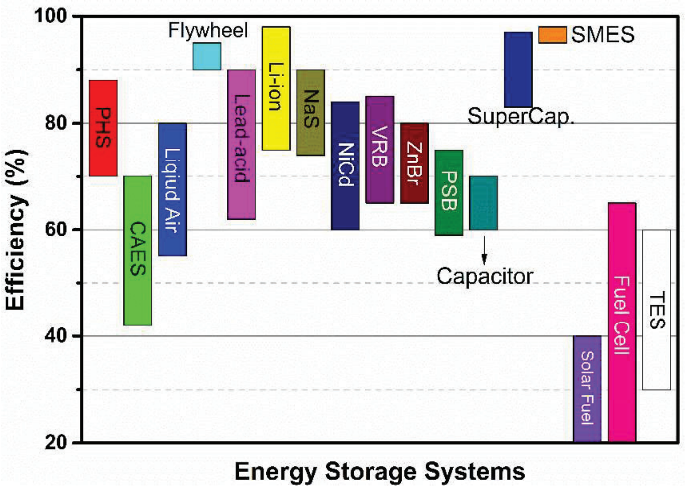

Figure 1-3: Comparison of cycle efficiency rates for different ESS technologies.

4- Application modes (APM): one of the most important characteristics of an ESS is its ability to work in a special, single task. Such tasks are called APMs and they can be classified as follows [13]:

   a. Uninterrupted power supply (UPS): an ESS should be able to provide power during a long blackout. It should also be capable of balancing the grid frequency at any time.

   b. Black start capability.

   c. Primary, secondary, and tertiary control reserve: control reserve is applied in electric grids to ensure a balance between electricity demand and generation.

   d. Peak-shaving, shifting, and managing.

   e. Grid support.

   f. Residential storage: residential storage gives a household the ability to save excess energy collected during the day from photovoltaic panels, and use it when there is no access to renewable energy sources.

   g. Island grids: there are more than two thousand islands around the world with up to 100,000 inhabitants living on each. Researchers have shown that a combination of photovoltaic panels and ESSs provide an ideal solution to supplying energy to these islands.

Based on the above-mentioned APMs, Table 1-1 shows the ability of different ESSs to be served in specific APMs. In this Table, more stars indicate higher levels of ability.

Table 1-1: Ability of Different ESS to Work in Various APMs [13]

Energy storage system	Electrical		Chemical	Electrochemical				Mechanical			
	DLC	SMES	H_2	Lead Acid	NaS	Redox Flow	Li-Ion	PHS	FES	CAES	AA-CAES
UPS	***	***	**	**	**	**	***	*	**	*	*
Black Start	*	*	*	**	**	**	**	***	*	***	***
PCR/SCR/TCR	*	*	*	***	***	**	***	***	*	***	***
Residential	*	*	*	***	*	**	***	*	*	*	*
Islands	*	*	*	***	***	***	***	*	*	**	**
Peak-Shaving, Shifting, Managing	*	*	*	**	***	**	***	***	*	**	***
Grid Support	*	*	*	**	***	**	***	*	**	***	***

It can be concluded from Figures 1-2 and 1-3 and Table 1-1 that the development of an ESS for grid-scale energy storage can be based on lithium-ion batteries. In the next section, this type of energy storage system will be explained in detail. Before that, a general overview on batteries will be presented.

1.2. Lithium-Ion Batteries

The last two decades have seen a very rapid growth in the field of electrochemical energy storage and conversion, especially with regards to rechargeable batteries as ESSs. Currently, more than 50% of ESS projects have focused on electrochemical energy storage devices. Among these, more than 60% were based on lithium-ion batteries [13]. Moreover, lithium-ion batteries occupy about 37% of global battery marketing. Thus, this technology has the potential to be used widely in grid-scale energy storage. Figure 1-4 shows the distribution of different types of batteries around the world.

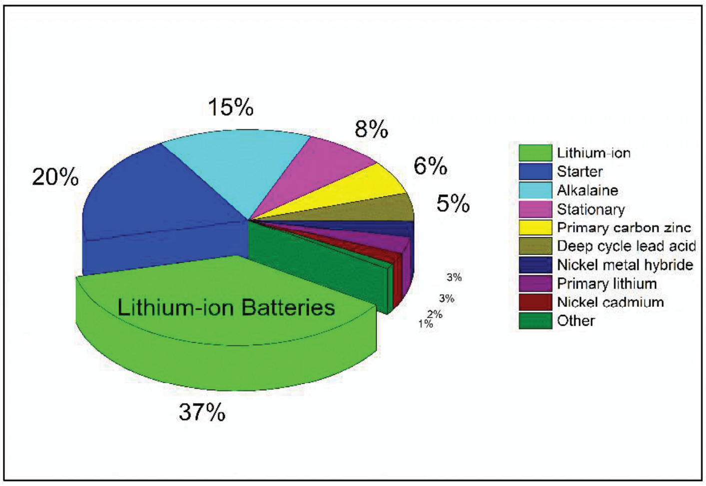

Figure 1-4: Global contribution of different types of batteries.

Before focusing on lithium-ion batteries, a brief review of batteries in general is given below [4]. A battery is a device from which the energy is generally produced based on following reaction:

$$A + B \leftrightarrow C + D \tag{1-1}$$

where A is an oxidant, and B is a reductant. In this reaction, electrons flow from B to A, resulting in the formation of C and D. In a battery based on electrochemical reactions, two distinct reactions are distinguishable: anodic and cathodic. These reactions occur on two sides of the battery that are separated from one another by separators. A separator is ionically conductive, but has no electrical conductivity. Therefore, the electrochemical reaction can be written as follows:

$$Anodic\ reaction{:}\ \ B \rightarrow C + ne^- \tag{1-2}$$

$$Cathodic\ reaction{:}\ \ A + ne^- \rightarrow D \tag{1-3}$$

In general, batteries can be categorized from different points of view and according to various classification types, such as:

1- Primary versus secondary. Primary batteries can only be used a single time, while secondary batteries can be recharged several times.

2- Static versus flow systems. In a flow system, the electrolyte flows and redox couples perform the charge transfer during the flow of the electrolyte. Vanadium redox flow and zinc-bromine flow batteries are examples of this.

3- Aqueous versus non-aqueous batteries. There are a number of important aqueous batteries; among them, lead-acid, nickel-cadmium, and nickel metal hydride are the most popular. Organic rechargeable batteries are the most common non-aqueous batteries.

Based on the aforementioned classifications, lithium-ion batteries are secondary, static systems. They can be aqueous or non-aqueous, based on the electrolyte. Currently, most lithium-ion batteries are non-aqueous. Lithium-ion batteries store electrical energy in the form of chemical energy. They are comprised of three main components: a cathode, anode, and electrolyte. Electrolytes contain a solvent that can be organic, ionic liquid, or aqueous, and at least one salt. The cathode and anode materials may be porous; their thicknesses will vary between 30 µm and 150 µm, depending on their application. To obtain porous electrodes, an active material, the main substance inside the electrode that reacts with the lithium ions, is mixed with binders and other conductive materials such as carbon black C65.

Typically, the reaction between the lithium ions and electrodes can be divided into three main classifications, as follows:

1- Intercalation reactions

In this reaction, lithium ions are introduced inside the structure of the electrode. Most of the reactions on the cathode material are intercalation reactions. Graphite and lithium titanium oxides are examples of anode materials by which lithium ions are intercalated. Usually, no crystal change is introduced to the crystalline structure during intercalation reactions [4,14].

2- Conversion reactions

This type of reaction can be defined as follows:

$$MX + 2e^{-} + 2Li^{+} \leftrightarrow M^{0} + Li_{2}X \tag{1-4}$$

where M is a transition metal (e.g., Fe, Cu, Co, etc.) and X can be P, F, O, or even H. To result in a reversible reaction, MX must be nano-sized. Due to the substantial hysteresis in their potential curve, their applications are restricted [15].

3- Alloying reactions

Alloying commonly occurs between the lithium and elements such as silicon (Si), tin (Sn), and Germanium (Ge). This reaction can be described as follows:

$$xLi^{+} + xe^{-} + M \leftrightarrow Li_{x}M \quad (1\text{-}5)$$

The problem with these reactions is that they result in a substantial volume expansion, usually of more than 200%. Therefore, the mechanical stability of the electrodes during cycling is very poor. Moreover, due to the lack of a passivation layer, side reactions can be expected.

To discharge the battery, lithium ions are transported from the anode to the cathode through the electrolytes, and react with the cathodic materials. During charging, the reverse reaction occurs. Figure 1-5 presents a schematic of a lithium-ion battery during the discharge process.

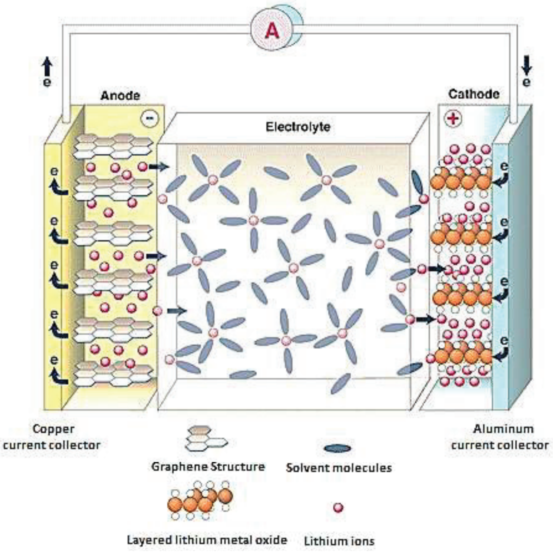

Figure 1-5: Schematic of a lithium-ion battery during the discharge process (modified from [16]).

1.2.1. Cathode

Cathode material in lithium-ion batteries can be categorized into three general groups: layered lithium metal oxides, spinels, and olivines [17,18]. The most famous lithium metal oxides are lithium nickel oxide and lithium cobalt oxide, both of which are toxic. Synthesis of these materials is very difficult and expensive. They also suffer from low rate capability. Kang et al. [19] argued that the key to improving the rate capability of layered metal oxides is to combine them with low-valent transition metal ions and lower the strain in the activated state. That research led to the synthesis of lithium nickel manganese cobalt oxide, which showed a high operating voltage [20]. A simple sketch of layered lithium metal oxide can be found in Figure 1-6.

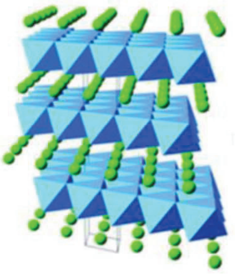

Figure 1-6: The structure of layered lithium metal oxide. The green points are lithium ions and the blue structures are layered metal oxide (modified from [21]).

Another structure commonly used as a positive electrode in lithium-ion batteries is the spinel. Lithium manganese oxide is the oldest compound from this family. This material shows a high rate capability and thermal stability, and uses environmentally friendly components [22]. The cost of fabrication is also lower than layered lithium metal oxides. Therefore, it has been widely applied as a cathode material. A spinel structure is illustrated in Figure 1-7.

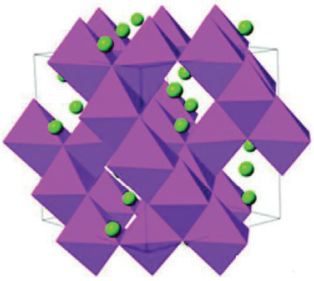

Figure 1-7: Spinel structure. The green points are lithium ions and the pink constructions are spinels (modified from [21]).

Lithium iron phosphate is a well-known compound with an olivine structure. It is non-toxic and shows a flat discharge plateau. The most important advantage to this material over lithium cobalt oxide is related to safety issues. Thus, in terms of security, it is a better choice for grid-scale energy storage. Moreover, iron is very cheap. So, the final price of this material is lower than others. One significant disadvantage of lithium iron phosphate, however, is its low conductivity, which leads to the low charge potential [23,24]. Figure 1-8 shows a schematic of an olivine structure.

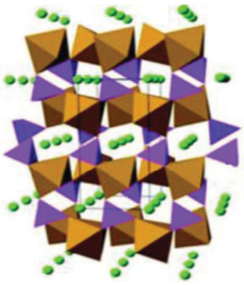

Figure 1-8: Olivine structure of lithium iron phosphate. The green points are lithium ions, brownish constructions are Fe-O bonds, and bluish items are PO_4 molecules (modified from [21]).

There are also other cathodic materials that can be used in lithium-ion batteries. Table 1-2 presents the structure, average voltage, and specific capacity of each.

Table 1-2: Structure, Average Voltage, and Specific Capacity of Cathodic Materials in Lithium-Ion Batteries (extracted from [21])

Crystal	Compound	Average Voltage (V)	Specific Capacity (mAh g^{-1}) Theoretical/Experimental
Layered	**$LiTiS_2$**	1.9	225/210
	$LiCoO_2$	3.8	274/148
	$LiNiO_2$	3.8	275/150
	$LiMnO_2$	3.3	285/140
	$LiNi_{0.33}Mn_{0.33}Co_{0.33}O_2$	3.7	280/160
	$LiNi_{0.8}Co_{0.15}Al_{0.05}O_2$	3.7	279/199
	Li_2MnO_3	3.8	458/180
Spinel	**$LiMn_2O_4$**	4.1	148/120
	$LiCo_2O_4$	4.0	142/84
Olivine	**$LiFePO_4$**	3.4	170/165
	$LiMnPO_4$	3.8	171/168
	$LiCoPO_4$	4.2	167/125

1.2.2. Anode

The most important anode material in lithium-ion batteries is graphite. Graphite has a 2D layered structure that served as the source of the electrochemical activity. This 2D structure guarantees electrical conductivity, mechanical stability, and lithium ion intercalation. Each carbon ring of graphite can serve as a host for one lithium atom [4,21]. The intercalation process can be described as follows:

$$Li^{+} + C_6 + e^{-} \rightarrow LiC_6 \tag{1-6}$$

For the last 25 years, carbon's low cost, abundance in nature, low discharge potential, high conductivity and lithium diffusivity, and low volume change during charge/discharge have made it the best choice for use as a negative electrode in lithium-ion batteries [21].

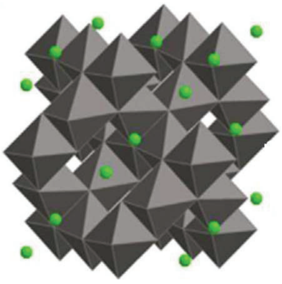

Figure 1-9: LTO structure. The green points are lithium ions and gray items are LiO_6 or TiO_6 (modified from [20]).

Another material that has been commercialized as a negative electrode for lithium-ion batteries is lithium titanium oxide (LTO). This compound has several advantages such as a high cycle life, excellent thermal stability, and a zero-strain intercalation mechanism that makes it a good alternative as a negative electrode in lithium-ion rechargeable batteries [25–28]. Zero strain means that the intercalation/deintercalation of the lithium ion inside the structure leads to a negligible volume change. The equilibrium potential of LTO is equal to -1.55 V vs. Li/Li^{+}. This potential avoids, or at least decreases, the solid electrolyte interphase (SEI) formation and increases the kinetics of the lithium intercalation/deintercalation [26]. Additionally, the equilibrium potential of LTO prevents any dendrite formation in the lithium, which makes this material very safe [28]. Figure 1-9 presents the schematic structure of LTO.

Other materials that could be used as anodes in lithium-ion batteries are listed in Table 1-3.

Table 1-3: Structure, Intercalation and Deintercalation Potentials, and Volume Change of Anodic Materials in Lithium-Ion Batteries (extracted from [21])

Material	Intercalation Potential vs. Li/Li^{+} (V)	Deintercalation Potential vs. Li/Li^{+} (V)	Volume Change
Graphite	0.07, 0.10, 0.19	0.1, 0.14, 0.23	10%
LTO	1.55	1.58	0.2%
Si	0.05, 0.21	0.31, 0.47	270%
Ge	0.2, 0.3, 0.5	0.5, 0.62	240%
Sn	0.4, 0.57, 0.69	0.58, 0.7, 0.78	255%

1.2.3. Electrolytes

Electrolytes are component of the batteries that contain an ion-conducting phase in the form of a liquid, gel, or solid solution [29]. This phase can be an additive [30], matrix for a structural enhancement [31,32], and so on. Electrolytes are considered the most important component in rechargeable batteries because they are the only component that contributes to all interfaces in which the rate capability of the battery is controlled [30]. Liquid electrolytes are the most common electrolyte used in battery technology, due to their superior ability to make contact with electrodes all over the interface. Moreover, their ionic conductivity is higher than other types of electrolytes. Nevertheless, safety concerns [33] such as leakage, flammability, and stability are a major challenge when applying this type of electrolytes in grid-scale energy storage. Liquid electrolytes can be categorized into three different groups, discussed in detail below.

- Organic liquid electrolytes [34]

The most common electrolytes in lithium-ion batteries are based on organic solvents. Classic organic solvents like ethylene carbonate (EC), dimethyl carbonate (DMC), propylene carbonate (PC), and ethyl methyl carbonate (EMC) are usually used in organic electrolytes. The most important factors for solvents are their viscosity, boiling and/or melting point, and dielectric constant. In addition, safety issues such as flammability, toxicity, and thermal stability must also be considered. Typical salts for organic electrolytes include lithium perchlorate ($LiClO_4$), lithium hexafluorophosphate ($LiPF_6$), and Lithium bis(trifluoromethanesulfonyl)imide (LiTFSI). The final cost of preparation and environmental impact, as well as the solubility into the solvent and thermal and electrochemical stability are crucial aspects for the salts. Furthermore, the ability of the electrolyte to form a reliable and permanent SEI in the first cycle and be compatible with the electrodes are also very important.

- Ionic liquid electrolytes

Ionic liquids are molten salts at room temperature; they can be used as a solvent for electrolytes in lithium-ion batteries or as an electrolyte in capacitors [35,36]. They have several remarkable characteristics that make them a viable alternative to organic liquid electrolytes. First, the high electrochemical stability of the ionic liquid electrolytes, up to 6 V, is preferable in battery applications. Second, they show a thermal stability, above 300°C. They are also of a low volatility and non-flammable [29]. Despite these characteristics, their application in the batteries is limited by the high cost of production. Moreover, they suffer from a low rate capability and poor cycle performance, which are the main restrictions to employing them as high-performance electrolytes. Figure 1-10 shows common ionic liquids that can be utilized as ionic liquid electrolytes.

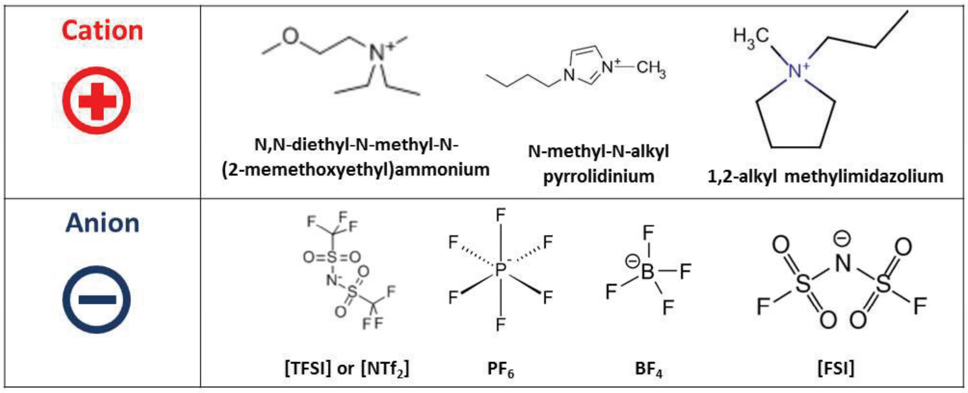

Figure 1-10: Common ionic liquids that can be utilized as ionic liquid electrolytes [29].

- Aqueous liquid electrolytes

Applications for aqueous liquid electrolytes date back to the previous generation of batteries, such as those comprised of nickel-cadmium and nickel metal hydride. Recently, due to issues of safety and environmental friendliness, aqueous liquid electrolytes have been studied for applying in grid-scale energy storage [37–42]. In general, this type of electrolyte is much safer than organic and ionic liquid electrolytes. Moreover, the ionic conductivity of aqueous electrolytes is approximately two orders greater than organic electrolytes. Additionally, they are low in cost, due to their water-based solution of lithium salts such as lithium sulfate (Li_2SO_4) or lithium nitrate ($LiNO_3$). Furthermore, they are classified as "green" electrolytes because they are highly environmentally friendly [29]. Conversely, organic electrolytes are flammable, toxic, and sensitive to moisture and oxygen. Overheating this type of electrolyte may lead to evaporation and battery explosion [43,44]. Based on this analysis, aqueous liquid electrolytes are one of the best alternatives for grid-scale energy storage. In the next section, aqueous metal-ion batteries are discussed.

1.3. Aqueous Metal-Ion Batteries

As mentioned above, aqueous liquid electrolytes are a potential choice for grid-scale energy storage due to their low cost, high ionic conductivity, safety, non-flammability, and being environmental friendliness. However, they have a low electrochemical stability window, due to the decomposition of water, which thermodynamically splits at 1.23 V [45]. The electrochemical stability window of an aqueous electrolyte can be enhanced by pH adjustment [46], oxygen elimination [47], and highly concentrated electrolytes [48]. Additionally, electrochemical reactions in water-based electrolytes are very complicated. Besides intercalation reactions, a number of side reactions can occur, such as co-intercalation of protons into the electrodes, electrode reactions with the water or oxygen, dissolution of the electrode's active materials inside the water-based solution, oxygen and hydrogen evolution, and intercalation of different ions as impurities from the water-based solution into the electrode [49,50]. In the following section, aqueous lithium-ion batteries are introduced. Then, possible aqueous metal-ion batteries are presented as a potential replacement for conventional lithium-ion batteries in large-scale applications.

1.3.1. Aqueous Lithium-Ion Batteries

Lithium-ion batteries using organic electrolytes are energy storage systems with high levels of energy density. However, they suffer from safety, toxicity, and cost issues. They also do not provide superfast charging of the electrodes, due to the low ionic conductivity of the electrolyte, which is a vital parameter when storing energy from inherently intermittent renewable energy sources. Aqueous lithium-ion batteries are ideal for this purpose because of their high ionic conductivity, excellent reliability, and safety [51]. Yet, in addition to the narrow electrochemical stability window of the electrolyte, the rate capability and cycling stability of this type of battery must be strengthened before it will fulfill all the requirements for large-scale energy storage. The poor rate capability of aqueous lithium-ion batteries can be improved by using nanostructured materials in positive and negative electrodes. Due to the high specific surface area of nanostructured materials, they can provide more channels for intercalation/deintercalation. Moreover, the distance of solid-state diffusion is much shorter, which improves the rate capability of the material [52].

Capacity fade is a second important limitation of aqueous lithium-ion batteries that affects their cycling stability. The origin of capacity fading is structural distortions during the intercalation/deintercalation of the lithium ions. Application of nanoporous structures in electrode materials is a practical way of decreasing the level of structural distortion in the structure of the electrodes during charge and discharge [52]. The advantages of nanoporous structures can be summarized as follows [52,53]:

- High crystallinity that guarantees structural stability.
- Shorter diffusion distance for lithium ions.
- Enhancement of the contact between the electrode and the electrolyte.
- Reduction of polarization.
- Facilitation of lithium intercalation/deintercalation.
- Adaption to any stress/strain during charge/discharge process from the Jahn-Teller effect.

Table 1-4: Cycling Performances of Different Materials as Cathodes and Anodes in Aqueous Lithium-Ion Batteries (modified from [51])

Material		Cycling Performance (capacity retention)
$LiCoO_2$ nanoparticles	Cathode	No capacity fading after 40 cycles
$LiMn_2O_4$ nanochains		No capacity fading after 200 cycles
Porous $LiMn_2O_4$		93% after 10,000 cycles
Al-doped $LiMn_2O_4$		95% after 100 cycles
$H_2V_3O_8$ nanowires	Anode	72% after 50 cycles
$Li_xV_2O_5$		80% after 40 cycles
$LiTi_2(PO_4)_3$		82% after 200 cycles
MoO_3 coated with PPy		90% after 50 cycles
Hybrid of V_2O_5 nanowires and MWCNTs coated with PPy		No capacity fading after 500 cycles

1.3.2. Aqueous Sodium-Ion Batteries

Due to a lack of source of lithium, developing lithium-ion batteries for grid-scale energy storage is not desirable. One alternative are aqueous sodium-ion batteries; there is an abundance of sources of sodium around the world [54]. The main problem with this type of battery is related to the ionic radius of sodium, which is much larger than lithium; it is challenging to find suitable positive and negative electrodes for intercalation and deintercalation of sodium ions [40]. These compounds should have crystal constructions with large tunnels, open framework structures, 2D layered assemblies, or 3D structures with corner-sharing matrices [55]. In recent years, several attempts have been made to introduce different crystal structures as potential positive and negative electrodes for aqueous sodium-ion batteries.

Manganese-cobalt hexacyanoferrate [56] and manganese hexacyanomanganate [57] have recently been employed as positive electrodes. These compounds are members of Prussian blue analogues (PBA) materials [38,58]. PBA's general formula is $A_xPR(CN)_6$. In this formula, P and R represent transition metals such as Cu, Fe, Co, Ni, Mn, or Zn, or a mixture of these. They bond with each other by CN ligands that comprise an open framework, face-centered cubic structure. In this formula, A represents the large interstitial sites inside the structure that make the intercalation of guest ions possible. The structure of PBA is presented schematically in Figure 1-11. Other possible compounds that might serve as positive electrodes in aqueous sodium-ion batteries include $Na_2FeP_2O_7$, Na_xMnO_2, and birnessite-type MnO_2 [40].

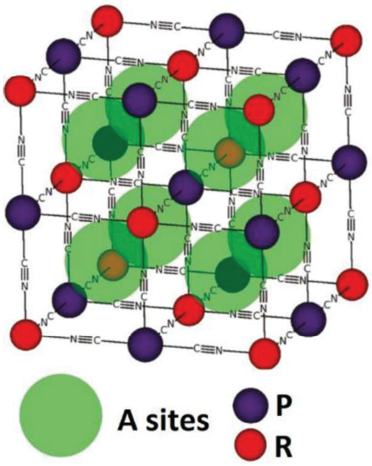

Figure 1-11: PBA structure (modified from [59]).

There are only a few studies that have introduce reliable compounds for negative electrodes in aqueous sodium-ion batteries. These studies have generally addressed the open framework structure, with two types of interstitial sites allowing for rapid transport of sodium ions through the lattice. Nasicon-type phase $NaTi_2(PO_4)_3$ is one of these compounds [60,61]. Recently, phosphorous has also been determined to be an attractive compound for negative electrodes in aqueous sodium-ion batteries, due to its high theoretical capacity of 2596 mAh g^{-1} [62,63]. However, the large volume expansion of this structure during the reaction with sodium has led to the restricted application of this material in batteries.

It should be noted that lithium and sodium-ion batteries can deliver just one electron per ion, which restricts the charge capacity. Therefore, multivalent aqueous metal-ion batteries have recently been considered, because they deliver more than one electron and provide a higher capacity [64]. In the next section, an overview of aqueous multivalent metal-ion batteries is presented. Finally, aqueous zinc-ion batteries are introduced as an alternative for lithium-ion batteries in stationary applications.

1.3.3. Aqueous Zinc-Ion Batteries

To store energy from renewable sources, it is better to use a battery with a high charge capacity. One method of storing more charge capacity is to use multivalent cations (e.g., Al^{3+}, Ni^{2+}, Mg^{2+}, Zn^{2+}, Ca^{2+}) as intercalation species. Table 1-5 shows a comparison of the standard electrode potential and theoretical capacity of the reduction of monovalent and multivalent cations.

Table 1-5: Comparison of Standard Electrode Potential and Theoretical Capacity of the Reduction Reactions of Monovalent and Multivalent Cations (modified from [64])

Electrochemical Reaction	Standard Electrode Potential vs. SHE (V)	Theoretical Capacity	
		Specific Capacity ($mAh\ g^{-1}$)	**Volumetric Capacity ($mAh\ cm^{-3}$)**
$Li^+ + e^- \rightarrow Li$	-3.05	3,829	2,044
$Na^+ + e^- \rightarrow Na$	-2.71	1,165	1,128
$Al^{3+} + 3e^- \rightarrow Al$	-1.66	2,980	8,046
$Mg^{2+} + 2e^- \rightarrow Mg$	-2.36	2,234	3,882
$Ca^{2+} + 2e^- \rightarrow Ca$	-2.87	1,337	2,073
$Ni^{2+} + 2e^- \rightarrow Ni$	-0.257	913	8,133
$Zn^{2+} + 2e^- \rightarrow Zn$	-0.76	820	5,854

It is important to note that multivalent metals can provide high storage capacities. They are low in cost, abundant in nature, and easy to employ. Therefore, they could be used as anodes in aqueous metal-ion batteries [64].

Among the various multivalent aqueous metal-ion batteries, zinc-ion batteries are a useful alternative for large-scale energy storage. In this type of battery, zinc is employed as a negative electrode. Cheap and simple chemistry solutions such as $ZnSO_4$, $Zn(ClO_4)_2$, and $Zn(NO_3)_2$ can be used as the electrolyte. Currently, most of the research has focused on the development of cathode materials for this type of battery [65–67]. For instance, different types of MnO_2 were considered as possible positive electrodes in zinc-ion batteries [68–70]. Table 1-6 lists the advantages and disadvantages of using different types of MnO_2 for the cathode in aqueous zinc-ion batteries.

Table 1-6: Advantages and Disadvantages of Using MnO_2 as a Cathode in Aqueous Zinc-Ion Batteries (extracted from [64])

Material	Advantages	Disadvantages
α-MnO_2	Discharge potential of 1.3 V and energy density of 225 Wh kg^{-1} at moderate currents	Capacity fading in long-term cycling Poor performance at high currents
λ-MnO_2	Initial discharge capacity of 442.6 mAh g^{-1} Coulombic efficiency of nearly 100% for number of cycles	Large capacity fading at high currents
Todorokite	Easy Zn^{2+} diffusion due to larger interlayer spacing than α-MnO_2 Partial shielding effect of Zn^{2+} due to the presence of water inside the structure Less electrostatic reaction and bonding effect of Zn^{2+} due to the presence of water inside the structure Better capacity retention than α-MnO_2 at high currents	Less discharge capacity than α-MnO_2 due to the presence of Mg^{2+} inside the structure

Another structure that has been investigated as a cathode for aqueous zinc-ion batteries is PBA [58,65,67,71]. In PBA, the capacity is limited by the balance between the number of intercalated ions and the number of available P position inside the structure [59]. For instance, in zinc-ion batteries based on copper hexacyanoferrate (CuHCF), the capacity is limited by the equilibrium between the number of intercalated zinc ions and the number of accessible Fe^{2+} in the structure. Thus, the ionic valence of intercalated cations is not of primary importance.

The PBA structure shows superior intercalation and deintercalation of the multivalent cations, based on the shielding effect of water molecules inside the structure and ferricyanide vacancies. The shielding effect can decrease the electrostatic interactions between the host ions in the PBA structure and the guest intercalated ions. The ferricyanide vacancies promote the migration of guest ions inside the structure by providing a shorter diffusion distance and stabilizing the PBA structure after ion intercalation by the redistribution of charges. These two effects make the PBA structure an appropriate positive material for aqueous zinc-ion batteries [58].

Rhombohedral zinc hexacyanoferrate (ZnHCF) is one of the structures derived from PBA that is utilized as a positive electrode in aqueous zinc-ion batteries [67]. This material shows a specific capacity of 65.4 mAh g^{-1} at 1C (a rate of nC represents a full charge or discharge in 1/n hours) using zinc foil as a negative electrode and 1 M $ZnSO_4$ as an electrolyte, with an average discharge potential of 1.7 V. A capacity retention of 76% after 100 cycles has been recorded for this material.

The other derivative from PBA is copper hexacyanoferrate (CuHCF), which has shown successful intercalation of Zn^{2+} using zinc foil as a negative electrode and 20 mM $ZnSO_4$ as an electrolyte, with a specific capacity of 60 mAh g^{-1} [65]. This material shows an average discharge potential of 1.73 V and 96.3% of the capacity retention after 100 cycles. The rate capability of this battery is good and it can provide more than 80% of its theoretical capacity at 10C.

In another study [72], the application of hyper-dendritic zinc as negative electrode led to a capacity retention of more than 90% after 100 cycles and 83% after 500 cycles. This great improvement in the capacity retention shows the effective role of zinc as a negative electrode in the capacity fading of zinc-ion batteries, based on Prussian blue analogues. Zinc is often utilized as a negative electrode in aqueous zinc-ion batteries. However, its equilibrium electrochemical potential is beyond the electrochemical stability window of current electrolytes such that, at least thermodynamically, hydrogen evolution is favored. Hydrogen evolution negatively influences the performance of a battery, hindering the power density and lowering the total specific energy. Moreover, it can inversely influence the electrodeposition efficiency of zinc during cycling. To further develop of this type of battery, a better understanding of the main and side electrochemical reactions is required. This knowledge can be achieved by using different types of electrochemical, structural, and morphological characterization techniques, a topic that is briefly presented in the next section.

1.4. Characterization Techniques

There are several different techniques that can be used to study the performance of electrodes and electrolytes during the intercalation/deintercalation of batteries. These techniques provide information about surface variations of electrodes and/or electrolyte decomposition due to a series of electrochemical or side reactions. These characterization techniques can be divided to *ex-situ*, *in-situ*, and *in-operando*. In *ex-situ* techniques, the sample should be taken out of the cycling cell and characterized in another apparatus. When the cycling of the battery is paused and the characterization method is run, the technique is called *in-situ* characterization. *In-operando* methods characterize samples during cycling. This type of method can provide more information about the electrochemical reactions during the cycling process. However, preparing a setup to run according to an *in-operando* technique is very complicated. Below, a number of the methods commonly used for characterization of rechargeable batteries are introduced.

1.4.1. Cyclic Voltammetry and Galvanostatic Cycling with Potential Limitation

Cyclic voltammetry (CV) is one method to measure the kinetics of electrochemical reactions at the electrode surface. This technique consists of triangular waveforms where potential linearly changes from E_1 to E_2 and sweep back to E_1 again. The ratio of the potential differences (ΔE) to the time is called the scan rate. During the potential sweep, the current is recorded and the variation of the current versus the potential can be plotted. This technique provides valuable information about the reversibility of the reaction, the redox potentials, and a rapid estimation of the rate constant for electron transfer [73].

Another classic electrochemical method for electrode characterization is galvanostatic cycling with potential limitation (GCPL). In this technique, a constant current is imposed on the electrode and the variation of the potential during an amount of time is measured. This process is very useful for battery tests, especially under realistic conditions in which batteries are charged and discharged under constant current. The specific capacity, thermodynamic equilibrium potential, kinetic overpotential, capacity retention, and coulombic efficiency of a battery can be extracted easily via this technique [74].

1.4.2. X-ray Photoelectron Spectroscopy (XPS)

X-ray photoelectron spectroscopy (XPS) is one of the most effective techniques for accomplishing surface analysis. This method can be applied in both *ex-situ* and *in-situ* modes. In this method, high-energy X-ray photons with a penetration depth of ~50 Å hit the surface of the sample. The scattered photoelectrons are then trapped by the analyzer and sent to the detector.

Due to the different kinetic energies of the scattered photoelectrons, XPS is able to recognize all of the elements (except H and He) on the surface of the electrode. Therefore, valuable information about the surface composition of the electrodes before and after cycling can be obtained. However, due to the utilization of highly energetic photons, the risk of radiation damage or composition change on the surface of the electrode is very high. Moreover, due to spectra-shifting, calibration of the spectra is very complicated for non-conducting samples. In addition, the interpretation of XPS data is very tricky and requires a list of good reference values [75].

1.4.3. X-ray Diffraction (XRD)

XRD is an analytical method used to determine the crystal structure of materials. In this process, the incident x-ray beam is diffracted at different angles, based on the structure of the material. By using x-ray analysis, phase composition of an electrode, unit cell parameters, and Bravais lattice symmetry, the crystal size and quality, percentage of electrodes' crystallinity, and residual strain and stress can all be evaluated. This technique can be performed either *ex-situ* or *in-situ* [76].

1.4.4. Scanning Electron Microscopy (SEM)

SEM is one of the most pervasive techniques for microstructure morphology and chemical composition characterization. In this method, the interaction between the specimen and high energy electrons leads to image formation. SEM can be applied as an *ex-situ* and *in-situ* technique in the field of rechargeable batteries when comparing the surface morphology of electrodes before, during, and after cycling [77,78]. Any surface degradation and/or exfoliation, dendrite formation, and electrodeposition can be observed via high-resolution SEM [75].

1.4.5. Atomic Force Microscopy (AFM)

Atomic force microscopy can be applied *in-situ* to characterize the surfaces of electrodes. In this method, a tip is attached to a cantilever and the surface of the electrode is scanned. Based on forces between the tip and the surface, the tip is deflected and a surface image is formed. This method can be used to study variations in the surface before, during, and after intercalation/deintercalation. This method can also be used to study SEI formation [79].

1.4.6. Scanning Electrochemical Microscopy (SECM)

SECM is a probe technique that uses a microelectrode as a tip to measure the current of electrochemical reactions. The tip scans the surface in very close proximity of sample. The interaction between the tip and the surface creates an electrochemical perturbation that provides valuable information about the surface of the specimen. SECM can be used to determine electron transfer kinetics, corrosion, crystal dissolution reactions, and micromachining. This technique has been used for studying SEI formation in lithium-ion batteries, based on organic electrolytes [80].

1.4.7. Electrochemical Impedance Spectroscopy (EIS)

EIS is a technique in which several different properties of electrodes and electrolytes such as solid state and/or liquid diffusion, charge transfer resistance, and charge accumulation at the interface can be quantified. The working principle of this technique is the superimposition of a small AC potential onto a constant DC potential. Impedance is characterized by the magnitude, $|Z|$, which is the ratio between the amplitude of the AC voltage to the AC current, and phase shift, φ, between the AC current and the AC potential. In a battery system, a three-electrode cell configuration should be used for access to the features of a single electrode. Thus, employing a good reference electrode is mandatory. Reversibility, reproducibility, and non-polarizability are the most important features of the ideal reference electrode in EIS measurements. Recently, dynamic impedance spectroscopy has been developed; this allows researchers to acquire impedance spectra while the batteries are cycled. Hence, EIS can now be applied both *in-situ* and *in-operando* [81].

1.4.8. Differential Electrochemical Mass Spectrometry (DEMS)

One of the most appropriate *in-operando* analytical techniques used to study the aging mechanisms of batteries and gas evolution during electrochemical reactions is DEMS. In this technique, mass spectrometry is coupled with an electrochemical method (typically CV and GCPL); this allows for the investigation *in-operando* of the formation of gaseous or volatile species. This method is widely applicable to different demands such as electro-oxidation of adsorbed CO on the surface of the catalyst, oxidation of ethanol and methanol on various substrates, and battery analysis [81]. In the third chapter of this dissertation, a complete overview of DEMS applications for battery characterization is presented.

1.5. Aim of the Work

As has already been discussed, hydrogen evolution and the low electrodeposition efficiency of zinc are significant drawbacks to the development of aqueous zinc-ion batteries. To eliminate these problems, a better understanding of the electrochemical reactions that occur during cycling is required. Moreover, a number of modifications to the constituents of the electrolytes and electrodes should be implemented.

To do so, three different strategies was considered for this dissertation. First, a novel electrochemical cell has been designed to investigate the gas evolution in aqueous and organic electrolytes *in-operando*. Development of this technique will allow for a more detailed examination of the main and side electrochemical reactions that occur during battery cycling, upon which the final performance is highly dependent. In second part, this work addresses the effects of an organic additive on the efficiency of zinc electrodeposition. Organic additives play an important role in the modification of surface roughness, grain size, and growth mechanism of electrodeposited layers [82,83]. Organic additives can also increase cathodic overpotential, elevate surface polarization, and suppress the kinetics of zinc electrodeposition [84,85]. Herein the effects of the presence of branched polyethyleneimine (BPEI) as an additive in the electrolyte on the efficiency of zinc electrodeposition, as well as the morphology of the electrodeposited layers, are reported. Additionally, this work considers the application of layered double hydroxide (LDH) as a substrate for zinc electrodeposition. Finally, water-in-salt solution is employed to improve the electrochemical stability window of the electrolyte. In sum, this work investigates the interactions between electrolytes and negative electrode, in order to design a proper remediation for improving energy efficiency and cycle life.

2. Experimental Methods

2.1. Materials and Instruments

Table 2-1 provides general information about the materials used to fabricate the cell and develop a setup for the DEMS measurements.

Table 2-1: Materials Used to Fabricate the Cell and Develop a Setup for the DEMS Measurements

Component	Supplier	Size/Description
Bushing & Ferrules	Macherey Nagel GmbH & Co	1/16 inch
PPS Nuts	Macherey Nagel GmbH & Co	1/4 - 28 inch
PEEK Nuts & Double Ferrules	Macherey Nagel GmbH & Co	10-32
O-ring NBR 70	O-ring	21.95 × 1.78 mm, 25 × 3 mm 3 × 1 mm
PEEK Tubes	Macherey Nagel GmbH & Co	OD = 1/16 inch ID = 0.5 mm
Polyether Ether Ketone (PEEK) Rod	Goodfellow	Outer Diameter (OD) = 50 mm Half-crystalline
Plug, Long Hex	Macherey Nagel GmbH & Co	10-32, 1/4 - 28 inch
PTFE Film	Goodfellow	Thickness = 0.263 mm Porosity = 51.5%
Separators	Whatmann TM, GE Health Care	GF/A, Glass microfiber filter
Stainless Steel AISI 303	Edelstahlhandel HARRY RIECK	OD = 3 mm As current connector
Small Springs (D-60A)	Gutekunst Federn	OD = 3.2 mm
Glassy Carbon SIGRADUR G Rods	HTW GmbH	OD = 3 mm As current connector
Titanium Rod	Goodfellow	OD = 3 mm As current connector

To run the experiments for this research, different devices and software were applied. General information on these devices is provided in Table 2-2.

Table 2-2: Devices and Software

Name of Device/Software	Supplier	Description/Model
Balance	Kern	EMB 100-3
Centrifuge	Andreas Hettich GmbH & Co.	Universal 320 R
Color 3D Laser Microscope	Keyence	VK-9710K
Energy Dispersive X-ray Spectroscopy	Oxford Instruments	EDS, X-Max 80 Energy Dispersive X-ray SD-Detector
Inventor 2016 (software)	Autodesk	To design a cell
Glove Box Workstation	Mbraun	MB-200B
Mass Flow Controller	Alicat Instruments	0-0.5000 sccm, 0-2.000 sccm
Mass Spectrometer	Pfeiffer-Vacuum	Thermostar GSD 320
Mass Spectrometer Software	Pfeiffer-Vacuum	Quadera
Oven	Thermo Fisher Scientific	Heratherm OM H60
Potentiostat	Biologic	VMP-3, SP 200
Potentiostat Software	Biologic	EC-lab
SEM	Phenomworld	Phenom Pro X
SEM	FEI	Helios NanoLab^{TM} 600 DualBeam^{TM}
Silica Capillary	A-Z Analytic-Zubehör GmbH	150UM/220UM VSD Tubing
Stirring Hot Plate	IKA	RHD
Ultra-turrax Disperser	IKA	To mix the slurries
Vespel Ferrule	A-Z Analytic-Zubehör GmbH	GVF16-003
XRD	Rigaku	Miniflex 600

2.2. Chemical Components

A list of chemical components used in this research can be found in Table 2-3.

Table 2-3: List of Chemical Components

Chemical Component	Supplier	Description
Metals and Compounds as Active Materials for Electrodes		
Lithium Ribbon	Sigma Aldrich	Purity: 99.9%
Zinc Powder	Sigma Aldrich	Purum Powder
Zinc Sheet	Goodfellow	Purity: 99.99% Thickness: 0.125 mm
Zinc Rod	Vitalation	Purity: 99.999%
Lithium Iron Phosphate (LFP)	MTI Corporation	High Rate LFP Powder for Cathodes
Additives for Electrode Preparation		
Carbon Black	Timcal	Super C65
Polyvinylidene Fluoride (PVDF)	Solvey	Solef S5130
NMP	Sigma Aldrich	ACS Reagent, Assay > 99%
Chemical Compounds to Prepare Solutions, Electrolytes, and LDH Electrodes		
Aluminum Nitrate Nonahydrate $Al(NO_3)_3 \cdot 9H_2O$	Sigma Aldrich	Purity > 98%
Branched Polyethyleneimine Solution (BPEI)	Sigma Aldrich	Molecular Weight ~ 800 g mol^{-1}
Copper Nitrate Tetrahydrate, $Cu(NO_3)_2 \cdot 3H_2O$	Sigma Aldrich	Purity > 99%
Lithium bis(trifluoromethanesulfonyl)imide (LiTFSI)	Solvionic	Purity > 99%
Nitric Acid, HNO_3	Sigma Aldrich	Purity > 65%
Potassium Ferricyanide $K_3Fe(CN)_6$	Sigma Aldrich	Purity > 97%
Potassium Nitrate, KNO_3	Sigma Aldrich	Purity > 99%
Sodium Carbonate Decahydrate, $Na_2CO_3 \cdot 10H_2O$	Sigma Aldrich	Purity > 99%
Sodium Hydroxide, NaOH	Sigma Aldrich	Purity > 98%
Zinc Nitrate Hexahydrate, $Zn(NO_3)_2 \cdot 6H_2O$	Sigma Aldrich	Purity > 98%
Zinc Sulfate Monohydrate, $ZnSO_4 \cdot H_2O$	Sigma Aldrich	Trace Metal Basis Purity > 99.9%
1 M $LiPF_6$ in EC/DMC: 1/1 Solution	BASF	
Carbon Cloth	Fuel Cell Earth	As Current Collector

2.3. Synthesis of Materials

2.3.1. Synthesis of Copper Hexacyanoferrate (CuHCF)

The copper hexacyanoferrate was synthesized via a co-precipitation method, as in [86]. Simultaneously and at room temperature, 100 mM of $Cu(NO_3)_2.3H_2O$ (120 mL) and 50 mM of $K_3Fe(CN)_6$ (120 mL) were added dropwise to 60 mL of H_2O, while vigorously stirring. A brown precipitate formed immediately. After sonication for 30 minutes, the suspension was kept overnight. The precipitate was centrifuged and washed with a solution containing 1 M of KNO_3 and 10 mM of HNO_3, dried at 60°C, and ground. Figure 2-1 schematically illustrates the preparation procedure.

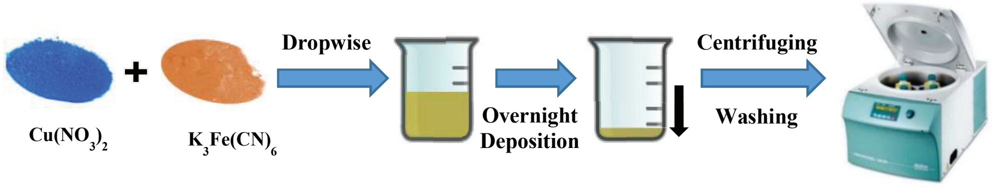

Figure 2-1: Procedure to synthesize the copper hexacyanoferrate.

2.3.2. Synthesis of Zinc Hexacyanoferrate (ZnHCF)

The zinc hexacyanoferrate was synthesized via a co-precipitation method, as in [87]. To prepare Solution A, 2 millimoles of zinc sulfate monohydrate was dissolved in 200 mL of deionized water; to prepare Solution B, 2 millimoles of potassium ferricyanide was dissolved in 200 mL of deionized water. Then, these solutions were simultaneously added at room temperature to an empty beaker, while vigorously stirring. The suspensions were kept overnight after being stirred for 24 hours at room temperature. The precipitate was then centrifuged and washed with water, dried at 60°C, and ground.

2.3.3. Synthesis of Layered Double Hydroxide (LDH)

The layered double hydroxide was prepared via a co-precipitation method at a constant pH. To do so, an aqueous solution (100 mL) of zinc nitrate hexahydrate, copper nitrate tetrahydrate, and aluminum nitrate nonahydrate, with a Zn:Cu:Al molar ratio of 2.8:0.2:1 and a total metal ion concentration of 0.25 M, was added to 50 mL of distilled water in a round-bottom three-neck flask. The process was performed at 65°C, with vigorous stirring. The flow rate of adding the solution to the water was set to 5 mL min^{-1} and the pH of the solution inside the flask was controlled to be within the range of 9.9 to 10.1. Controlling the pH was done by adding an alkaline solution (100 mL) of sodium carbonate decahydrate (0.0125 mol) and sodium hydroxide (0.05 mol). After stirring for 30 minutes, the product was transferred to a high-pressure 120 mL Teflon-lined autoclave at 120°C for 10 hours. The product was then cooled to room temperature. After that, it was centrifuged at 4,000 rpm and washed four times with deionized water until the pH reached 7. Finally, the product was dried for 24 hours at 60°C and ground to a fine powder.

2.3.4. Branched Polyethyleneimine Solution (BPEI)

The BPEI purchased from the company was very viscous. Therefore, it was not possible to add the BPEI directly to a solution. To solve this problem, 1 mL of BPEI was mixed with 199 mL of deionized water, and this solution was used to prepare the solutions of 500 mM of zinc sulfate, containing different concentrations of BPEI that ranged from 10 to 300 ppm.

2.4. Electrode Preparation

Lithium ribbons, zinc rods, and zinc sheets were all used as they were received from the company, without any further preparation.

The slurries of CuHCF, ZnHCF, and LFP electrodes contained 80wt% of the active material, 10wt% carbon black C65, and 10wt% PVDF binder solution in NMP (25 mg mL^{-1}). These components were mixed for 30 minutes at 4,000 rpm, using an ultra-turrax disperser. The electrodes were prepared by hand-painting on carbon cloth, which acted as a current collector; they were then dried in an oven for 5 hours at 60°C. The zinc slurry contained 96wt% of zinc powder, plus 4wt% of binder. Due to the good conductivity of zinc, the addition of carbon black was unnecessary.

The sum of the weight percent of the two main components in the slurries of the electrodes containing zinc and LDH was 90wt%. The rest of the slurries was 10wt% PVDF binder solution in NMP (25 mg mL^{-1}). These constituents were mixed for 30 minutes at 4,000 rpm, using an ultra-turrax disperser. The electrodes were prepared by hand-painting on carbon cloth, which acted as current collector; they were then dried in an oven for 5 hours at 60°C.

2.5. Electrochemical Cells

DEMS Electrochemical cells designed and fabricated for this research were used to study gas evolution in organic and aqueous solutions. A detailed description of the fabrication process and different materials used for the cells can be found in Chapter 3.

A conical cell was used to study the effects of additives on the electrodeposition efficiency of zinc and application of LDH as a negative electrode in aqueous zinc-ion batteries. A picture of this cell is shown in Figure 2-2.

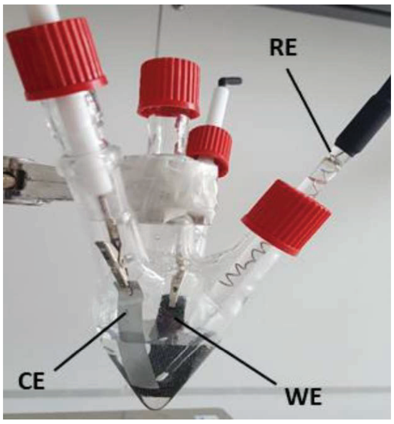

Figure 2-2: Conical cell for electrochemical measurements and characterization. WE: working electrode, CE: counter electrode, and RE: reference electrode.

A special electrochemical cell was used to study the electrochemical stability window of the water-in-salt electrolyte, as shown in Figure 2-3.

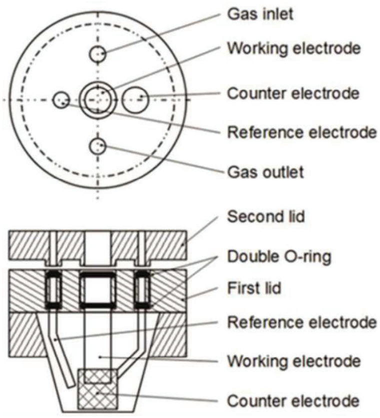

Figure 2-3: An electrochemical cell used to study the stability window of the electrolyte.

3. Differential Electrochemical Mass Spectrometry (DEMS)

3.1. An Introduction to DEMS

Analyzing gas evolution in battery systems that is caused by decomposition of an electrolyte or other side reactions is of fundamental importance to improving the long-term performance and cycle life of batteries. In general, this phenomenon can simultaneously lead to irreversible charge loss, chemical short circuit, and bulk or surface degradation of materials, as well as an increase in internal resistance [88–91]. The predictable result is a lowering of the energy and charge efficiency of storage systems.

One useful analytical methods for studying gas evolution in batteries is differential electrochemical mass spectrometry (DEMS) [92]. In this technique, mass spectrometry is coupled with an electrochemical characterization method, typically cyclic voltammetry, to investigate *in-operando* the formation of gaseous or volatile species. This process is widely used for different applications such as electro-oxidation of adsorbed CO on the surface of a catalyst [93,94], oxidation of ethanol and methanol on various substrates [95,96], and characterization of batteries containing organic electrolytes [88–90,97–99]. There are different kinds of DEMS setups. Among them, the most common for batteries is using a carrier gas to observe gas evolution. In this setup, an inert gaseous compound is continuously purged into an electrochemical cell, bringing volatile products to the mass spectrometer.

A mass spectrometer is an apparatus in which partial pressure measurements of gaseous species are measured and used in an analysis of the chemical composition of a product [100]. To determine the partial pressure of a single component, it must be isolated from the others. To accomplish this, a high vacuum atmosphere is required. When in this condition, each single component can be distinguished from the others based on the mass to charge ratio.

To analyze the gas, it is introduced to the mass spectrometer through an inlet system. Usually, a capillary made of silica brings the gas into the system. Thereafter, an ion source bombards the gas with high-energy electrons and generates different ions from the gaseous species with different mass to charge ratios. These ions are filtered based on their mass to charge ratio using a quadrupole mass spectrometer. This filtering system consists of four parallel cylindrical slabs that each pairs of opposite rods is connected to each other. In the ideal case, these pairs must have a hyperbolic profile rather than a cylindrical shape, which is not common in experimental conditions. Electrical voltage (U_{qaud}) is applied via rods that consists both DC and AC portions. The AC portion has the amplitude of V and the angular frequency of ω.

$$U_{quad} = U + V.\cos(\omega t) \tag{3-1}$$

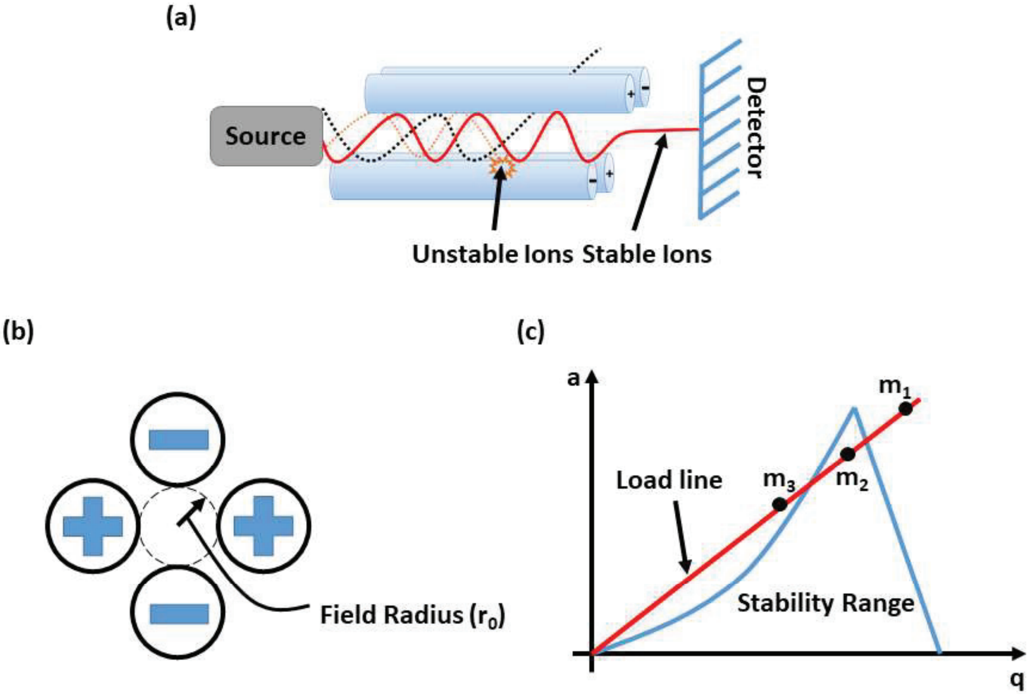

Figure 3-1: (a) A simple sketch of filtering system in quadrupole mass spectrometer; (b) Visual explanation of field radius (r_0); and (c) Stability diagram of a quadrupole filter.

The voltage generates an electric field in the area between the slabs that forces the ions to move in a spiral configuration. They move inside the filter along Z direction and deviate in X and Y directions. The speed of the ions and their deviation from their normal route depend upon the mass to charge ratio of each ion. If the amplitude of the deviation exceeds field radius (see Figure 3-1), the ions are filtered by discharging them onto the rods or the surrounding area; there, they cannot reach the detector. Otherwise, they will hit the detector at different times and at distinct positions.

To find the stability region of the quadrupole filter, two dimensionless parameters are introduced as “a” and “q”. These parameters can be defined as follows:

$$a = \frac{8\,.\,Q\,.\,U}{m\,.\,r_0^2\,.\,\omega^2} \tag{3-2}$$

$$q = \frac{4\,.\,Q\,.\,V}{m\,.\,r_0^2\,.\,\omega^2} \tag{3-3}$$

Where Q is the charge, U is the DC voltage, m is the mass, r_0 is the field radius, ω is the angular frequency, and V is the AC amplitude. The slope of the load line, which is indicated in Figure 3-

1(c) can be calculated by dividing these two equation by one another. This slope is equal to 2U/V. if the load line intersects the stability range of quadrupole filter, a triangle is formed (see Figure 3-1(c)). The ion can reach the detector, if the "a" and "q" parameters of that ion is located inside the triangle. Therefore, among three different points that are indicated in Figure 3-1(c), m_2 can reach detector. It should be noticed that in this Figure, m_1 is too light to pass the quadrupole filter. In the case of m_3, the AC voltage is too low to allow the ion to pass the filter and reach detector. Any ions above the red line in the area of stability range can reach the detector.

Subsequently, the data will be sent from the detector to the analyzer and the chemical component for each ion will be determined. As various gaseous species have different mass to charge ratios, the components can be separated as a function of space or time.

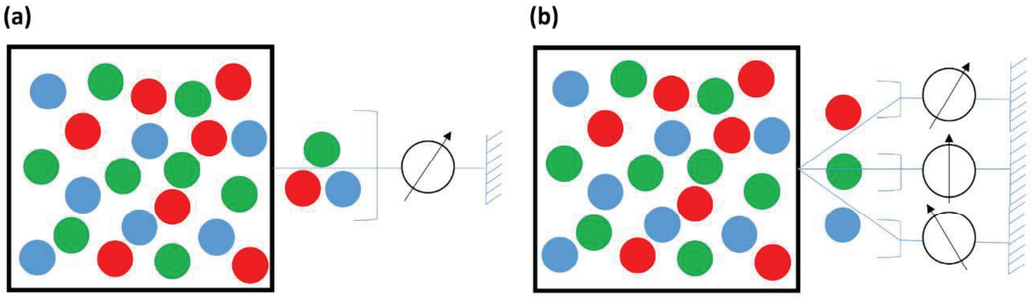

Figure 3-2: Gaseous species: (a) Without applying quadrupole filter: no separation of gaseous specie. They reach the detector at the same time and at the same location; and (b) With applying quadrupole filter: gaseous species are separated as a function of space or time, based on the mass to charge ratio.

Designing a DEMS cell for studying gas evolution during battery cycling is a significant step in performing such an experiment. Below is a brief discussion of DEMS applications in studying lithium-ion batteries with organic electrolytes. Next, the design and validation of a cell for DEMS measurements is discussed. Finally, DEMS applications in studying aqueous metal-ion batteries are introduced.

3.2. Application of the DEMS Method to the Study of Rechargeable Batteries: An Overview

Applications of DEMS in studies of rechargeable batteries dates back to 1997, when Petr Novak and Roman Imhof used a DEMS method to study the degradation of mixed carbonate electrolytes on a graphite electrode in a lithium-ion battery [101]. By applying this procedure, they demonstrated that in an electrolyte containing a mixture of ethylene carbonate (EC) and dimethyl carbonate (DMC), ethylene evolution occurs during the first reduction of the graphite electrode. This gas evolution was attributed to the electrochemical reduction of EC. They also found that the purity of the electrolyte is an important parameter in hydrogen evolution. In particular, a high level of water as an impurity in the electrolyte increases a battery's irreversible capacity fade [102]. One year after that study, they detected CO_2 evolution on the surface of lithium metal oxides such as $LiNiO_2$, $LiCoO_2$, and $LiMn_2O_4$, in electrolytes based on propylene carbonate (PC). They argued that this gas was produced as a result of the decomposition of the electrolyte [103].

Dominko et al. [104] used DEMS to investigate the effects of gelatin as a pretreatment material in lithium-ion batteries. Their research showed that although gelatin leads to CO_2 evolution in the EC:DMC electrolyte, it can also reduce irreversible charge loss. They believed that the origin of CO_2 evolution is a side reaction between the gelatin compound and degradation products from decomposition of the electrolyte.

Spahr et al. [105] employed DEMS in a study of the effects of heat treatments on the exfoliation of graphite electrodes. These researchers analyzed the level of ethylene and CO_2 evolution on an electrode during the first cycle. Based on the results, they supposed that heat treatments can lead to different passivation mechanisms and electrolyte decomposition in electrolytes in which ethylene carbonate is one of the major ingredients. They concluded that the pretreatment of an electrode can reduce surface activity for forming an SEI layer; the result is an increase in graphite exfoliation. In another study [106] Buqa et al. used DEMS to investigate the formation of a passivation layer on a highly crystalline graphite in a propylene carbonate electrolyte. The results showed that a high surface crystallinity may provide less proper positioning on the surface of an electrode that energetically favors the formation of a passivation layer. Thus, graphite with a low surface crystallinity is more stable than high crystalline graphite in an electrolyte containing propylene carbonate.

This technique had been also used to investigate the effects of an additive on battery performance. For instance, the effects of vinylene carbonate (VC), an additive in EC/PC/EMC electrolytes, on gas evolution in lithium-ion batteries was analyzed via a DEMS process [88]. This study showed that the presence of VC in an electrolyte can suppress gas evolution in a battery, especially at high voltages and temperatures. The same results were presented by Wuersig et al. [89]; the production of oxidative CO_2 was confirmed by a DEMS process. Moreover, these researchers demonstrated that temperature, solvents, and VC additives, as well as the types of oxide used as cathode material, all strongly affect CO_2 evolution. Subsequent to that research, Li et al. [107] presented evidence of the positive effect of adding vinyl ethylene carbonate (VEC) to a EC/DMC electrolyte on the high-temperature performance of lithium-ion batteries composed of $LiNi_{0.8}Co_{0.2}O_2$ as the positive electrode and lithium as the negative electrode. Their results indicated a 15% enhancement in capacity retention after 100 cycles. They also showed that the amplitude of CO_2 evolution was markedly decreased by adding VEC to the electrolyte, which guaranteed the formation of a stable SEI layer on the surface of the electrode. Finally, Zhang et al. [108] simultaneously employed vinylene carbonate and propane sultone (PS) as additives to an electrolyte. Their results suggested that these additives suppressed the gas evolution during SEI formation, which is of primary importance to faster and easier battery production.

Freiberg et al. [109] studied the effects of Trimethylboroxine (TMB) as an electrolyte additive on the performance of lithium-ion batteries in which $LiCoPO_4$ is the positive electrode. Using DEMS, they determined that a low level of TMB, in the range of 0.5 wt%, can enhance the performance of the electrode. Moreover, they found that the electrode oxidized at approximately 4.6 V and produced phosphorylfluoride (POF_3), boron trifluoride (BF_3), and carbanion (CR_3^-). They argued that the TMB decomposition accelerated SEI formation, due to the rapid polymerization of the carbonates.

La Mantia et al. [110] employed a DEMS technique to study oxygen evolution in $Li_{1+x}(Ni_{1/3}Mn_{1/3}Co_{1/3})_{1-x}O_2$ (NMC) at high voltages. They compared oxygen evolution in stoichiometric and overlithiated compounds, finding that oxygen evolution occured during the first cycle of an overlithiated compound. Oxygen molecules may have formed as a result of oxygen loss from the lattice structure. For stoichiometric compounds, no evidence of oxygen evolution could be found. The researchers also determined that in lithium-rich mixed-metal layered oxide with a general formula of $xLi_2MnO_3 \cdot (1-x)LiMO_2$ in which M could be nickel, cobalt, or manganese, oxygen evolution took place in the first cycle such that it could increase the internal pressure of the battery and decrease its performance [111]. Thereafter, Castel et al. [98] proposed a gas evolution mechanism for the same cathode as was used in La Mantia's study, at high voltage. They supposed that the presence of oxygen in the structures of these materials enhanced the oxidative decomposition of the electrolyte at high voltages. They also detected CO_2 evolution during the first cycle, due to the oxidative decomposition of ethylene carbonate.

The stability windows of three different electrolytes, named EC/DMC, EC/DEC, and PC, were also examined by a DEMS method [112]. All of these solvents contained 1 M of $LiPF_6$, and $LiNi_{0.5}Mn_{1.5}O_4$, $LiMn_2O_4$, and $LiCoO_2$ were used as the working electrodes. The results showed that these electrolytes decomposed at high voltages and evolved O_2 and CO_2. Among them, EC/DMC was the most stable, in combination with the aforementioned electrodes. Moreover, the active material in the positive electrode had a significant effect on the stability window of the different electrolytes. For instance, application of $LiNi_{0.5}Mn_{1.5}O_4$ as a positive electrode in EC/DMC showed a stable condition up to 5 volts. Therefore, it was concluded that to find a precise stability window for each electrolyte, an appropriate cathodic material must be utilized.

In 2015, Bernhard et al. [113] performed a series of experiments to study the effects of traces of water on gas evolution from a graphite electrode in lithium-ion batteries. Their results were in complete agreement with the outcomes produced by Novak and Imhof in 1997 [101]. They showed that controlling the level of water inside an EC-based electrolyte to be less than 20 ppm had a substantial effect on the behavior of gas evolution during cycling. In this condition, ethylene was formed due to the decomposition of ethylene carbonate in the first cycle; also, a negligible amount of hydrogen was observed. When the amount of water in the electrolyte exceeded 4,000 ppm, hydrogen evolution occurred continuously after the first cycle. Moreover, the presence of water in the aforementioned range enhanced the anodic oxidation of the conductive carbon black in the electrode or oxidation of the electrolyte [114].

DEMS has also been applied in studies of the effects of temperature on the degradation mechanism of electrolytes. He et al. [90] employed this technique to examine the electrolyte degradation in electrodes based on $Li_4Ti_5O_{12}$ (LTO), at high temperatures. They found that the intensity of the gas evolution was increased at high temperatures, which was related to the fast decomposition of the electrolyte. Since no SEI layer formed on the surface of the LTO, ethylene evolution was observed after the first cycle. It was also recognized that the nature of anions played a significant role in the gas evolution. In other words, changing the $LiPF_6$ salt to $LiClO_4$ dramatically reduced the intensity of the gas evolution. Thus, DEMS could be used to study the effects of different salts on the decomposition of the electrolyte.

Recently, Metzger et al. [115] carried out an analysis to determine the reason for hydrogen evolution in graphite half cells and graphite-NMC full cells. These researchers proposed that the hydrogen evolution could be explained as follows:

1- Diffusion of protic electrolyte oxidation species ($R\text{-}H^+$) from the cathode to the anode.

2- Reduction of protic electrolyte oxidation species on the anode.

As has already been mentioned, DEMS can be employed to study gas evolution in both half and full cells. In a study carried out by Michalak et al. [116], this method was applied to analyze gas evolution in full cells. They used $LiNi_{0.5}Mn_{1.5}O_4$ (LNMO) as the positive electrode and graphite as the negative electrode. They found that CO_2 evolution occurred on the positive electrode, while hydrogen and ethylene formed mainly on the negative electrode. In addition, the role of Ni^{3+}/Ni^{4+} redox couple in the production of CO_2 was confirmed. In another investigation of the same material, the effects of solvent, lithium salt, and temperature on the degradation of carbonate-based electrolytes was examined [117]. The electrolyte was composed of EC/DMC: 1/1 + 1 M $LiPF_6$. The results showed that increasing the portion of DMC in the electrolyte led to higher levels of gas evolution. This was attributed to the lower viscosity of the DMC, which enhanced the mass transport in the electrolyte. Furthermore, high temperatures and the nature of salt increased the rate of electrolyte decomposition.

All of these studies illustrate the substantial role of DEMS in characterizing electrochemical and side reactions in lithium-ion batteries. In brief, DEMS can be used to study the following aspects of rechargeable batteries:

1- Degradation mechanism of electrolytes at low, moderate, and high potentials.

2- Effects of various parameters such as electrolyte additives and impurities, solvents, salts, and temperature on electrolyte decomposition.

3- Effects of the surface roughness of the working electrode on electrolyte decomposition.

4- Effects of electrode heat treatments on electrolyte decomposition.

5- Investigation of the stability windows of different mixtures as organic electrolytes.

It can be deduced from this brief overview that differential electrochemical mass spectrometry is a valuable technique for characterizing electrochemical and side reactions during battery cycling. The results of this *in-operando* method can provide a better understanding of the processes occurring during the operation of metal-ion batteries. Further development of this technique will allow for more detailed information to be gathered about the reactions that occur during battery cycling, upon which the final performance of the device is highly dependent. One of the important components of DEMS process is the electrochemical cell in which all electrochemical reactions are performed. This electrochemical cell must fulfill various requirements that will be discussed in detail in the next section.

3.3. Electrochemical Cell Design and Validation of DEMS Measurements

A good electrochemical cell plays an important role in achieving favorable results in DEMS measurements. One of the first electrochemical cells to be used in DEMS measurements was introduced by O. Wolter and J. Heitbaum [118]. A schematic of this two-electrode cell is presented in Figure 3-3. In this type of cell, the working electrode is prepared by deposition of powdered materials onto the PTFE membrane. As a reference electrode, a platinum wire is used inside the cell. The electrolyte is added to the cell from the top, and gaseous products pass through the stainless steel frits during cycling, eventually reaching the vacuum chamber connected to the mass spectrometer. The advantages of this electrochemical cell for DEMS measurements include fast response and high efficiency. However, using more than 2 mL of the electrolyte for each experiment can be a disadvantage [119]. There are also other disadvantages to this design. For instance, due to the very short distance between the PTFE membrane and stainless steel frits, controlling the mass transport of the reactants is very difficult. This type of electrochemical cell is usually employed to study catalytic reactions.

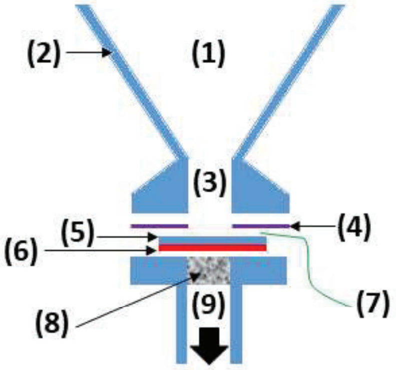

Figure 3-3: Classic DEMS cell developed by Wolter and Heitbaum: (1) Electrochemical cell, (2) Glass body, (3) Electrolyte, (4) PTFE spacer, (5) Working electrode material, (6) PTFE membrane, (7) Contact wire, (8) Stainless steel frits, and (9) Outlet to the vacuum chamber (reproduced from [119]).

In 1989, Tegtmeyer et al. [120] combined mass spectrometry with a rotating disc technique, developing a new rotating inlet system. This cell has also been used to study mass transport efficiency from, to, and inside a porous catalyst layer. One year later, a thin-layer flow cell was developed to study single or polycrystalline electrodes [121]. In this type of cell, a thin layer of electrolyte fills the space between the working electrode and membrane, which allows for different types of electrodes to be used. However, any gaseous products must diffuse from the surface of the electrodes to the electrolyte, and then reach the vacuum outlet. This results in an increase in response time. Moreover, the small volume of the cell does not allow for a location reference and counter electrode in the same chamber as the working electrode; they must be placed in another component.

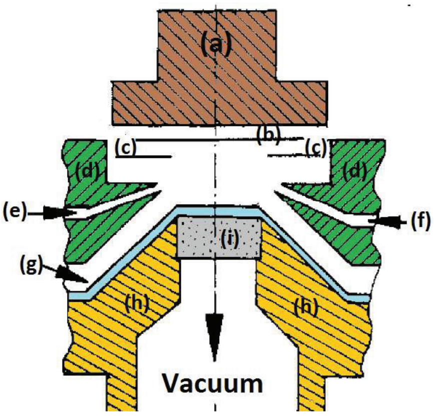

Figure 3-4: Schematic sketch of the thin-layer flow cell: (a) Body support for the electrode, (b) Platinum wire or sheet as the working electrode, (c) PTFE spacer, (d) Body of the thin-layer flow cell, (e) Electrolyte inlet, (f) Electrolyte outlet to the counter and reference electrode, (g) Porous PTFE membrane, (h) Cell body to connect to the vacuum chamber, and (i) Porous steel frit (reproduced from [121]).

Compared to the classic DEMS cell, this cell design provides a condition for controlling the flow of the electrolyte inside the cell. However, due to the outlet connection to the reference and counter electrodes, a part of the volatile species departs the cell before reaching the vacuum chamber. Therefore, the collection efficiency of such a cell, which is a ratio of the amount of the detected gaseous species to the total amount of produced gaseous species, is poor. To solve this problem, Baltruschat et al. [93] introduced a dual thin-layer flow cell design in which the flows of electrolyte into the inlet and outlet are separated from one another. This cell was developed to combine DEMS with an electrochemical quartz crystal microbalance (EQCM). Using this cell design resulted in a practical enhancement of the collection efficiency and an increase in response time over the previous cell design.

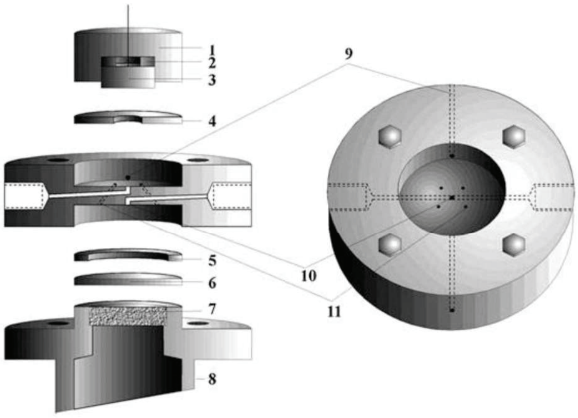

Figure 3-5: Dual thin-layer flow cell: (1) Body support, (2) Back support for the electrode, (3) Working electrode, (4,5) Teflon spacers, (6) Porous membrane made by Teflon, (7) Stainless steel frits, (8) Vacuum connection, (9) Holes for the argon flashing (10) Electrolyte inlet and outlet, and (11) Connecting holes [93].

To make the experiments more realistic, a cell with the same sized positive and negative electrodes was required. Moreover, these electrodes needed to be placed completely in front of one another. In addition, the porous membrane connected to the vacuum system had to be eliminated. These prerequisites led to the construction of the new DEMS cell design presented in Figure 3-6(b). In this design, an inert gas such as helium or argon was sent into the cell. This gas, together with the produced gaseous species, was continuously pumped off via a capillary into a quadrupole mass spectrometer. This design made possible the identification of much smaller quantities of gases. Furthermore, the cell could also be adapted for high-temperature measurements. Although the cell worked very well for the DEMS experiments, it could not provide electrochemical information about both electrodes. To have separate access to the features of each electrode, it is necessary to use a three-electrode cell configuration involving a reference electrode. Furthermore, new DEMS cells should be capable of working with an appropriate amount of electrolyte that can be compared to real batteries.

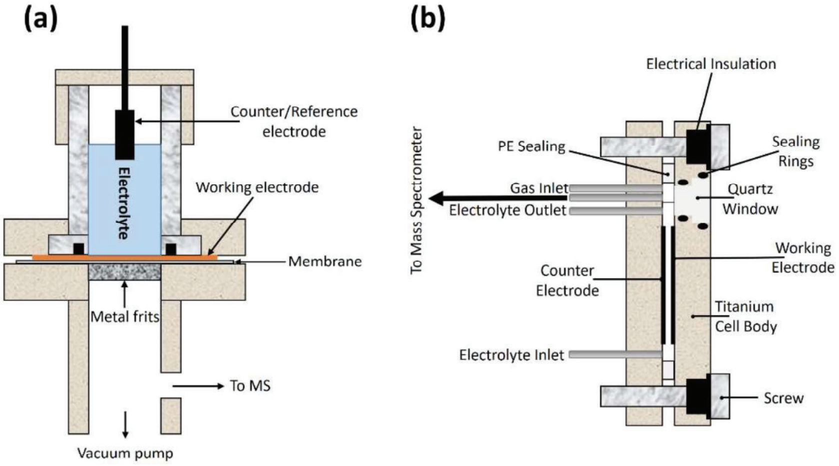

Figure 3-6: Schematic view of a DEMS cell for studying electrochemical and side reactions during the cycling of lithium-ion batteries using a: (a) Vacuum pump, and (b) Carrier gas (reproduced from [102,122]).

Figure 3-7 presents the new cell design, developed during this Ph.D thesis, for performing a DEMS experiments and classic electrochemical characterization measurements such as cyclic voltammetry, galvanostatic cycling with potential limitations, and EIS measurements in aqueous and organic electrolytes. The body of the cell was made completely of polyether ether ketone (PEEK; Goodfellow). This material is resistant to many organic solvents and aqueous solutions. The cell was composed of three separate main parts indicated in Figure 3-7 with the colors green, orange, and brown. The space between the green and orange parts, indicated by the number 1, was filled with electrodes and separators. The diameter of this area was equal to 14 mm which is similar to a real battery. The working electrode (WE), separator, reference electrode (RE), another separator, and counter electrode (CE) were all located in this space (from top to bottom, respectively). Each separator (Whatman™, GE Healthcare, UK) was wetted with 50 µL of the desired electrolyte during cell assembly. The total amount of electrolyte did not exceed 500 µL in each experiment. To achieve a good sealing of the connections in the inlet and outlet channels (numbers 5 and 6), PEEK nuts in a double ferrule configuration were used (MACHEREY-NAGEL GmbH & Co). Moreover, an O-ring (number 7) was employed around the intermediate part of the cell, in order to attain a proper seal. The sealing efficiency was evaluated by sending a 0.2 sccm (standard cubic centimeters per minute) flow of argon to the inside of the empty cell and measuring the output flow via a mass flow controller (Alicat Instruments). By using appropriate ferrules, nuts, and O-ring, a sealing of 85% was achieved.

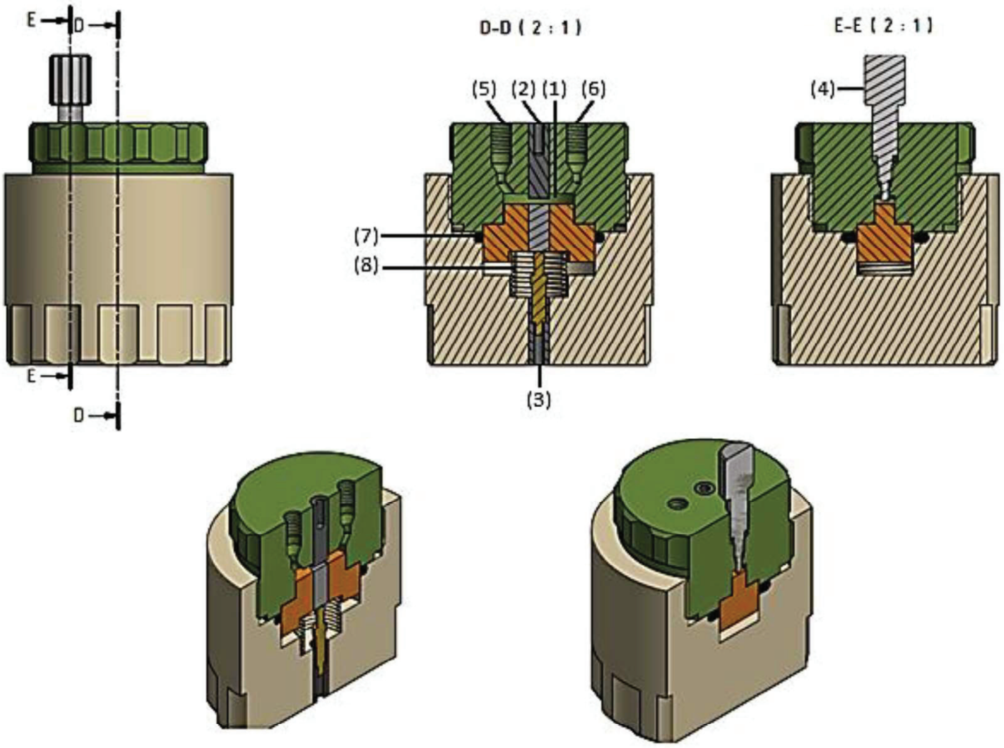

Figure 3-7: Schematic view of the DEMS cell: (1) Cavity for assembling the electrodes; (2-4) Stainless steel AISI 303 current connectors; (5-6) Gas inlet and outlet; (7) O-ring; and (8) Contraction spring.

To apply a constant external force to the electrodes during the experiment, the middle part of the cell, represented by the orange color, was mechanically supported by a contractive spring (indicated with a number 8). The current connectors (marked with numbers 2 through 4) were made of polished stainless steel AISI 303 (Edelstahlhandel HARRY RIECK). The working electrode was connected to the current connector from the top of the cell, and a counter electrode connection was constructed at the bottom. A reference electrode was located between the working and counter electrodes. Based on previous studies, assembling the reference electrode between the working and counter electrode was presumed to lead to more reliable results [123]. In this cell, the reference electrode had a circular shape with an external segment; this allowed for good contact with the current connector (shown with a number 4). The current connector of the WE entered 1 mm inside the cell. In general, this area needed to be filled with a membrane having the following characteristics:

1- Hydrophobicity, to prevent liquids from approaching the outlet channel.

2- Porosity, to allow gaseous and volatile species to pass through and reach the capillary of the mass spectrometer.

3- Permeability, to provide a rapid flow of gaseous species and avoid time-consuming diffusion resistance or capacitive effects inside the membrane.

Therefore, the area behind the WE was filled with polytetrafluoroethylene film (PTFE, Goodfellow) that provided all of the aforementioned properties.

In this study, ThermoStar^{TM} (Pfeiffer-Vacuum) was used to detect and analyze the outlet gaseous species from the DEMS cell. This type of mass spectrometer works properly if at least 1 sccm of gas flow is introduced to its capillary. If this flow is sent directly into the electrochemical cell, and from there to the capillary, evaporation of the electrolyte occurs very quickly. Moreover, this high flow of carrier gas may push the electrolyte towards the capillary and block it. To prevent these problems, a working setup using an auxiliary argon line next to the main line was designed. Different ratios of main to auxiliary carrier gas flows were examined; the best result was achieved when the flow of 0.2 sccm was sent to the main line and 1 sccm was sent to the auxiliary line. A schematic and real view of this setup is illustrated in Figure 3-8. For all connections between the experimental components, PEEK tubes with 1/16-inch outer diameters and 0.50 mm inner diameters (MACHEREY-NAGEL GmbH & Co) were used.

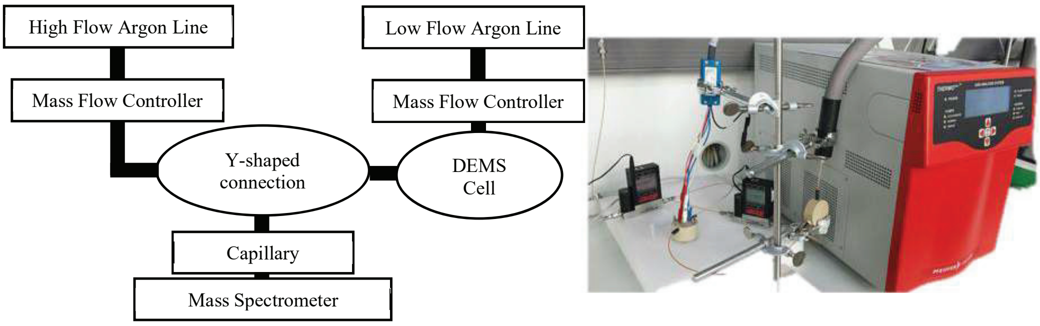

Figure 3-8: DEMS setup: (left) Schematic view, (right) Real setup.

It is also possible to use a humidifier in this setup. When the humidifier is added, the argon gas passes through the electrolyte before being sending into the cell. Thus, the carrier gas is completely saturated with the electrolyte, the partial pressure of the volatile species is increased inside the cell, and the rate of electrolyte evaporation is decreased. The schematic of this setup is shown in Figure 3-9.

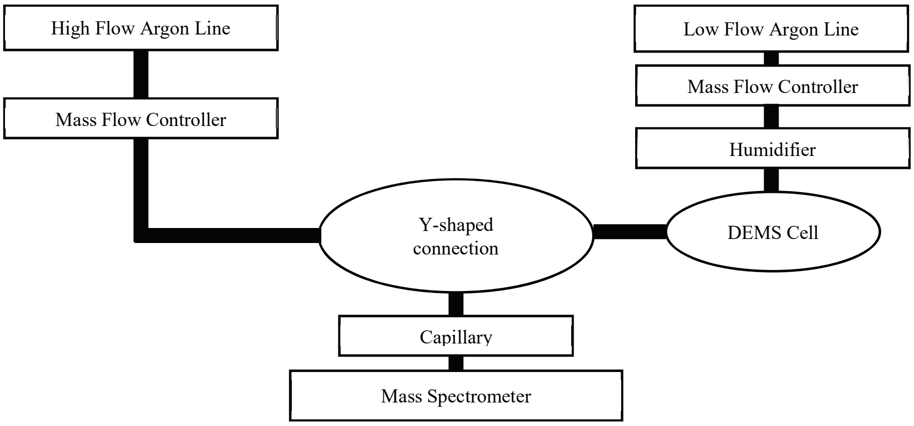

Figure 3-9: DEMS setup using a humidifier.

To validate the performance of the cell, it had to be tested with a well-known electrochemical reaction in a battery. Before that, the reliability of the cell needed to be examined via a high-frequency electrochemical impedance spectroscopy (EIS). This measurement was performed for proving the quality of the connection between the electrodes and metallic current collectors of the cell. To perform such an experiment, EIS measurements were carried out under three different sets of conditions. In all of the experiments, half-oxidized lithium iron phosphate (LFP) was employed as a reliable reference electrode [124]. The reason for using half-oxidized LFP as a reference electrode was related to its flat plateau during charging and discharging by a constant current. This kept it stable during the experiment and the potential from changing even if a tiny number of lithium ions were intercalated into the structure or adsorbed at the surface of the reference electrode during cycling.

To prepare the reference electrode, the LFP was reduced to 3 V vs. Li/Li^+, accompanied by oxidation up to 3.8 V and a second reduction down to 3 V. Finally, it was oxidized up to half of the practical capacity. Figure 3-10 represents the electrochemical procedure for the reference preparation. As mentioned above, three different experimental conditions were considered for the EIS measurements. In all cases, two similar electrodes, based on LFP, and called LFP1 and LFP2, were employed as working and counter electrodes. LFP1, RE, and LFP2 were located inside the cell from top to bottom, respectively.

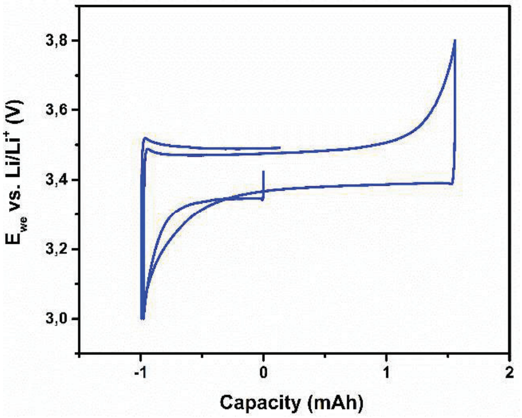

Figure 3-10: Flat plateau of LFP during charge and discharge.

Using one separator between each, three different EIS measurements were acquired, as follows:

1- LFP1 was employed as the working electrode and LFP2 as the counter electrode, labeled as LFP1-RE in Figure 3-11.

2- LFP1 was employed as the counter electrode and LFP2 as the working electrode, labeled as LFP2-RE in Figure 3-11.

3- A two-electrode configuration in which LFP1 was the working electrode and LFP2 was the counter electrode. The reference electrode was short-circuited with the counter electrode in this configuration. This experiment is labeled as LFP1-LFP2 in Figure 3-11.

From Figure 3-11 it can be seen that the impedance spectra of LFP1-RE and LFP2-RE were identical, with a shift in spectra along the x-axis. This shift could be considered as an experimental error stemming from the cell design. As indicated with the numbers 2 and 3 in Figure 3-7, the shape, size, and fabrication materials of the working and counter current connectors were not completely the same, which led to this experimental error. However, it should be stressed that although a shift in the spectra along the x-axis was observed, the shapes of the spectra of the two LFP electrodes were almost identical. This confirms that the cell was reliable for impedance spectra in high-frequency region. Moreover, high-contact resistance on one side of the cell did not influence the current density distribution inside the cell. Thus, it did not affect the impedance spectra recorded at the working electrode. From Figure 3-11, it can be seen that the sum of the spectra of LFP1 and LFP2 coincided with the impedance of the whole cell within the range of experimental error, confirming the reliability of the cell.

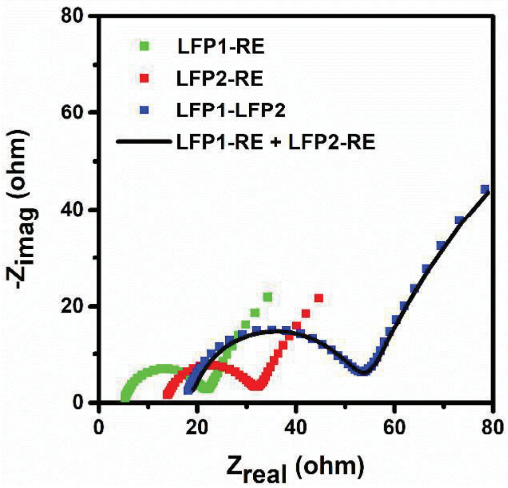

Figure 3-11: EIS measurements in the DEMS cell.

Subsequently, the ability to run DEMS measurements with this setup was evaluated by cycling the graphite as the working electrode versus metallic lithium as the counter electrode, using EC/DMC: 1:1, 1 M of $LiPF_6$ as the electrolyte. The reference electrode was half-oxidized LFP. Figure 3-12 presents the results of the DEMS measurements.

Figure 3-12(a) shows the cyclic voltammetry measurements of the graphite for the first four cycles. The potential changed from 1.5 to 0 V vs. Li/Li^+ in the first cycle, and increased up to 1 V vs. Li/Li^+ with a scan rate of 0.1 mV s^{-1} for subsequent cycles. During the first reduction, ethylene evolution occured in the potential range of 0.75 to 0.55 V vs. Li/Li^+. This was the range that the SEI layer formed on the surface of the graphite. Therefore, the ethylene evolution could be attributed to decomposition of the electrolyte and formation of the SEI layer. Moreover, hydrogen evolution was observed for all cycles, and the intensity of the peaks were almost equal. This hydrogen evolution, which was accompanied by a CO_2 evolution in the first cycle, could be attributed to the residual water inside the electrode. This residual water decomposed to H^+ and OH^- during the first reduction of the graphite electrode. Thereafter, the OH^- caused a ring opening of the ethylene carbonate molecules and reacted with them. This reaction produced alkyl di-alcoholates and CO_2. The latest could be detected with the mass spectrometer. These results matched well with the previous studies [99,113].

Thus, the DEMS cell's abilities and the appropriateness of the setup were confirmed through this experiment. This cell is able to run DEMS measurements with a cyclic voltammetry technique.

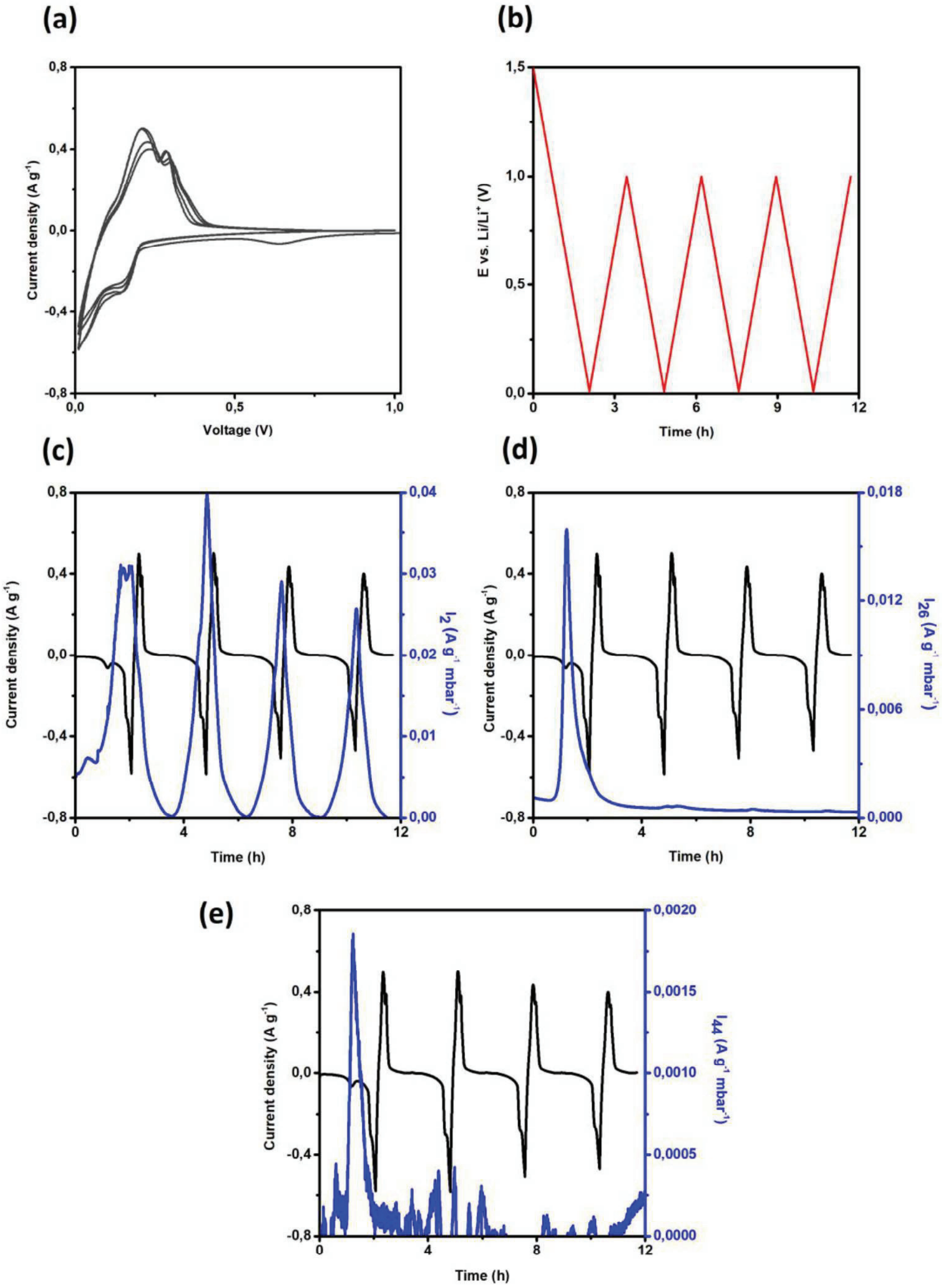

Figure 3-12: (a) Cyclic voltammetry (CV) measurement of graphite versus lithium for four cycles: (b) Potential variations in CV measurements versus time; (c) Hydrogen evolution; (d) Ethylene evolution; and (e) CO_2 evolution during CV measurements. In Figure (c-e), the black lines show the variations in current density during the cyclic voltammetry, and the blue lines show the variations in gas evolution.

The other aspect of the DEMS cell that needed to be confirmed was the performance of the cell under a constant current. This characteristic is important, because the batteries are being charged under a constant current in an operating condition. The gas evolution during the first discharge and charge of the graphite electrode under a constant current are illustrated in Figure 3-13. As expected, ethylene evolution occurred during SEI formation under a constant current. Figure 3-13(b) shows two distinct peaks in the hydrogen evolution. The first was related to the residual water decomposition inside the electrode, which produced H^+ and OH^-. In the next step, protons formed and evolved as molecular hydrogen, indicated as peak number 1 in Figure 3-13.

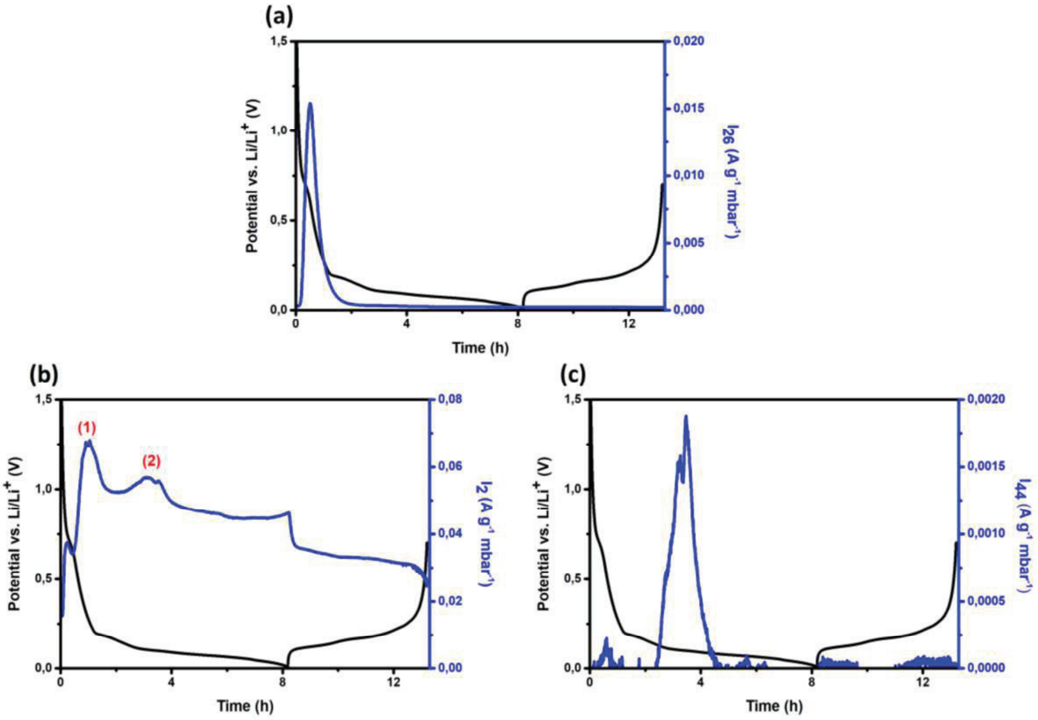

Figure 3-13: Gas evolution during the first charge and discharge of the graphite electrode under a constant current: (a) Ethylene evolution, (b) Hydrogen evolution, and (c) CO_2 evolution. The black lines show the potential changes during charge and discharge under a constant current, and the blue lines show the variations in gas evolution.

The formation of molecular hydrogen locally increased the concentration of OH^- on the surface of the electrode. These anions attacked the ethylene carbonate and opened the ring of ethylene carbonate molecules. After that, the OH^- anions reacted with the opened-ring ethylene carbonate, which led to CO_2 evolution. This reaction accelerated the decomposition of the residual water, and the second peak in the hydrogen evolution appeared in the DEMS data (as indicated with a number 2 in Figure 3-13). Therefore, the results of this experiment under a constant current completely matched with the results from the cyclic voltammetry measurements; thus, this cell can be employed in both CV and GCPL techniques.

Although the results obtained up to this point were considered reliable, more accurate data would require a geometric modification of the DEMS cell. For instance, the collection efficiency of this cell was equal to 85%, which could be improved. Moreover, the flow of the carrier gas into the cell could be changed from a vertical direction with respect to the surface of the electrodes to a parallel direction; this would result in a more homogeneous flow distribution of the carrier gas inside the cell. In addition, this DEMS cell was not symmetrical and the length and thickness of the current connectors were not identical. This means that the current connectors of the working, counter, and reference electrodes were not fabricated from thoroughly identical material with the same geometrical design. These differences introduced different resistances into the setup, which may have affected the results. For these reasons, some modifications were implemented in the electrochemical cell, and a second version of the DEMS cell was fabricated. Figures 3-14 to 3-16 represent this second version of the DEMS cell.

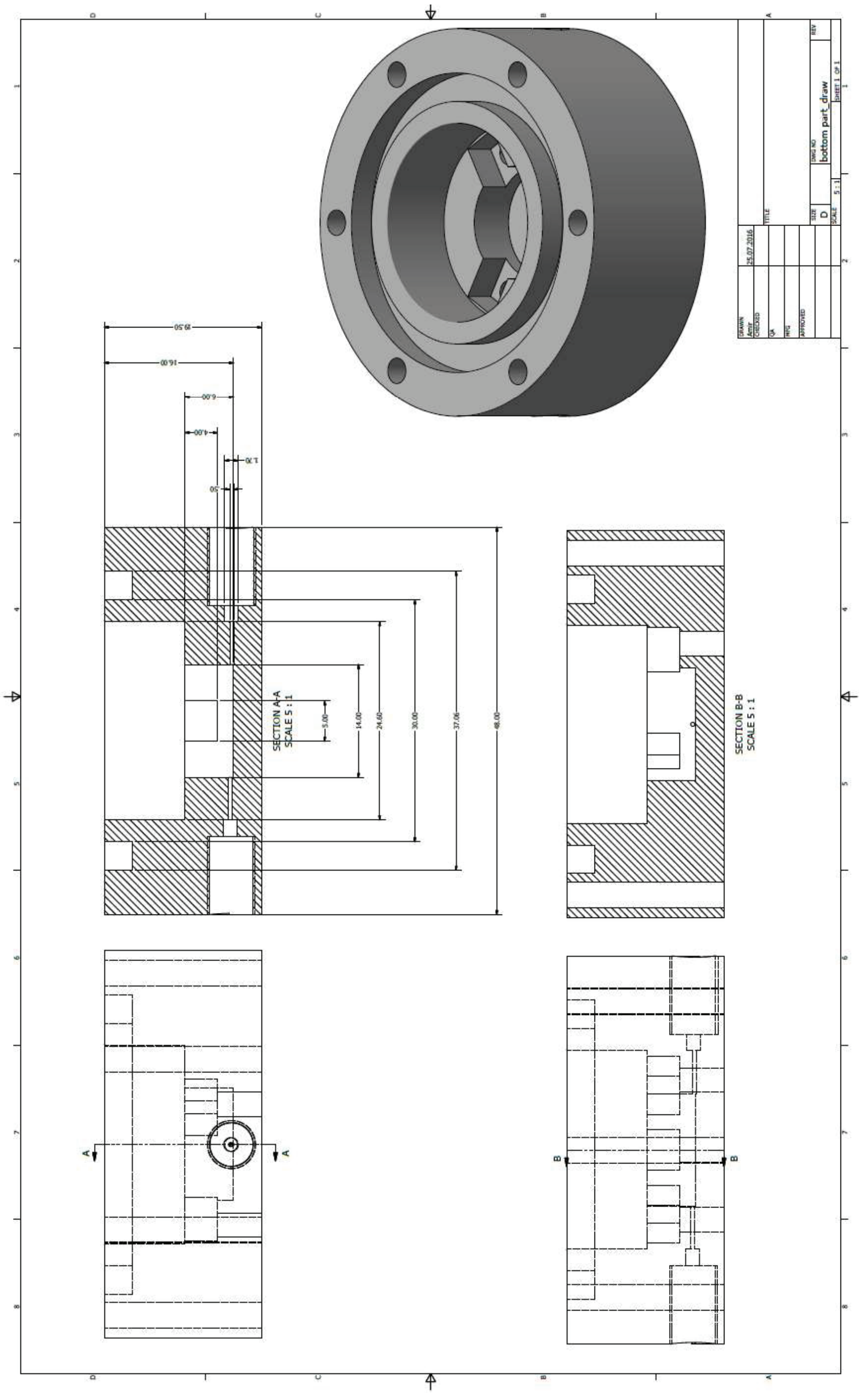

Figure 3-14: Top part of the second version of the DEMS cell, with all dimensions.

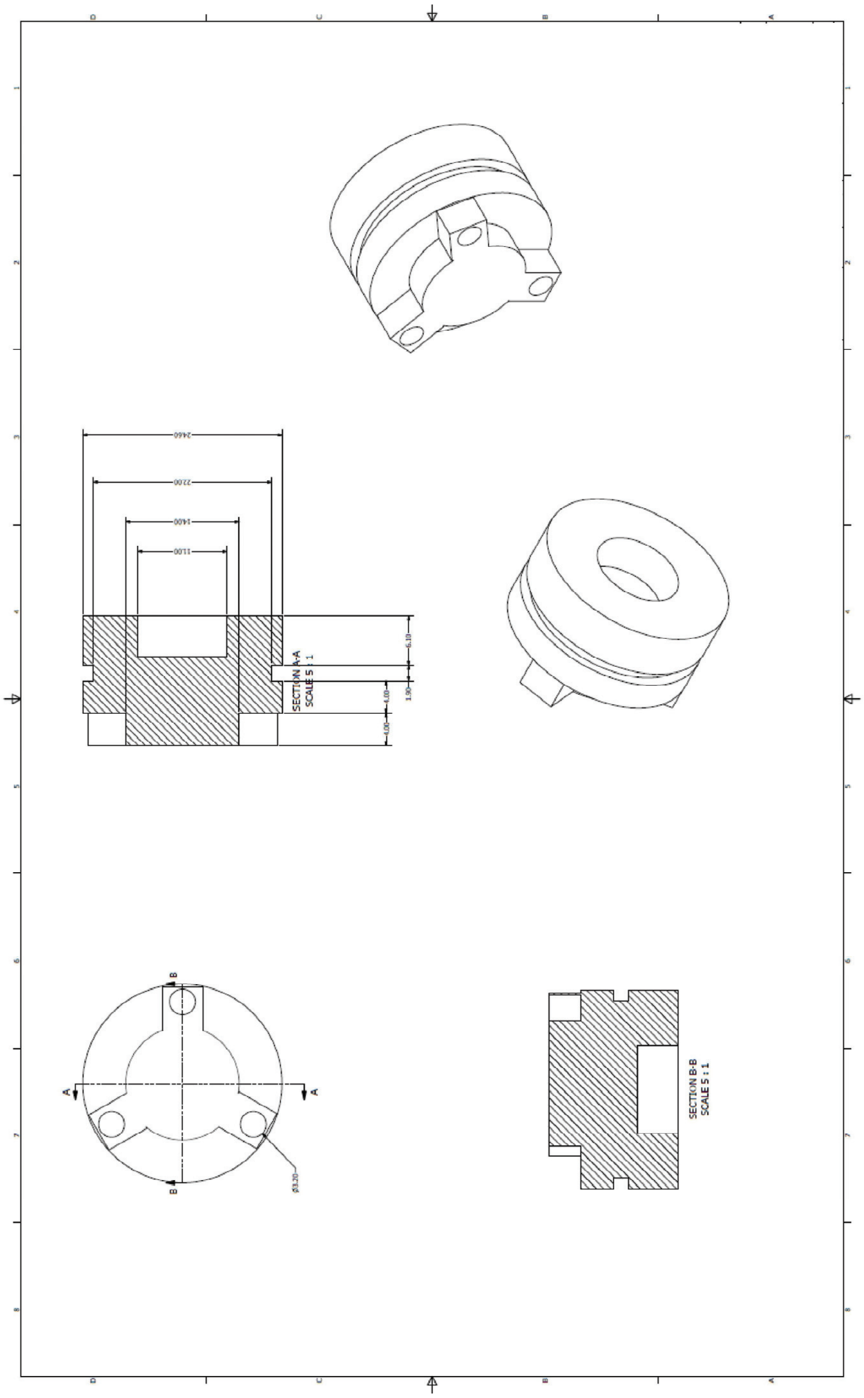

Figure 3-15: Middle part of the second version of the DEMS cell, with all dimensions.

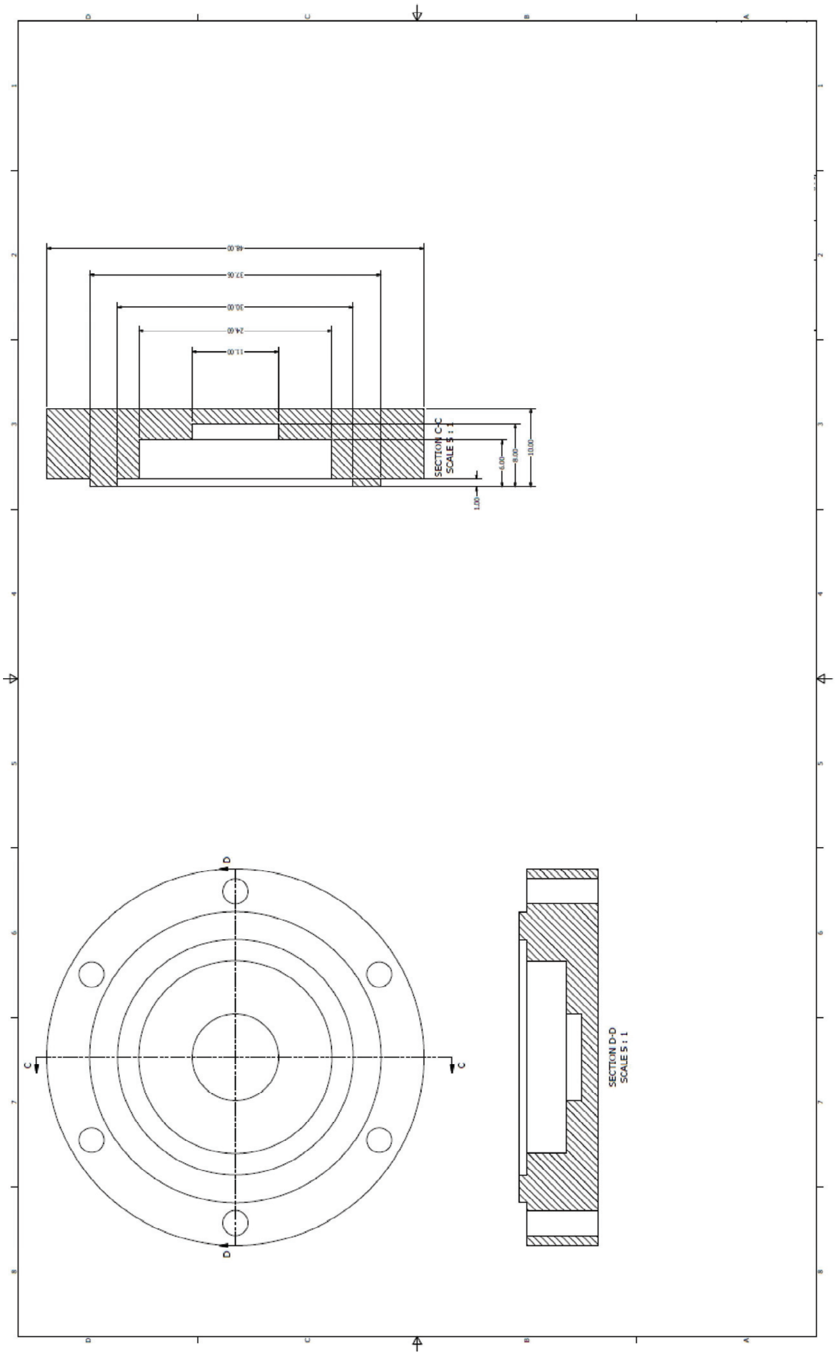

Figure 3-16: Bottom part of the second version of the DEMS cell, with all dimensions.

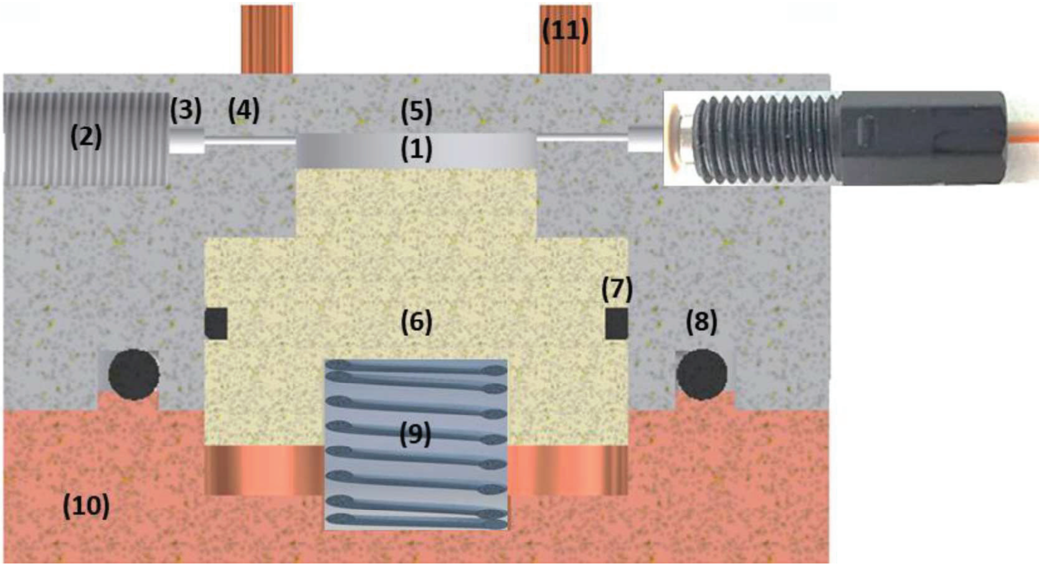

Figure 3-17: Schematic assembly of the second version of the DEMS cell: (1) Space to assemble the electrodes and separators; (2) Inlet and/or outlet channel to connect the tubes to the DEMS cell; (3) Extra space to fix the tubes; (4) Inlet and/or outlet channel for the carrier gas and produced species; (5) Top part of the cell; (6) Middle part of the cell; (7-8) O-rings; (9) Compression spring; (10) Bottom part of the cell; and (11) Current connector.

A schematic sketch of the cell can be found in Figure 3-17. The body of the cell, indicated with the numbers 5, 6, and 10 was fabricated using PEEK. Number 1 in this Figure corresponds to the space filled with PTFE membranes, as well as the working, counter, and reference electrodes. The 2 mm at the top of this space was filled with a PTFE membrane to homogenize the flow of carrier gas and prevent the electrolyte from entering the outlet channel. The number 2 indicates the connection between the DEMS cell and the tube of carrier gas. To connect the tube to the cell, 1/4-28 inch nuts were used. The sealing of the connection was achieved by using stainless steel bushing and PEEK ferrules. The tube was fixed inside the space; in the Figure it is illustrated with a number 3. The diameter of this space was slightly larger than the outer diameter of the tube, and was equal to 1.7 mm; the length of this area was 2 mm. To prevent a pressure drop in the carrier gas before it reached the inside of the cell, a cylindrical channel (indicated with a number 4) that was 5.3 mm in length was fabricated. The diameter of this channel was exactly as same as the inner diameter of the tube, 0.50 mm. After filling the cell with electrodes and separators, this area was sealed from the outside by the middle part of the cell.

To achieve a better sealing, an O-ring was placed around middle part, indicated with a number 7 in the schematic sketch. To guarantee a perfect sealing of the cell from the outside, another O-ring was added to the cell between the top and bottom parts. These two O-rings did not negatively affect each other, while the first O-ring tolerated a vertical force and the second O-ring was under a horizontal force. To create a constant pressure on the electrodes inside the cell, a spring was employed behind the middle part, indicated with a number 9. The current connectors (which could have been made either of titanium or glassy carbon, based on application) were positioned inside the cell on the perimeter of the circle, with a 120° difference between them. In total, there were three current connectors; one is indicated with a number 11. Using glassy carbon or titanium as the current connector made it possible to apply this cell at a high current voltage in both organic and aqueous solutions.

To validate the performance of the cell, the collection efficiency and the contact between the electrodes and current connectors had to be examined. In the first step, the collection efficiency of the cell was determined. To do this, an empty cell (filled only with PTFE paper) was connected to the argon line, and argon (as a carrier gas) was sent into the cell at flows ranging from 0.050 to 0.500 sccm. The flow of the argon gas was adjusted by the mass flow controller. Another mass flow controller was assembled for this setup after the outlet channel of the DEMS cell, in order to measure the output flow of the carrier gas. Figure 3-18 shows the results of this experiment.

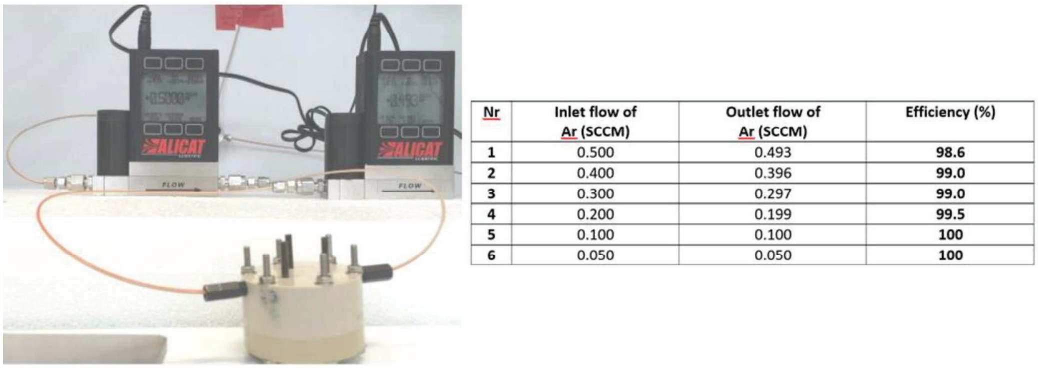

Nr	Inlet flow of Ar (SCCM)	Outlet flow of Ar (SCCM)	Efficiency (%)
1	0.500	0.493	**98.6**
2	0.400	0.396	**99.0**
3	0.300	0.297	**99.0**
4	0.200	0.199	**99.5**
5	0.100	0.100	**100**
6	0.050	0.050	**100**

Figure 3-18: Evaluation of the collection efficiency of the second version of the DEMS cell.

The collection efficiency of this cell was much better than that of the previous cell. This efficiency began at 98.6% for the high argon flow and increased up to 100% for the low argon flow. This is worth to notice that the collection efficiency for the last DEMS cell was 85%.

In the next step, the connection between the current connectors and electrodes needed to be tested. For this purpose, the high-frequency domain of the impedance spectra was studied. As has already been mentioned, the position of the current connectors was at the edge of the space in which the electrodes and separators were assembled. Therefore, the electrodes needed to be prepared in a circular shape, with an extra edge at the corner to connect to the current connectors. Due to the flow of argon inside the cell, the electrodes had to be fixed on top of the current connectors; otherwise, the connection would be lost during the measurements. Figure 3-19 schematically shows the positioning of the current connectors inside the cell.

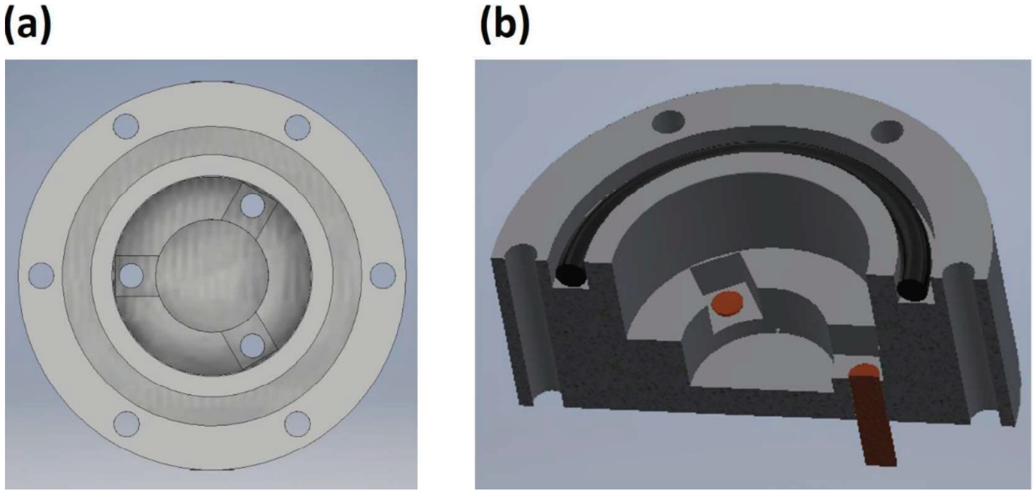

Figure 3-19: Schematic sketch of the top part of the cell: (a) Top view, and (b) Cross section of one part. The current connectors are indicated with a brown color in (b).

To fix the electrodes on the current connectors, certain modifications needed to be applied to the middle part of the cell. On the first attempt, the holes on this part were filled with a conductive material. The height of the conductive material was changed from 0.2 to 0.6 mm. Figure 3-20 shows this modification on the middle part of the cell.

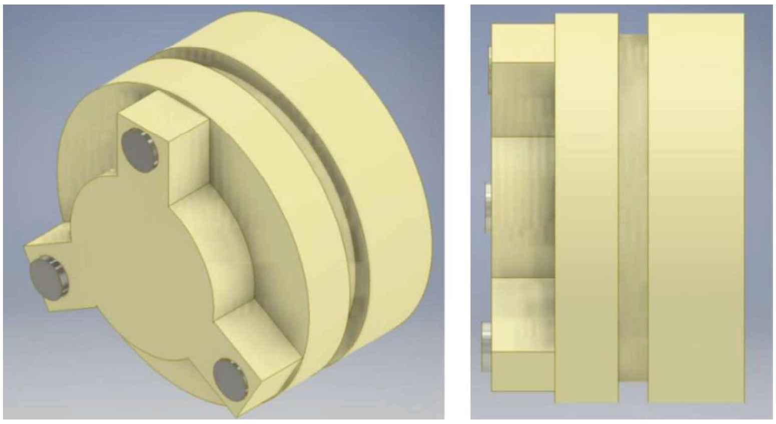

Figure 3-20: Filling the holes in the middle part of the cell with a different height of conductive material to improve the connection between the electrodes and current connectors.

In the next step, the impedance spectra of the working electrode were examined. To accomplish this, three different zinc foils were used: WE, RE, and CE, in 500 mM of $ZnSO_4$ as the electrolyte. The impedance spectra in the high-frequency domain are shown in Figure 3-21 for the different configurations.

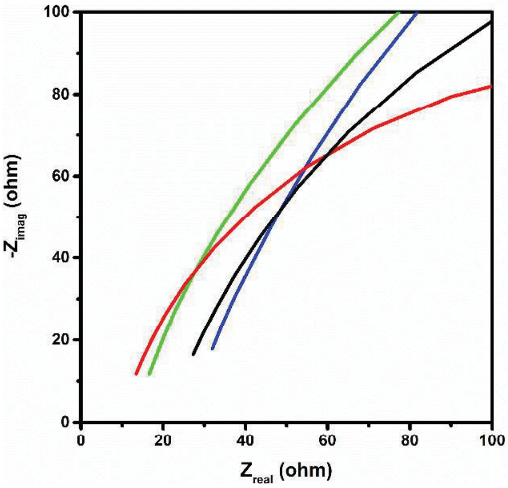

Figure 3-21: Impedance spectra at a high-frequency domain with different cell configurations. Black line: a normal configuration in which the WE, RE, and CE were located inside the cell and from top to bottom, respectively. Red line: inverse configuration in which the CE, RE, and WE were located inside the cell and from top to bottom, respectively. Blue line: two-electrode configuration in which the WE was located on top and the CE and RE were short-circuited at the bottom of the cell. Green line: two-electrode inverse configuration in which the WE was located at the bottom and the CE and RE were short-circuited at the top of the cell.

Four different configurations of cell assembly were defined, and EIS measurements in the high-frequency domain were obtained. These configurations were as follows:

1- Normal configuration: in which the WE, RE, and CE were located inside the cell and from top to bottom, respectively; this is indicated with a black line on the graph.

2- Inverse configuration: in which the CE, RE, and WE were located inside the cell and from top to bottom, respectively; this is indicated with a red line on the graph.

3- Two-electrode configuration: in which the WE is located on top and the CE and RE were short-circuited at the bottom of the cell; this is indicated with a blue line on the graph.

4- Two-electrode inverse configuration: in which the WE is located at the bottom and the CE and RE were short-circuited at the top of the cell; this is indicated with a green line on the graph.

It was obvious from the EIS results that the impedance spectra crossed the x-axis, a real part of the impedance spectra, from 10 to 30 ohms. This 20-ohm difference between various configurations indicates that the connections between the electrodes and current connectors was not very good. Therefore, another modification was made to this part of the cell. In this modification, the holes on the middle part of the cell were filled with compression springs. This configuration properly affixed the electrodes to the current connector. Moreover, if the thickness of the electrodes changed, the length of the spring also varied. This feature can provide the possibility to use electrodes of different thicknesses. Figure 3-22 shows a schematic view of the middle part of the cell and the results of the EIS experiments in the high-frequency domain.

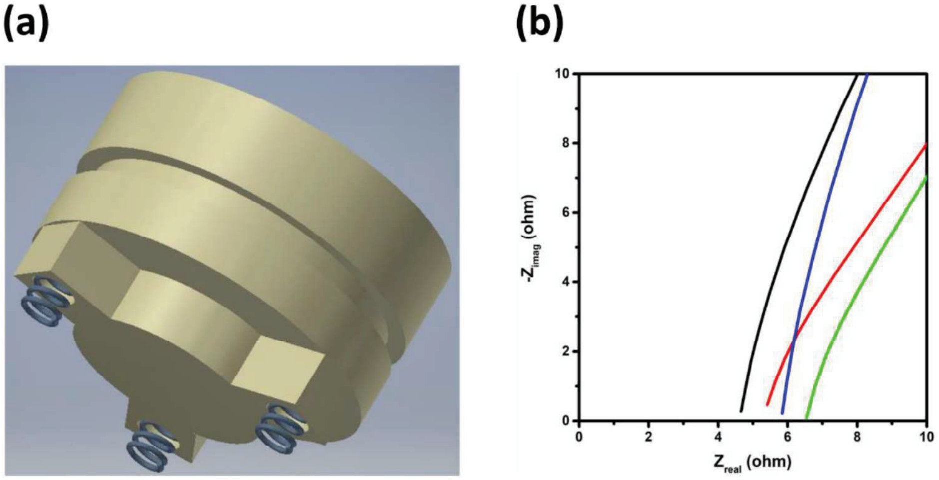

Figure 3-22: (a) Schematic view of the middle part of the cell after inserting a spring inside the holes; and (b) Impedance spectra in a high-frequency domain with different cell configurations. Black line: a normal configuration in which the WE, RE, and CE were located inside the cell and from top to bottom, respectively. Red line: inverse configuration in which the CE, RE, and WE were located inside the cell and from top to bottom, respectively. Blue line: two-electrode configuration in which the WE was located on top and the CE and RE were short-circuited at the bottom of the cell. Green line: two-electrode inverse configuration in which the WE was located at the bottom and the CE and RE were short-circuited at the top of the cell.

This configuration greatly enhanced the impedance spectra in the high-frequency domain. The magnitude of the electrolyte's resistance, which was measured in these different configurations, dropped from 20±10 ohms in the first design to 5.5±1 ohms in the second. This was a sign of good contact between the electrodes and current connectors. Therefore, for subsequent experiments small springs were implemented at the inside of the middle part of the cell. To prevent direct contact between the springs and current connectors, two layers of separator were applied.

The next part discusses applications of the DEMS method to the study of aqueous zinc-ion batteries, using both designed cells. To the best of knowledge, this is the first study of this technique to analyze electrochemical and side reactions in aqueous rechargeable batteries.

3.4. Application of the DEMS Method to the Study of Aqueous Zinc-Ion Batteries

To collect more energy from renewable sources, it is best to use a battery with a higher capacity of charge. One method for storing more charge capacity is the use of multivalent cations (e.g., Al^{3+}, Ni^{2+}, Mg^{2+}, Zn^{2+}, and Ca^{2+}) as intercalation species. Among the multivalent aqueous metal-ion batteries, zinc-ion batteries could be a useful choice for large-scale energy storage. In 2015, a new type of zinc-ion battery, based on copper hexacyanoferrate, was introduced [65]. In this type of battery, zinc was employed as a negative electrode, 20 mM of zinc sulfate was used as the electrolyte, and copper hexacyanoferrate (CuHCF) served as the positive electrode. The average discharge voltage of this type of battery was 1.73 V, which was one of the highest values from aqueous metal-ion batteries at the time of publication. The XRD patterns after cycling showed that hydrogen evolution can occur in this type of battery. The authors believed that hydrogen evolution began in the first cycle and stopped before the fifth. To gain a better understanding of the hydrogen evolution that occurs in this type of battery, the same materials and electrolyte were introduced to the first version of the DEMS cell (see Figure 3-7) and an *in-operando* hydrogen evolution measurement was performed.

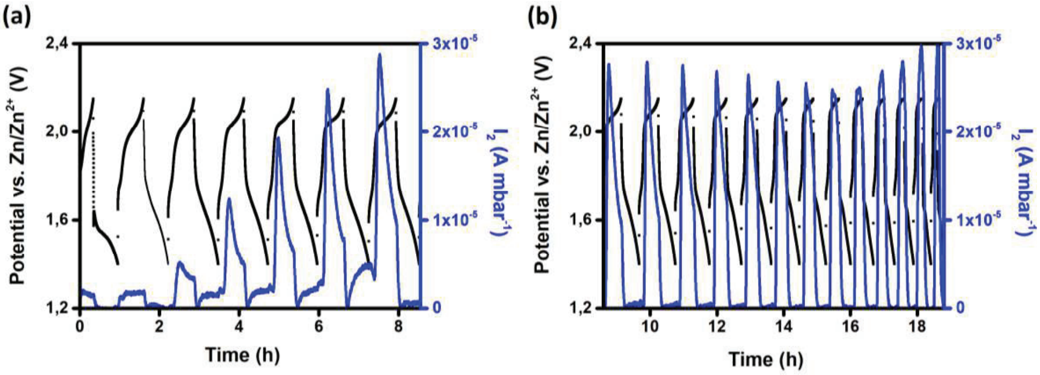

Figure 3-23: Hydrogen evolution during cycling of CuHCF vs. zinc in 20 mM of $ZnSO_4$ under a constant current equal to 2C, in the range of 1.4 to 2.2 V: (a) The first seven cycles, and (b) From cycle 7 to 20. In both graphs, the black lines indicate the potential changes during GCPL measurement, and the blue lines show the variations in hydrogen evolution.

As a cathode material, CuHCF was prepared as described in [65]. CuHCF slurry was made from a mixture of CuHCF, binder (PVDF in NMP), and C65. The final ratio of materials in the slurry was 80:10:10 wt%, respectively. The slurry of the zinc powder was employed as a negative electrode, and 20 mM of zinc sulfate was used as the electrolyte. In total, four separators were employed between the two electrodes. They were completely wetted with 200 µL of the electrolyte. The weights of the active material in the positive and negative electrodes were 8 and 14 mg, respectively, and the pH of the electrolyte was equal to 6. A GCPL was performed to cycle the battery in the range of 1.4 to 2.2 V, at a current rate of 2C. Argon gas acted as the carrier gas, bringing the volatile and evolved compounds from the cell to the mass spectrometer. Before starting the measurement, the cell was purged with argon for one hour to remove any residual air. The pressure of the vacuum chamber was set to 7.6E-7 mbar.

The results of this experiment are shown in Figure 3-23; hydrogen evolution is reported with a blue line and the potential variation during the GCPL technique is illustrated with a black line. From Figure 3-23(a), it can be seen that contrary to the previous hypothesis that was based on a postmortem analysis [65], hydrogen evolution is observed during all cycles. The amount of hydrogen evolution increased up to the seventh cycle and decreased gradually in the following cycles (see Figure 3-23(b)). Moreover, degradation of the system is observable in the aforementioned graph. The time of the oxidation and reduction processes decreased with an increase in the number of cycles. This means that the material was degraded during cycling. If the areas under the hydrogen evolution curves were calculated, more useful information could be collected. Additionally, the time difference between the starting point of the CuHCF oxidation, which was also the starting point of the zinc reduction, and hydrogen evolution was an important parameter. This parameter is called Δt_H and is shown versus cycle number in Figure 3-24(b).

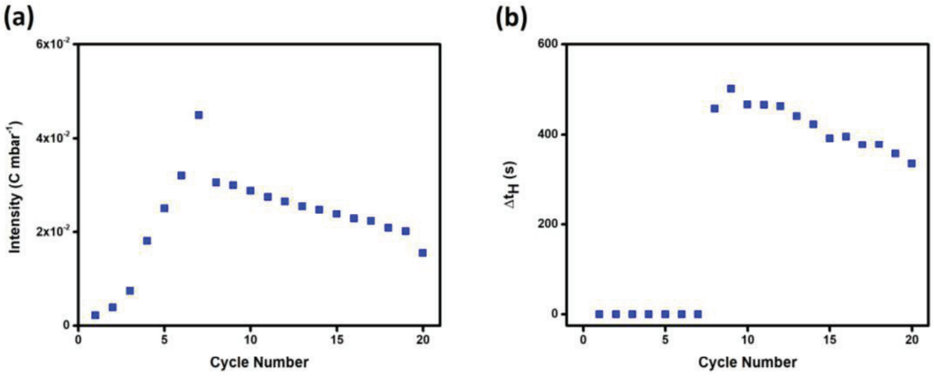

Figure 3-24: (a) The area under the hydrogen evolution peaks vs. the cycle number; (b) The time difference between the starting point of CuHCF oxidation and hydrogen evolution vs. the cycle number.

The magnitude of hydrogen evolution increased more than 10 times from the first cycle to the seventh, and then decreased moderately. This phenomenon can be explained by the fact that the surface of the negative electrode, which in this case was zinc, was thoroughly covered by zinc oxide or zinc hydroxide, up to the seventh cycle. Therefore, to further reduce this layer, an electrochemical reaction was required. This reduction led to a temporal shift in the starting point of the hydrogen evolution. In other words, the zinc, upon contact with the water molecules, formed a thin layer of ZnO or $Zn(OH)_2$ on the surface; this blocked further hydrogen evolution. When this layer was electrochemically reduced, the hydrogen evolution began again.

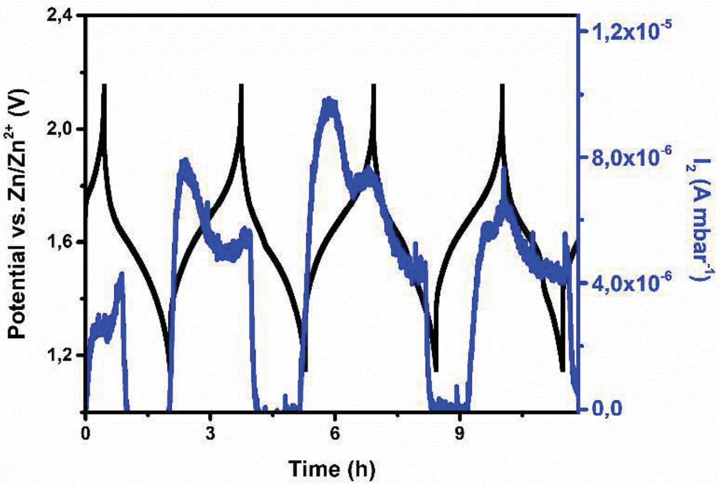

Figure 3-25: Hydrogen evolution during cycling of the CuHCF vs. zinc in 500 mM of $ZnSO_4$ under a constant current equal to 0.6C, in the range of 1.15 to 2.15 V. The black lines show the potential changes during GCPL and the blue lines indicate the variations in hydrogen evolution.

To prove the performance of the second version of the DEMS cell (which is schematically illustrated in Figure 3-17), a slightly modified version of the same experiment was carried out in an aqueous electrolyte. The first modification was related to the electrolyte's concentration. As is the case in practical applications, a diluted electrolyte could not be applied. For this experiment, the concentration of zinc sulfate was increased from 20 to 500 mM. Moreover, the current density was decreased from 2C to 0.6C. Finally, the weights of the electrodes, amount of electrolyte, and potential range were changed as follows:

1- The weight of the active material in the working electrode (CuHCF) was 14.4 mg.

2- The weight of the active material in the counter electrode (zinc) was 7.7 mg.

3- A solution of 500 mM of $ZnSO_4$ was employed as the electrolyte. Four separators were inserted between two electrodes and wetted with 200 µL of electrolyte.

4- The potential range was set to 1.15 to 2.15 V versus Zn/Zn^{2+}.

5- The pressure of the vacuum chamber was 5E-7 mbar.

The results of the gas evolution for the four cycles of this experiment are shown in Figure 3-25. As was expected, the hydrogen evolution began in the first cycle and continued in subsequent cycles. In addition, the time shift between the starting points of the CuHCF oxidation and hydrogen evolution at the zinc electrode was observed after the third cycle. Therefore, coverage of the zinc surface by zinc oxide or zinc hydroxide was completed after a smaller number of cycles than in the last experiment. As the current density, which was applied to the zinc electrode in both experiments, was almost the same, this phenomenon can be explained by the relation between the electrolyte's concentration and the rate of the reaction.

The rate of the reaction can be defined as follows:

$$r_i = k_i \cdot C_i \tag{3-4}$$

where r_i is the reaction rate, k_i is the rate constant, and C_i is the concentration of species i [125]. Moreover, the rate constant is proportional to the activation energy of the reaction, as follows (see [125]):

$$k_i = A \cdot \exp({}^{-E_A}/_{RT}) \tag{3-5}$$

where A is the frequency factor, E_A is the activation energy of the reaction, R is the universal gas constant, and T is the temperature. From Eqs. 3-4 and 3-5, the rate of reaction (r) can be written as follows:

$$r_i = C_i \cdot A \cdot \exp({}^{-E_A}/_{RT}) \tag{3-6}$$

Additionally, the activation energy can be defined as:

$$E_A = E_A^0 + \alpha \Delta E \tag{3-7}$$

where α is the transfer coefficient. Therefore:

$$r_i = C_i \cdot A \exp({}^{-E_A^0}/_{RT}) \cdot \exp({}^{-\alpha \Delta E}/_{RT}) \tag{3-8}$$

In Eq. 3-8, $A \exp({}^{-E_A^0}/_{RT})$ is constant and can be considered as B. Thus, Eq. 3-8 can be simplified as:

$$r_i = C_i \cdot B \cdot \exp({}^{-\alpha \Delta E}/_{RT}) \tag{3-9}$$

In addition, the proportionality of E to the concentration can be extracted from the Nernst equation, as follows:

$$E = E^0 + RT \cdot \ln\frac{[Ox]}{[Red]} \tag{3-10}$$

Here, the zinc electrodeposition reaction is considered:

$$Zn^{2+} + 2e^- \rightarrow Zn \tag{3-11}$$

Therefore, the Nernst equation can be written as:

$$E = E^0 + RT \cdot \ln[Ox] \tag{3-12}$$

and

$$\Delta E/_{RT} = \ln[Ox] \tag{3-13}$$

To calculate the ratio of zinc electrodeposition in two different concentrations of zinc sulfate solution, C_1 and C_2, Eq. 3-13 can be substituted into Eq. 3-9, as follows:

$$\frac{r_{C_2}}{r_{C_1}} = \frac{C_2 \cdot \exp\left[-\alpha \cdot \ln(C_2)\right]}{C_1 \cdot \exp\left[-\alpha' \cdot \ln(C_1)\right]} \tag{3-14}$$

It has been shown in the Butler-Volmer model of electrode kinetics [125] that the transfer coefficient is independent from the concentration. Therefore:

$$\frac{r_{C_2}}{r_{C_1}} = \left(\frac{C_2}{C_1}\right)^{1-\alpha} \tag{3-15}$$

It is known that the value of α can range from zero to unity, therefore the magnitude $\frac{r_{C_2}}{r_{C_1}}$ can vary between 1 and $\left(\frac{C_2}{C_1}\right)$. In the case of 20 and 500 mM of zinc sulfate, this ratio can be written as follows:

$$1 < \frac{r_{zinc\ deposition,500\ mM}}{r_{zinc\ deposition,20\ mM}} < 25 \tag{3-16}$$

Therefore, the rate of zinc electrodeposition is increased with an increase in the concentration of zinc sulfate in an aqueous solution.

In the case of hydrogen evolution, increasing the concentration of zinc sulfate in the solution has no effect on the concentration of hydrons. This means that C_{H+} is constant in both 20 and 500 mM of zinc sulfate solution. Thus, Eq. 3-15 can be written for hydrogen evolution, as follows:

$$\frac{r_{C_2}}{r_{C_1}} = \left(\frac{C'_2}{C'_1}\right)^{-\alpha} \tag{3-17}$$

It should be noted that C'_2 and C'_1 in Eq. 3-17 are the concentrations of zinc sulfate in the solutions. This can be concluded from Eqs. 3-9 and 3-13, which show the dependency of ΔE on the concentration of zinc in the solution. Therefore, the ratio of hydrogen evolution between 20 and 500 mM of zinc sulfate can vary between 0.04 and 1, as indicated in Eq. 3-18:

$$0.04 < \frac{r_{hydrogen\ evolution,500\ mM}}{r_{hydrogen\ evolution,20\ mM}} < 1 \tag{3-18}$$

This shows a decrement in hydrogen evolution when the concentration of zinc sulfate is increased from 20 to 500 mM. In other words, the aforementioned calculations confirm a shift towards the anodic equilibrium potential of zinc, when the concentration is increased from 20 to 500 mM. This is also shown by less-intense hydrogen evolution at higher concentrations of the electrolyte, as compared to the diluted electrolyte. Therefore, increasing the electrolyte concentration served to reduce hydrogen evolution in this type of battery. This experiment shows the usefulness of this cell in studying gas evolution in aqueous metal-ion batteries.

In the next part, the source of gas evolution in the cell was investigated. As the cell was applied to configurations with two and three electrodes, it was very important to determine if the detected gas was produced by one or both of the electrodes. To perform such an experiment, zinc electrodes were used as the working, counter, and reference electrodes inside the cell. Zinc slurry, which was painted on a carbon cloth, was used as the working and reference electrode, and zinc foil was employed as the counter electrode. This experiment was also carried out in 500 mM of $ZnSO_4$ as the electrolyte, with a total volume of 200 µL on the separators. The experiment began with two hours of reducing up to half of the theoretical capacity of the working electrode, accompanied by oxidation up to 0.3 V vs. Zn/Zn^{2+}. After four cycles, the oxidation limitation was reduced to 0.2 V vs. Zn/Zn^{2+}.

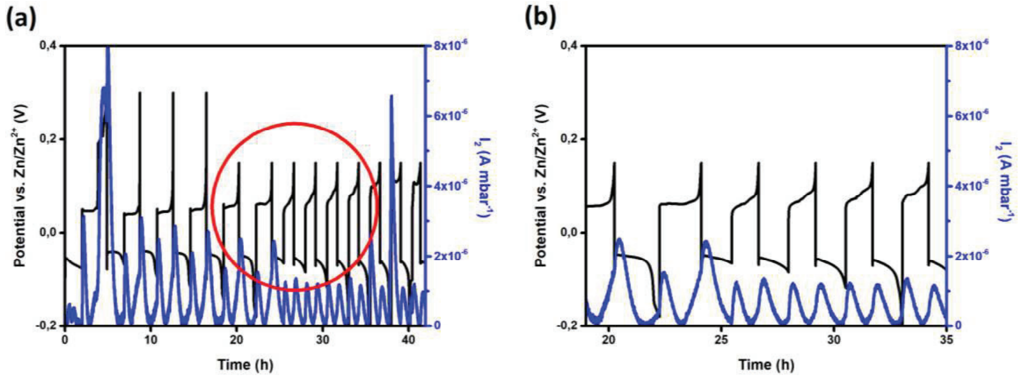

Figure 3-26: (a) Hydrogen evolution in a three-electrode cell. The working and reference electrodes were prepared with zinc slurry. Zinc foil was employed as a counter electrode; (b) Enlargement of a part of (a), for better resolution.

From Figure 3-26, it can be seen that hydrogen evolution was detected during the reduction and oxidation of the working electrode. As we discussed above, hydrogen evolution occurred during the reduction of the working electrode. The reason there was hydrogen evolution during the oxidation of the working electrode is the reduction of the counter electrode which produced hydrogen molecules. These molecules were carried by the argon gas to the mass spectrometer and then detected there. Therefore, it must be stressed that this DEMS cell can show gas evolution in the entire system, and thus is not suitable for studying gas evolution in one individual electrode.

Until now and in this investigation, all DEMS measurements in aqueous zinc-ion batteries were accomplished with a two-electrode cell configuration. To achieve a better understanding of the electrochemical behavior of each electrode, it is worthwhile to use a reference electrode in the system. As has already been discussed, the reference electrode in this electrochemical cell must have a flat plateau when it is at half-charged capacity. Moreover, to gather more accurate results, the reference electrode should contain the same intercalation ion as the working electrode, which in this case was zinc ions. Zinc hexacyanoferrate (ZnHCF) fulfilled all of these requirements, since it contains zinc in its structure and shows a flat plateau near to 1.96 V versus Zn^{2+}/Zn at half of the oxidation step. Therefore, the possibility of using this material as a reference electrode was investigated.

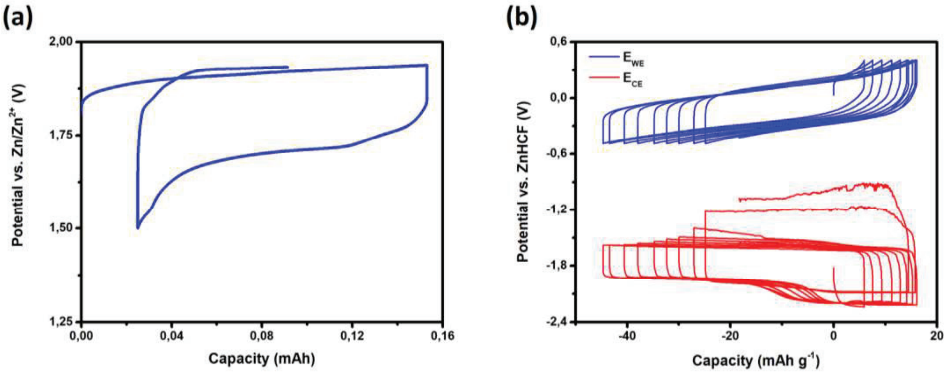

Figure 3-27: (a) Electrochemical preparation of ZnHCF as a reference electrode; (b) Cycling of the CuHCF as a working electrode vs. zinc as a counter electrode and ZnHCF as a reference electrode in 20 mM of $ZnSO_4$, to test the stability of the reference electrode upon cycling.

Figure 3-27(a) shows the first oxidation and reduction of the ZnHCF, which was synthesized as described in [87], accompanied by an oxidation step up to half capacity. This material has a flat plateau during zinc oxidation. Therefore, it can be used as a reference electrode in aqueous zinc-ion batteries. Figure 3-27(b) illustrates the first ten cycles of CuHCF vs. zinc in 20 mM of $ZnSO_4$, using ZnHCF as a reference electrode. Although the CuHCF cycling was very stable, the zinc counterpart in this cell showed an unstable electrochemical response after the seventh cycle. If these electrochemical characterization results are combined with the results of gas evolution during battery cycling, more information will be gathered that can be considered as a future work for this dissertation. Further development of the DEMS technique, accompanied by electrochemical characterization, will allow for more detailed study of the main and side electrochemical reactions during the cycling of aqueous batteries, upon which their final performance is highly dependent.

3.5. Conclusion

Chapter 3 presents an introduction to the DEMS technique. This chapter also provides a brief review of the applications for this method in characterizing rechargeable lithium-ion batteries in organic electrolytes. It was shown that this technique can effectively be employed to study the following phenomena in batteries:

1- Degradation mechanisms of electrolytes at low, moderate, and high potentials.

2- Effects of different parameters such as electrolyte additives, various solvents, salts, and temperatures on the degradation of electrolytes.

3- Effects of the surface roughness of electrodes on electrolyte decomposition.

4- Effects of electrode pretreatment and heat treatment on electrolyte decomposition.

5- Effects of impurities in the electrolyte, such as traces of water in organic electrolytes, on the intensity of gas evolution during battery cycling.

6- Stability windows of different mixtures of solutions serving as organic electrolytes.

The critical role of cell geometry in running *in-operando* DEMS measurements was also emphasized. Different electrochemical cells used for this purpose, designed by other researchers, were reported. A geometry of an electrochemical cell for running reliable and accurate EIS and DEMS measurements, as well as traditional electrochemical measurements such as cyclic voltammetry and galvanostatic cycling with potential limitation, was also introduced. Reliable DEMS measurements were performed by characterizing gas evolution during lithium-ion intercalation into a graphite electrode. The experimental results confirmed that this cell has a geometry appropriate for the simultaneous acquisition of impedance spectra and mass signals. The problems of the first version of the cell were determined and a modified DEMS cell was presented. To show the flexibility of both cells and possible application in aqueous rechargeable metal-ion batteries, hydrogen evolution in a zinc-ion battery based on Prussian blue derivatives was shown. The results of the experiments in 20 mM of zinc sulfate indicated that hydrogen evolution occurred during all cycles, and the amount of hydrogen evolution increased during the first cycles and decreased gradually upon continuous cycling. This phenomenon can be explained by the fact that zinc, upon contact with water, forms a thin layer of ZnO or $Zn(OH)_2$ on the surface, and this blocks further hydrogen evolution. When this layer is electrochemically reduced, the hydrogen evolution begins again. In addition, it was determined that increasing the concentration of an electrolyte can decrease the amount of hydrogen evolution. From these results, it is obvious that controlling hydrogen evolution is the key factor in enhancing the performance of aqueous zinc-ion batteries. Further developments of this DEMS technique will allow for more detailed studies of the main and side electrochemical reactions that occur during battery cycling, upon which the final performance is highly dependent.

The next chapters examine the effects of organic additives in electrolytes on zinc electrodeposition mechanisms. Furthermore, the application of layered double hydroxide (LDH) as a substrate for zinc electrodeposition is investigated. Finally, water-in-salt solution will be considered as a means of expanding the electrochemical stability window of the electrolyte and shifting the hydrogen evolution reaction to more negative potentials.

4. The Effect of Electrolyte Additives on the Performance of Negative Electrodes in Aqueous Metal-ion Batteries

The efficiency of zinc electrodeposition on negative electrodes is of fundamental importance for improving the long-term performance of aqueous zinc-ion batteries based on Prussian blue analogues (PBA). One approach to accomplish this goal is to introduce organic additives to the electrolyte. The application of organic additives in zinc bath solutions dates back to 1907 [126]. That study investigated the effect of a tiny amount of formaldehyde in solution on grain size of electrodeposited zinc layers. Since then, organic additives have frequently been used in zinc electrodeposition baths. They are usually applied for surface leveling or brightness purposes [127]. It has also been shown that the morphological aspects of electrodeposited layers of zinc in alkaline, acidic, and sulfate solutions can be varied by employing different kinds of additives [128–131]. In particular, organic additives play an important role in the modification of the surface roughness, grain size, and growth orientation of electrodeposited layers [82,83]. Organic additives can also increase cathodic overpotential, elevate surface polarization, and suppress the kinetics of zinc electrodeposition [84,85]. It has also been reported that co-deposition of organic additives onto the surface of an electrode may occur as a side reaction [127]. To prevent this reaction, the level of organic additive must be low.

Below, the electrodeposition mechanism of zinc under different applied current densities will be explained. Then, the limiting applied current density in which the electrodeposition mechanism is completely altered is determined. Finally, the effect of the presence of branched polyethyleneimine (BPEI) as an additive in a range of 10 to 300 ppm, in 500 mM of $ZnSO_4$ solution on the kinetics, cathodic overpotential, and efficiency of zinc electrodeposition, as well as the morphology of the electrodeposited layers, is presented.

4.1. The Zinc Electrodeposition Mechanism at Different Current Densities

It has already been illustrated that hydrogen evolution is inversely proportional to the electrodeposition efficiency of zinc in zinc sulfate solutions [132]. One of the significant parameters of the electrodeposition mechanism is the limiting current density. It has been demonstrated that at current densities higher than the limiting current density, water decomposition – and as a result hydrogen evolution – becomes the dominant reaction instead of zinc electrodeposition and/or dissolution [133]. Therefore, finding the limiting current density is of primary importance.

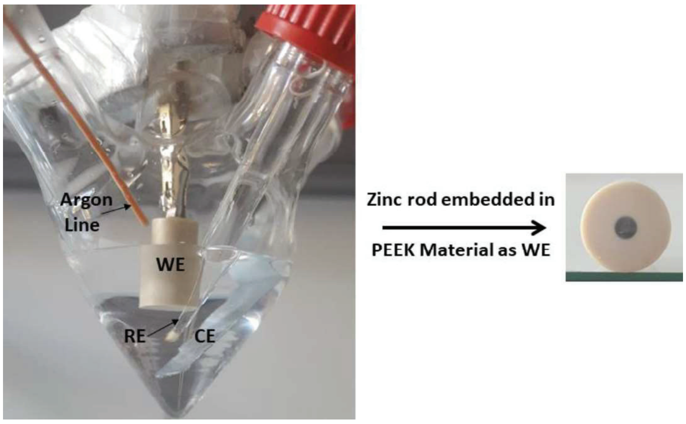

Figure 4-1: (left) Conical cell for studying the zinc electrodeposition mechanism; and (right) The working electrode for measurement.

To roughly estimate the limiting current density of any solution, the following formula can be applied:

$$i_L = \frac{nFC_BD}{\delta} \tag{4-1}$$

where i_L is the limiting current, n is the number of electrons transferred during the electrochemical reaction (this is equal to 2 in the case of zinc electrodeposition), F is the Faraday constant, C_B is the bulk concentration of the electrolyte, D is the diffusion coefficient of the zinc in the solution, and δ is the thickness of the Nernst layer. This last parameter usually varies from 0.001 cm for an agitated solution to 0.05 cm for an immobile solution. Based on calculation, the limiting current density should be approximately 13.56 mA cm^{-2}. The experiments began with this value and thereafter the current density was increased to find the effects of such changes on the potential response of the working electrode. The conical cell used to run the experiments and the working electrode are schematically represented in Figure 4-1.

To run the experiments, 500 mM of $ZnSO_4$ was used as the electrolyte. A zinc rod embedded in the PEEK was implemented as a working electrode. As a counter electrode, zinc foil was applied. All data were reported versus Ag/AgCl (3 M KCl) as the reference electrode. The diameter of the zinc rod was 2.5 mm; the PEEK acted as an insulator shield around the working electrode. In addition, the surface of the working electrode was polished with 1 µm polishing paper. Different cathodic current densities ranging from -13.56 mA cm^{-2} to -110 mA cm^{-2} were applied for 30 minutes, and the variations in potential were recorded. Figure 4-2 shows the potential variations versus time at different applied current densities.

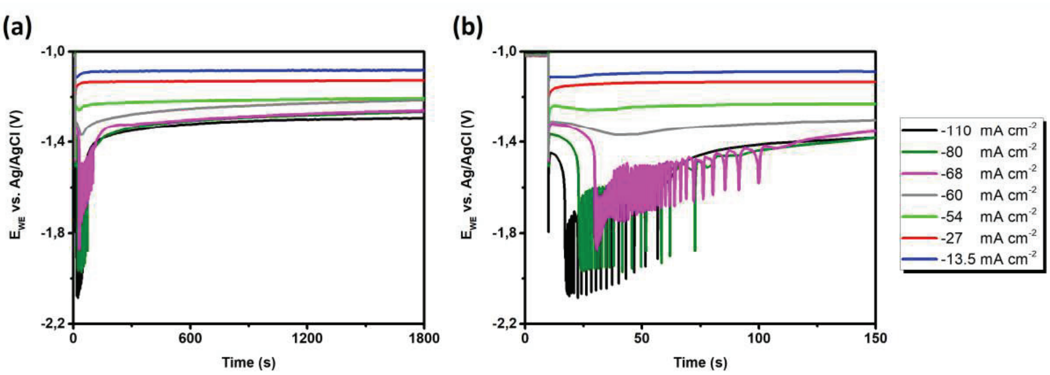

Figure 4-2: (a) Potential variations in the working electrode in 500 mM of $ZnSO_4$ under different applied current densities; and (b) Magnification of the first 150 seconds of the reactions under the various applied current densities.

The experiments were initiated by applying -13.5 mA cm^{-2} for 30 minutes. Subsequently, current densities of -27, -54, and -110 mA cm^{-2} were applied. As illustrated in Figure 4-2, the potential changes at the beginning of the experiment completely differed, from -54 mA cm^{-2} to -110 mA cm^{-2}. To find the precise limiting current density, current densities of -80, -60, and -68 mA cm^{-2} were applied to the working electrode, in that sequence. It should be noted that for each experiment, a new, perfectly-polished working electrode was used. The results show that at current densities ranging from -13.5 mA cm^{-2} to -60 mA cm^{-2}, the most prominent reaction on the surface of the working electrode was zinc electrodeposition. If the absolute value of the current density exceeded 60 mA cm^{-2}, frequent potential oscillations for a short period of time were observed. As the reaction continued, the interval times of the oscillations got larger. As this happened, the potential of the working electrode became more stable. This behavior can be explained by the fact that the limiting current density in this experimental condition was around -60 mA cm^{-2}. For current densities with absolute values less than the limiting current density, electrodeposition of zinc was the dominant reaction. Therefore, the working electrode experienced a potential drop at the starting point of the experiment, followed by a stable potential to the end.

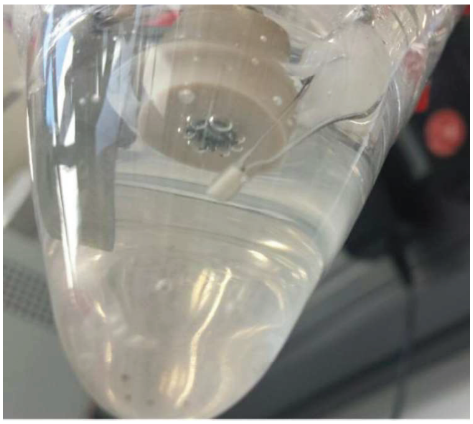

Figure 4-3: Hydrogen evolution at a high cathodic current density of -110 mA cm^{-2} on the surface of the zinc electrode.

For current densities with absolute values higher than the limiting current density, the reaction condition was completely different. In these experiments, decomposition of water on the surface of the working electrode occurred. Thus, hydrogen evolution was the controlling reaction for the first few seconds. This led an oscillating response in the electrode's potential. The reason of this response could be attributed to the gas formation on the surface of the electrode and bubbles detachment from the surface. As the rate of bubble formation decreased with the time, the interval between the oscillations increased. After that, the electrodeposition of zinc became the major reaction on the surface of the working electrode. Therefore, the time interval of the potential oscillations became larger and finally achieved stability. Figure 4-3 shows the hydrogen evolution on the surface of the electrode at a high current density.

To achieve a better understanding of the morphology of the working electrodes after running the experiments, SEM and 3D laser microscope images were taken from their surface. As is illustrated in Figure 4-4, increasing the absolute value of the applied current density from -13.5 mA cm^{-2} to -110 mA cm^{-2} had a significant effect on the thickness of the electrodeposited zinc at the edge of the sample. The rate of zinc electrodeposition at the edge of the working electrode was higher than at the center, due to the mass transport difference at these respective positions. This means that the zinc ions could approach the edge of the electrode more easily than the center. Furthermore, it was observed that at a low applied current density, the zinc layer could not thoroughly cover the surface of the electrode. This means that 30 minutes was not sufficient to form an electrodeposited layer on the surface. This was also confirmed by the SEM images.

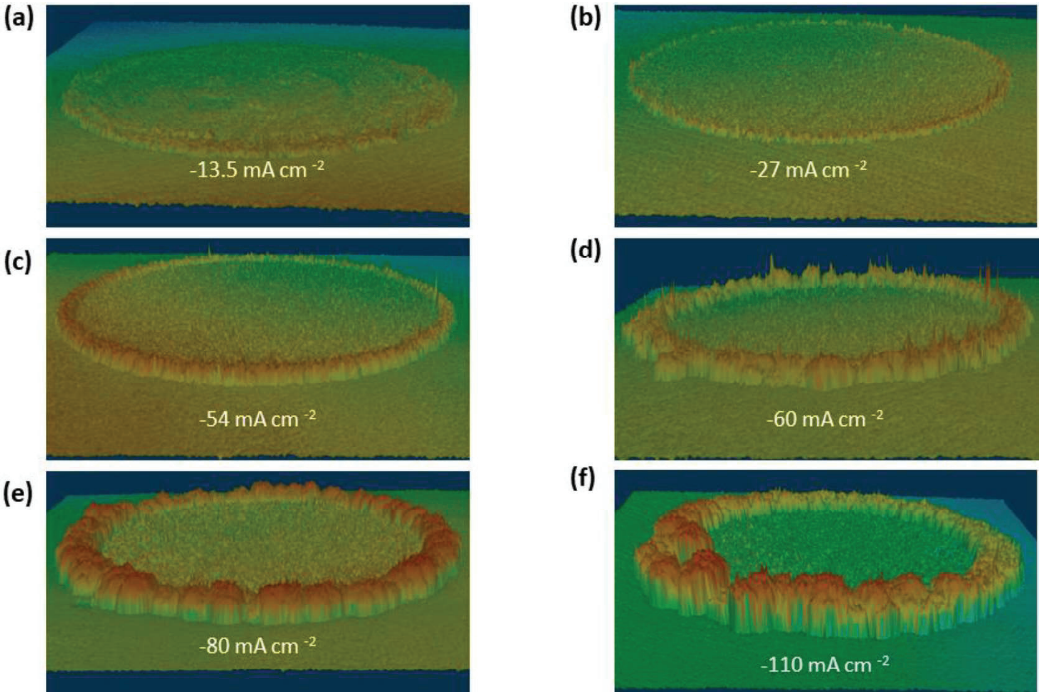

Figure 4-4: 3D laser microscope images of the working electrode after applying different current densities for 30 minutes in 500 mM of $ZnSO_4$. The applied current densities were equal to: (a) -13.5 mA cm^{-2}, (b) -27 mA cm^{-2}, (c) -54 mA cm^{-2}, (d) -60 mA cm^{-2}, (e) -80 mA cm^{-2}, and (f) -110 mA cm^{-2}.

Figure 4-5 shows the SEM images from the surface of the working electrode after applying -13.5 mA cm^{-2} for 30 minutes.

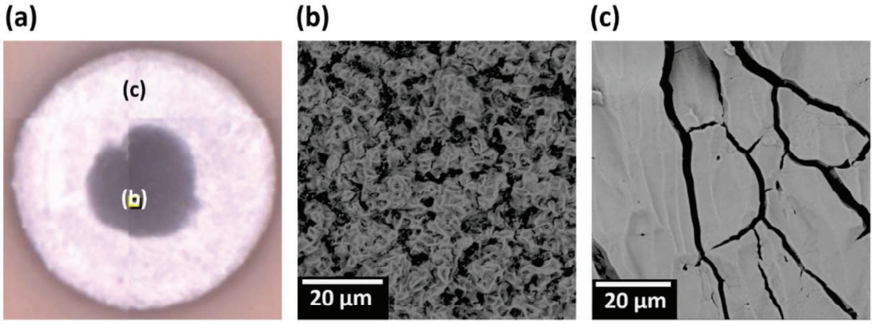

Figure 4-5: SEM images of the working electrode after 30 minutes of zinc electrodeposition under a -13.5 mA cm^{-2} applied current density in 500 mM of $ZnSO_4$. (a) Overall view of the working electrode under SEM; (b) Flower-like zinc growth in the middle of the working electrode; and (c) Growth of a thin layer of zinc at the edge of the sample.

As is illustrated in Figure 4-5(b), the number of zinc ions that reached the center of the working electrode was not adequate. Therefore, a flower-like electrodeposited layer was formed.

Contrary to what appeared in the center, sufficient zinc ions were deposited from the electrolyte to the edge of the working electrode. Thus, a thin layer of electrodeposited zinc was developed in this area, as is presented in Figure 4-5(c).

When the absolute value of applied current density was increased to 27 mA cm^{-2}, the mechanism of zinc growth changed, as shown in Figure 4-6. First, the surface of the working electrode was completely covered by an electrodeposited zinc layer.

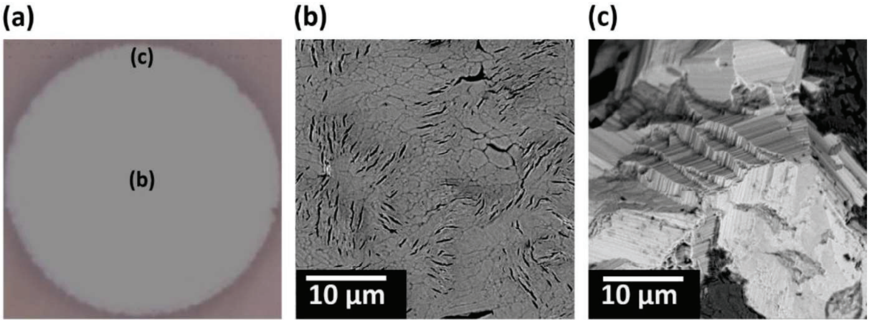

Figure 4-6: SEM images of the working electrode after 30 minutes of zinc electrodeposition under a -27 mA cm^{-2} applied current density in 500 mM of $ZnSO_4$. (a) Overall view of the working electrode under the SEM microscope; (b) Growth of a thin layer of zinc in the middle of the working electrode; and (c) Partial texture growth at the edge of the sample.

Second, the growth mechanism was different in response to the low applied current density. While a thin layer of electrodeposited zinc was formed in the middle of the working electrode, stepwise textured growth was observed at the edge of the working electrode. This mechanism was not dominant at the edge of the sample, but at some points was detected.

When the absolute value of the applied current density was raised up to 54 mA cm^{-2}, the predominant growth mechanism on the edge of the working electrode became preferential hexagonal growth. At this current density, some preferential hexagonal growth also appeared in the center of the working electrode, but it could not be considered the main mechanism in this area. Figure 4-7 displays the SEM images of the surface of the working electrode after 30 minutes of applying -54 mA cm^{-2} during zinc electrodeposition.

When the absolute value of the applied current density exceeded 60 mA cm^{-2}, the preferential hexagonal growth became the dominant growth mechanism on the surface. The growth mechanism on the surface of the working electrode at different applied current densities, from -60 mA cm^{-2} to -110 mA cm^{-2}, is presented in Figure 4-8.

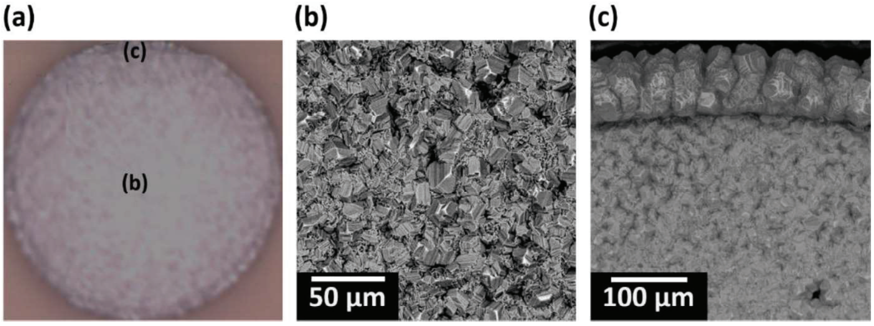

Figure 4-7: SEM images of the working electrode after 30 minutes of zinc electrodeposition under a -54 mA cm^{-2} applied current density in 500 mM of $ZnSO_4$. (a) Overall view of the working electrode under the SEM microscope; (b) Partial preferential hexagonal growth in the middle of the working electrode; and (c) Partial preferential hexagonal growth in the middle and on the edge of the sample.

At -60 mA cm^{-2} (see Figure 4-8(a)), which was the limiting current density, the system tended to minimize the surface energy of the electrodeposited layer. This meant that the growth of low surface energy planes was preferred with respect to the growth of high surface energy planes, and growth of the large hexagonal grains became the principle growth mechanism on the surface of the working electrode. Increasing the applied current density increased the number of ions reached the surface and decreased the size of the particles. At a high current density of -110 mA cm^{-2}, the mechanism was totally altered, and laminated hexagonal platelets were formed. Moreover, the size of the grains was almost one-third of the limiting current density.

To conclude, increasing the applied current density changed the growth mechanism from flower-like to preferential hexagonal growth. Moreover, if the absolute value of the applied current density exceeded the limiting current density of 60 mA cm^{-2}, the decomposition of water and hydrogen evolution became the predominant reactions during the first few seconds of the experiments; this resulted in an oscillation in the potential response of the working electrode within this period of time. Furthermore, the size of the hexagonal grains was decreased by increasing the applied current density.

In the next section, the effect of an organic additive, branched polyethyleneimine (BPEI), on zinc electrodeposition in 500 mM of $ZnSO_4$ will be characterized both electrochemically and morphologically.

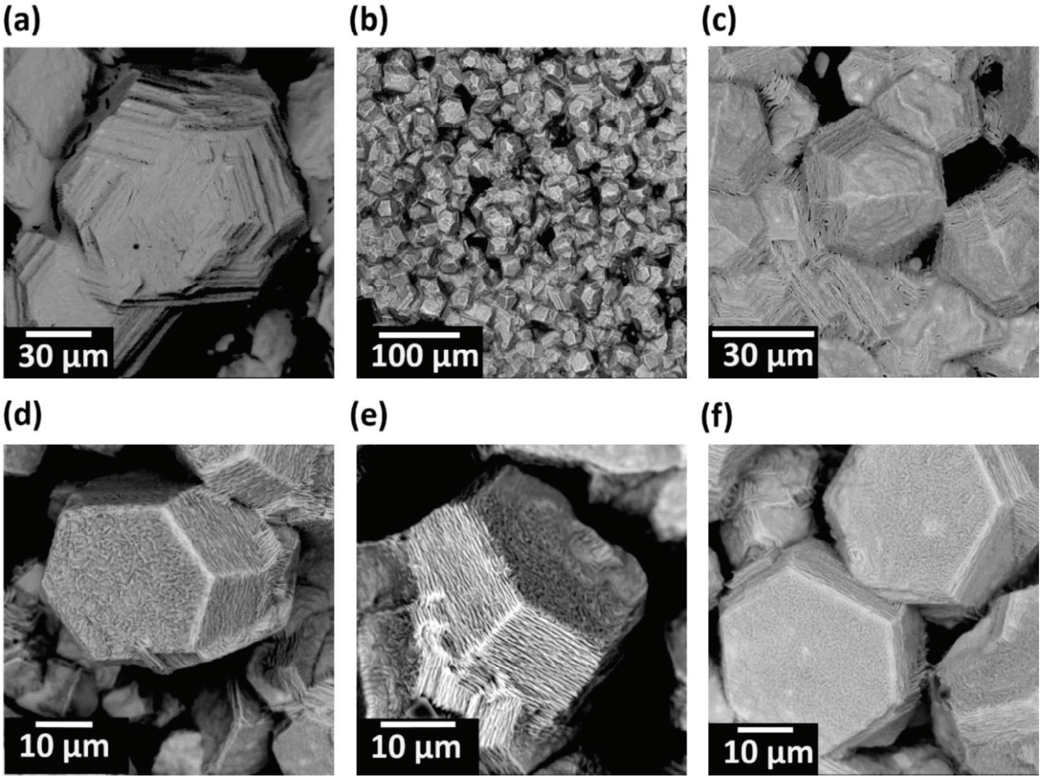

Figure 4-8: SEM images of the working electrode after 30 minutes of zinc electrodeposition in 500 mM of $ZnSO_4$ (a) -60 mA cm^{-2}, (b,c) -80 mA cm^{-2}, and (d-f) -110 mA cm^{-2}. Preferential hexagonal growth was the dominant growth mechanism on the surface of the working electrode.

4.2. The Effects of Branched Polyethyleneimine as an Electrolyte Additive on the Zinc Electrodeposition Mechanism at Different Current Densities

Electrolyte additives play a significant role in the zinc electrodeposition mechanism in zinc sulfate baths. Although they can change the surface morphology and kinetics of reaction and prevent hydrogen evolution, they may also codeposit on the surface of the working electrode, which is undesirable. Therefore, the concentration of the additive in an electrolyte should be minimized to inhibit its codeposition. In this study, branched polyethyleneimine (BPEI) was employed as an additive in 500 mM of $ZnSO_4$.

Polyethyleneimines (PEIs) are polymeric compounds composed of repeating units of amine groups and two aliphatic carbons. They are classified into two general categories: linear PEIs (LPEIs) and branched PEIs (BPEIs). A branched PEI, BPEI, may contain all types of primary, secondary, and tertiary amino groups and it is liquid at room temperature, irrespective of the molecular weight. An LPEI contains only primary and secondary amino groups, and it is solid at room temperature. The melting point of an LPEI is roughly 75°C [134]. In this research, a BPEI with a molecular weight of 800 g mol^{-1} was employed as an additive. Thereafter, the effect of this additive on the zinc electrodeposition mechanism was investigated.

One of the most important parameters when employing a battery for grid-scale energy storage is the current rate. In this case, the current rate is directly proportional to the kinetics of the zinc electrodeposition on the negative electrode. It has already been observed that additives can reduce the kinetics of electrochemical reactions on the surface of a working electrode [84,85]. To examine the effects of a BPEI on the electrodeposition of zinc in 500 mM of $ZnSO_4$, a 200 mV cathodic overpotential was applied for 30 minutes to a working electrode in electrolytes containing different concentrations of the additive, and the variations in current were recorded. Figure 4-9 illustrates the results of these experiments.

In Figure 4-9, the gray line indicates the highest concentration of the additive inside the electrolyte, which was 1,000 ppm BPEI; the black line shows the results of the experiment without using the additive. The concentration of the additive was varied from 300 ppm to 100 ppm, and eventually to 30 ppm (the red line, green line, and blue line, respectively). It can be concluded from this plot that the higher the concentration of additive, the lower the electrodeposition kinetics. In other words, increasing the concentration of additive leads to a lowering of the kinetics of the zinc electrodeposition. Since the kinetic of the electrodeposition affect the current rate of the battery, the concentration of the additive should be optimized so that its influence on the kinetics of the zinc electrodeposition reaction is minimized.

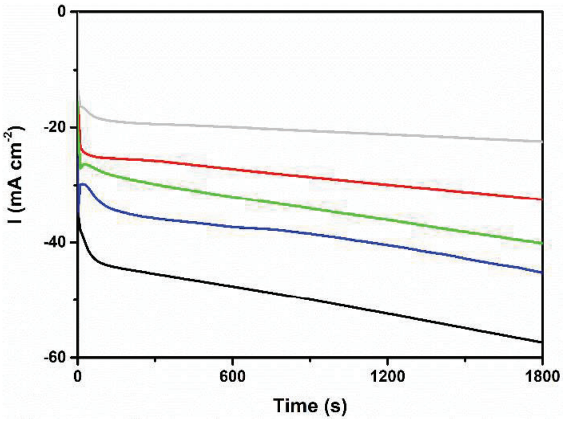

Figure 4-9: Current response of working electrode during 30 minutes of zinc electrodeposition under 200 mV of cathodic overpotential in 500 mM of $ZnSO_4$ with different additive concentrations. Black line: no additive, blue line: 30 ppm BPEI, green line: 100 ppm BPEI, red line: 300 ppm BPEI, gray line: 1,000 ppm PEI.

To study the effects of the additive on the zinc electrodeposition mechanism, three different current densities, namely -13.5 mA cm^{-2}, -60 mA cm^{-2}, and -110 mA cm^{-2} were identified as the low current, limiting current, and high current densities, respectively. Different concentrations of BPEI were added to the electrolyte, which was 500 mM of $ZnSO_4$ for all experiments. Zinc was electrodeposited on the surface of the working electrode for 30 minutes under different applied currents. Below, the effects of BPEI on the zinc electrodeposition at each applied current density are explained. Based on the above mentioned results, the solution containing 1,000 ppm BPEI was no longer studied; the electrolytes containing 10 ppm BPEI, 30 ppm BPEI, and 300 ppm BPEI are discussed below.

4.2.1. Low Current Density: -13.5 mA cm^{-2}

The first experiment studied the effects of different concentrations of additive in the electrolyte at a low applied current density. Figure 4-10(a) shows the potential change in the working electrode versus time for electrolytes containing 500 mM of $ZnSO_4$ and different concentrations of additives under an applied current density of -13.5 mA cm^{-2}. It can be determined from this Figure that increasing the concentration of BPEI in the electrolyte leads to a higher overpotential under a constant current.

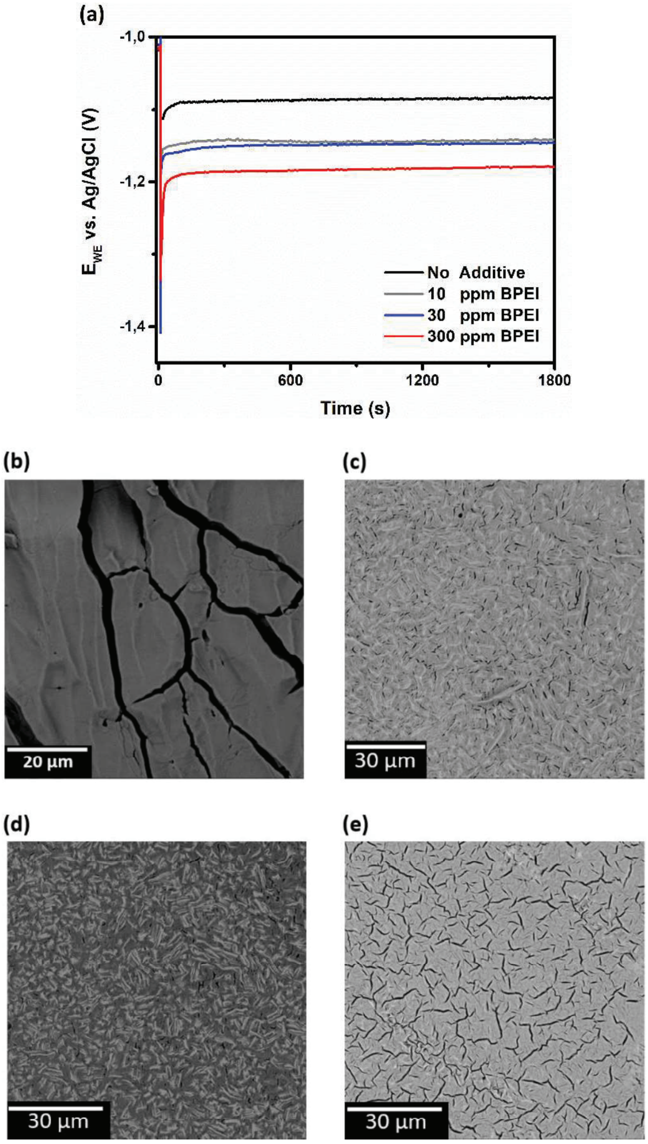

Figure 4-10: (a) Potential plot of the working electrode under an applied current density of -13.5 mA cm^{-2} in 500 mM of ZnSO$_4$ containing different concentrations of additive; (b-e) SEM images of the surface of the working electrode after finishing experiments in the electrolyte without an additive, 10 ppm, 30 ppm, and 300 ppm of BPEI, respectively.

The induced overpotential for 10 ppm and 30 ppm BPEI was almost the same at the end of the experiment. It was 60 mV more than the overpotential of the electrolyte without additive. This magnitude was 100 mV when 300 ppm BPEI was added to the electrolyte. This cathodic overpotential induced polarization on the surface of the working electrode and modulated current distribution to be more homogenous. This phenomena can be explained by Butler-Volmer equation [125]. Adsorption of the BPEI on the surface of the electrolyte decreased the surface area for zinc electrodeposition. Therefore, increasing the concentration of BPEI led to higher level of adsorption of this additive on the surface of the working electrode and less surface area for zinc electrodeposition. This decreased the exchange current density for zinc electrodeposition. To compensate this effect, the cathodic overpotential increased. As a result, the current distribution modulated to be more homogeneous and lower kinetic of the reaction was obtained.

4.2.2. Limiting Current Density: -60 mA cm^{-2}

As has already been discussed, increasing the applied current density to the limiting current density changes the growth mechanism. When there was no additive in the electrolyte, the system tended to minimize the energy by hindering the zinc growth on high energy surfaces. Thus, preferential growth began to develop all over the sample. This type of growth led to the formation of large hexagonal grains. Adding different concentrations of the additive caused the growth mechanism to completely change. As is clear from Figure 4-11(b-e), there was no evidence of preferential hexagonal plates, when different concentration of BPEI was added to the electrolyte. Therefore, adding BPEI drove the zinc ions to electrodeposit randomly on the surface of the substrate.

From Figure 4-11(a), it can be determined that the cathodic overpotential increased with increase in the applied current densities. In the other words, in the case of low current density, the cathodic overpotential is increased 60 mV and 100 mV for 30 ppm and 300 ppm of BPEI, respectively, as compared to the experiment without an additive in the electrolyte. These magnitudes were 70 mV and 300 mV, respectively, after applying a limiting current density.

Another important fact was related to the oscillation of the potential during the experiment when the concentration of the additive was 300 ppm in the electrolyte. To better understand this potential curve, 3D images of the surface of the working electrodes were constructed via a 3D laser microscope. The images are illustrated in Figure 4-12. Although the formation of zinc on the surface of the working electrode was reasonable in the electrolytes containing 10 ppm and 30 ppm of BPEI, the 3D image of the 300 ppm of additive shows inappropriate zinc growth on the surface of the electrode.

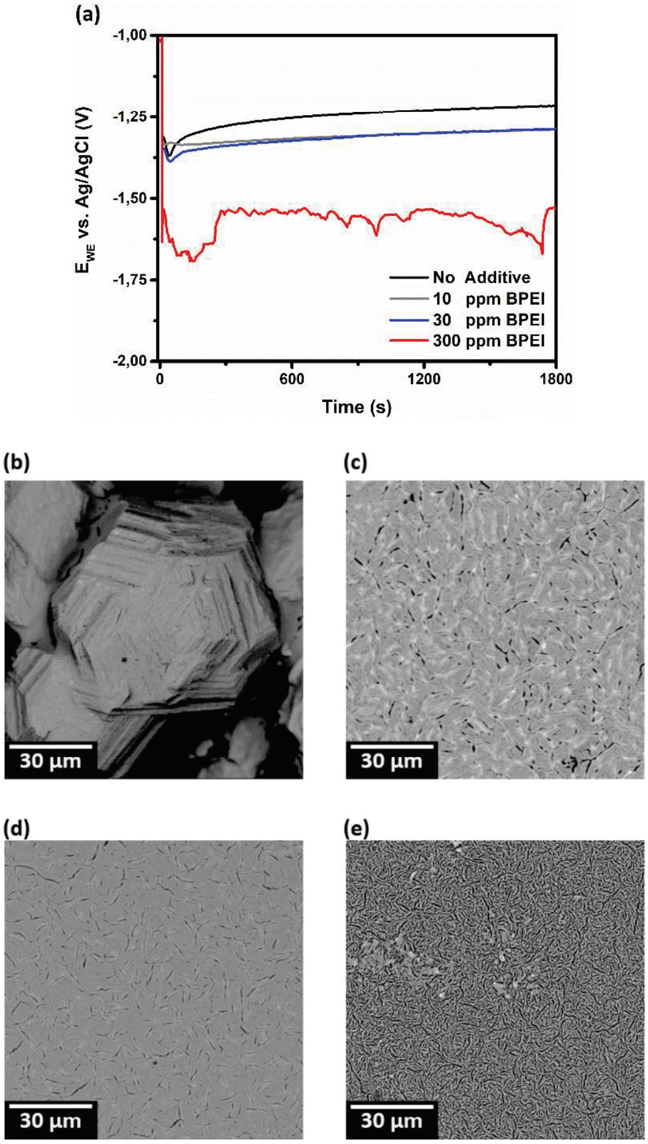

Figure 4-11: (a) Potential plot of the working electrode under an applied current density of -60 mA cm^{-2} in 500 mM of $ZnSO_4$ containing different concentrations of additive; (b-e) SEM images of the surface of the working electrode after zinc electrodeposition in an electrolyte without an additive, 10 ppm, 30 ppm, and 300 ppm of BPEI, respectively.

The reason for this electrodeposition of the layer stems from gas evolution during the measurement. Based on the observations, it was determined that gaseous bubbles formed immediately after beginning the experiment and remained on the surface of the electrode, as illustrated in Figure 4-3. The locations of these bubbles are indicated with red arrows in Figure 4-12. The bubbles prevented zinc ions from approaching to the surface of the working electrode. Thus, the zinc ions nucleated and grew on the other parts of the sample, which created a heterogeneous electrodeposition over the surface. The source of the bubbles could have been decomposition of water and hydrogen evolution or a side reaction of the additive on the surface of the electrode. As this problem appeared by increasing the level of the additive inside the electrolyte, the latter is more likely. This could be studied in greater detail in the future by employing DEMS and XPS methods.

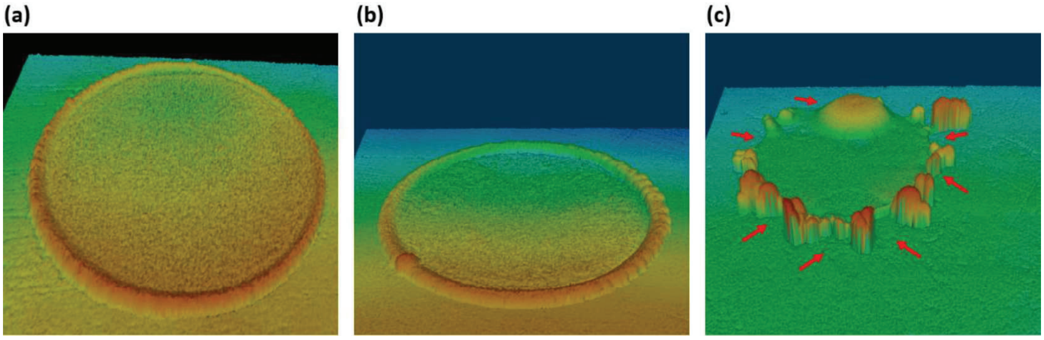

Figure 4-12: 3D laser microscope images from the surface of the working electrode after 30 minutes of zinc electrodeposition under the applied current density of -60 mA cm^{-2}: (a) 10 ppm BPEI, (b) 30 ppm BPEI, and (c) 300 ppm BPEI.

4.2.3. High Current Density: -110 mA cm^{-2}

Applying a high current density introduced an overpotential of 70 mV in the solution containing 10 ppm of BPEI and 300 mV in the presence of 300 ppm of additive as compared to the experiment without an additive in the electrolyte. These values were almost the same as in the previous experiment. For current densities larger than the limiting current density, the electrochemical reaction was under diffusion control of the ions. In this condition, increasing the current density may lead to the side reactions. In this case, the gas evolution was the most probable side reaction that could occurred. This may induce a convection of the electrolyte locally, near to the surface of the electrode, and lead to the more zinc electrodeposition by ions convection.

Moreover, the growth mechanism and potential response of the zinc at high applied current density was different from what it was in the earlier experiments.

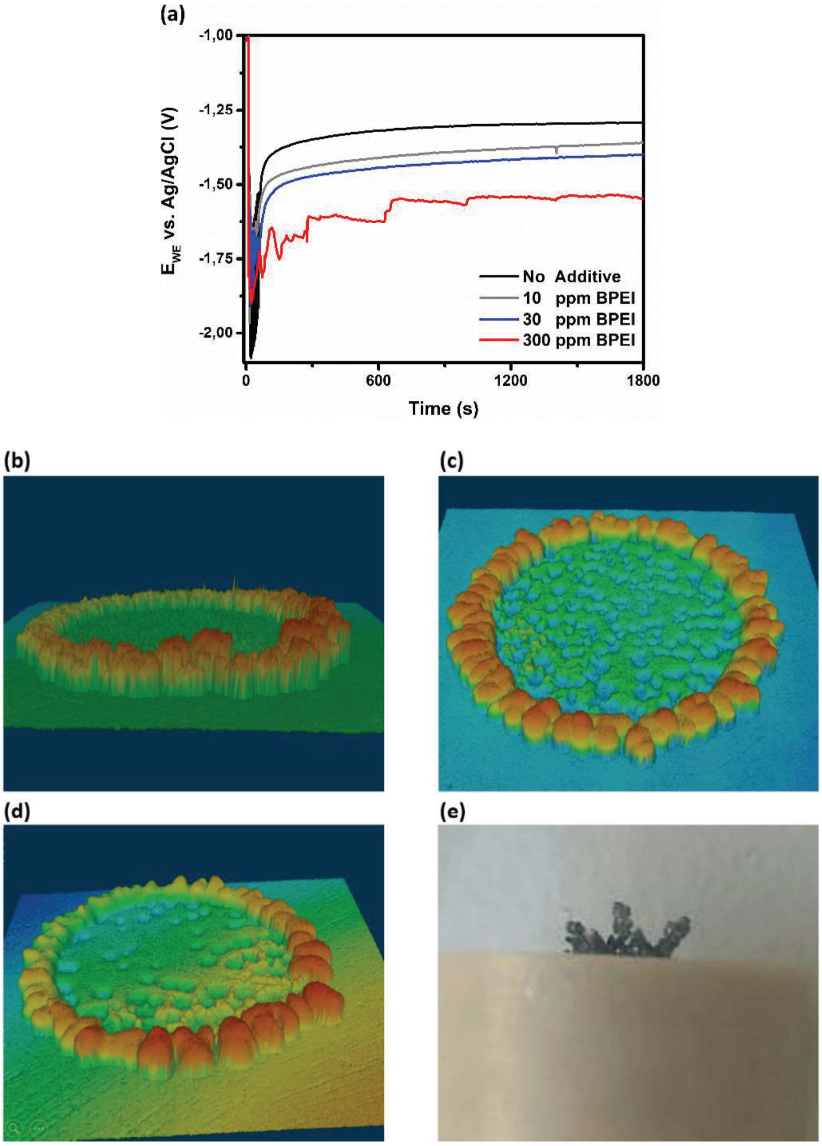

Figure 4-13: (a) Potential plot of the working electrode under an applied current density of -110 mA cm^{-2} in 500 mM of $ZnSO_4$ containing different concentrations of additive; (b-d) 3D laser images of the surface of the working electrode after zinc electrodeposition in an electrolyte without an additive, 10 ppm and 30 ppm of BPEI, respectively; and (e) An image of zinc electrodeposition at the edge of the sample in an electrolyte containing 300 ppm of BPEI.

First, a series of intense oscillations in the potential response could be observed during the first seconds of the experiment; this was true for all solutions. This intense oscillation can be explained by hydrogen evolution due to decomposition of water, and a side reaction of BPEI on the surface of the electrode that also generated a gaseous byproduct. In addition, in the case of applying 300 ppm of BPEI in the electrolyte, the length of the zinc deposited at the edge of the sample were larger than the range of the 3D laser microscope could encompass to make a 3D image (1-2 mm). Thus, a 3D image of this sample was not possible. To achieve a better understanding of electrodeposition mechanism in each case, a number of SEM images were taken. The mechanism of zinc growth in each case is explained below. Figure 4-14 shows zinc electrodeposition on the surface of a working electrode in 500 mM of $ZnSO_4$ containing 300 ppm BPEI.

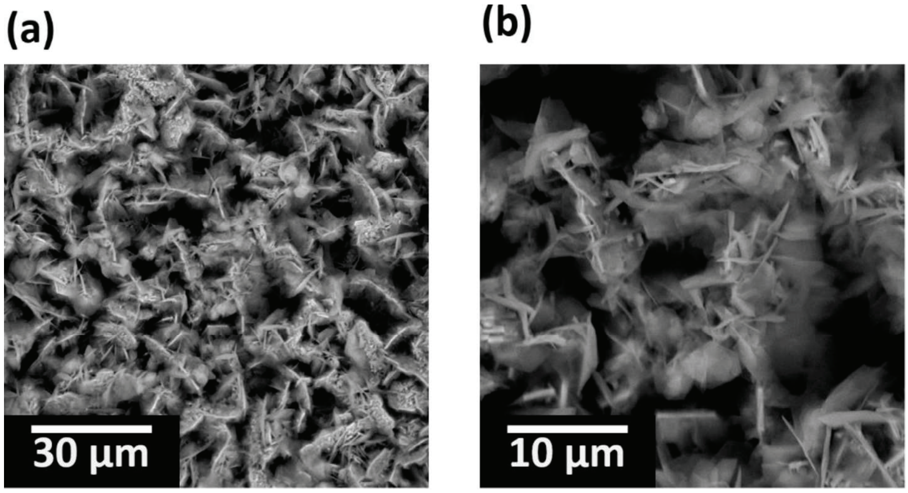

Figure 4-14: Electrodeposited zinc on the surface of a working electrode after 30 minutes of applying a current density of -110 mA cm^{-2} in 500 mM of $ZnSO_4$ containing 300 ppm of BPEI (the same location but on different scales).

When 300 ppm of BPEI was added to the electrolyte, needle-shaped zinc electrodeposition developed over the substrate. This type of growth could have been the source of the dendrite growth of zinc at the edge of the electrode that is shown in Figure 4-13(e). Dendrite growth can lead to a short circuit in the battery, and thus should be prevented. Therefore, adding 300 ppm of BPEI in the electrolyte at a high current density did not lead to promising results.

In the next experiment, 30 ppm of BPEI was added to the electrolyte. The SEM images of the surface of the working electrode are presented in Figure 4-15. The overall view of the surface of the electrode after running the experiment is illustrated in Figure 4-15(a). As can be seen in Figure 4-13(c) and 4-15(a), there were several holes on the surface of the electrode. These holes were formed due to the remaining bubbles of gas evolution on the surface of the working electrode during zinc electrodeposition. Therefore, zinc ions were deposited around the bubbles and holes appear on the surface.

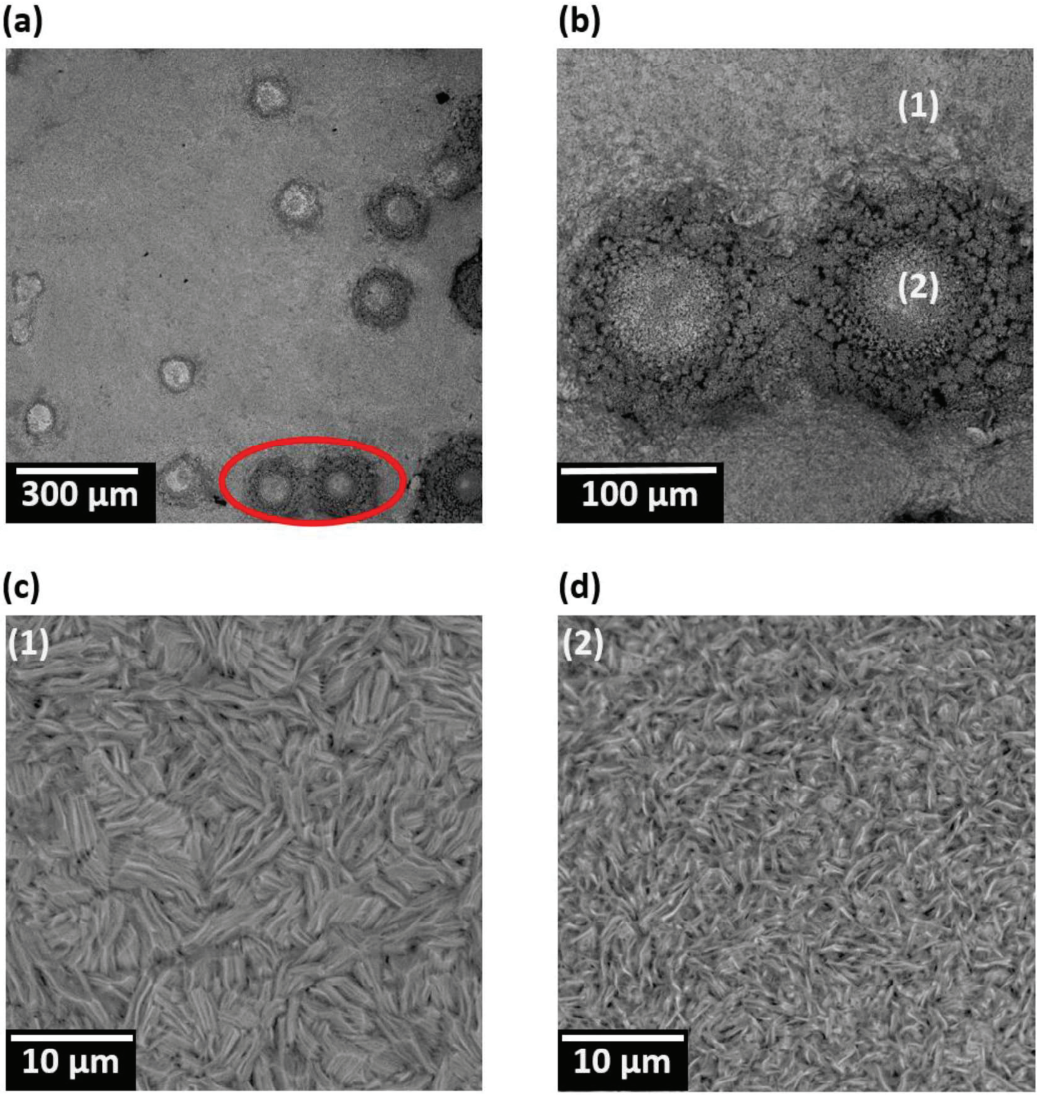

Figure 4-15: Electrodeposited zinc layer on the surface of the working electrode after 30 minutes of applying a current density of -110 mA cm^{-2} in 500 mM of $ZnSO_4$ containing 30 ppm of BPEI. (a) Overall view of the sample; (b) Magnification of the area indicated with a red oval in 4-15(a); (c) Magnification of the spot around the bubble indicated by (1) in 4-15(b); and (d) Magnification of the spot under the bubble indicated by (2) in 4-15(b).

Figure 4-15(b) shows the area indicated in Figure 4-15(a) with a red elliptical shape. Two different zones can be seen in this image. The first is the area around the remaining bubbles on the surface of the electrode, indicated by (1); the second is the region under the bubbles, indicated by (2).

To better understand the zinc electrodeposition mechanism in these regions, magnified images are presented in Figure 4-15(c) and (d). In both cases, the flat zinc texture was created by growth in a random direction. There was no evidence of large grain growth of a hexagonal shape. The same morphology of electrodeposited zinc layers in both areas can be attributed to adsorption of the additive on the surface that occurred before bubble formation. Thus, the cathodic overpotential also increased in that area, which could have modulated the applied current density all over the region and prevented preferential growth. The difference between regions (1) and (2) is the size of the zinc texture, which was finer in region (2). This can be explained by the remaining bubble on the surface of the electrode, which kept the zinc ions from reaching this area. Therefore, a finer zinc texture was formed in this region due to the lack of zinc ions from the electrolyte; more zinc ions would have resulted in further growth of the electrodeposited layer in this area.

In the last experiment for this section of the work, 10 ppm BPEI was added to the electrolyte, and the same experiment was run. Figure 4-16 presents the SEM images of this experiment. Similar to the last measurement, a number of bubbles were formed on the surface of the electrode and remained there during the experiment. Consequently, two different regions – around and beneath the bubble – were distinguishable. Figure 4-16(b-d) shows the morphology of the electrodeposited layer around the bubble. Here, the deposited zinc layers grew in a random direction, as was already seen in the case with a 30 ppm of additive. Moreover, there was no evidence of hexagonal plates in this region. The morphology of the electrodeposited zinc under the bubble was completely different. The images of this part of the sample can be found in Figure 4-16(e-g). In this region, very small hexagonal plates in the range of 1 to 3 µm were formed over the surface. This can be explained by the low concentration of the organic additive in the electrolyte. In both cases, around and underneath the bubbles, there was an initial adsorption of the additive on the surface. After that, more additive was adsorbed to the surface of the working electrode around the bubbles, which led to a homogeneous applied current distribution and a random growth of the electrodeposited layer. At the same time, the bubbles prevented further additive adsorption in the other region, which led to the formation of hexagonal zinc plates.

This study shows that the effect of BPEI as an additive on the morphology of electrodeposited zinc layers is concentration-dependent. Among the different concentrations of additive in 500 mM of $ZnSO_4$, the addition of 30 ppm of BPEI demonstrated the most promising results. Therefore, this concentration of additive was applied to study the effects of BPEI as an additive on zinc electrodeposition efficiency during cycling.

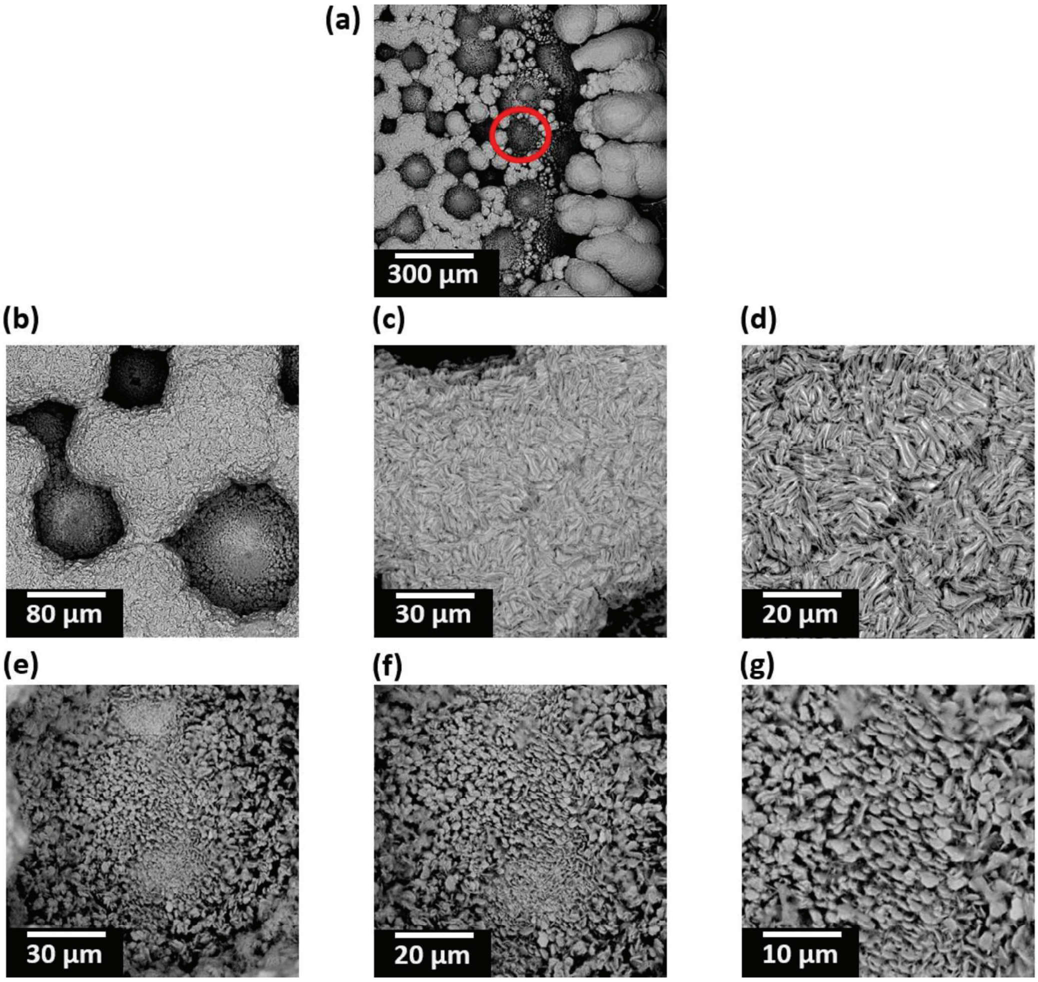

Figure 4-16: Electrodeposited zinc layer on the surface of the working electrode after 30 minutes of applying a current density of -110 mA cm^{-2} in 500 mM of $ZnSO_4$ containing 10 ppm of BPEI. (a) Overall view of the sample; (b-d) Morphology of the electrodeposited zinc layers around the bubbles at different magnifications; and (e-g) Morphology of the electrodeposited zinc layers under the bubbles at different magnifications.

4.3. The Effects of an Additive on Zinc Electrodeposition Efficiency

In the last part of this chapter, the effects of BPEI as an organic additive on the electrodeposition efficiency of zinc is discussed. As has already been mentioned, the electrodeposition efficiency of zinc is defined as the ratio of the charge flow during the oxidation of metallic zinc to the charge flow during the electrodeposition of Zn^{2+}, which in an ideal case should be equal to 100%. To study the electrodeposition efficiency, two different measurements were performed. In both cases, zinc slurry on carbon cloth (see experimental chapter under the section of electrode preparation), as the working electrode, was reduced for two hours, up to half of its theoretical capacity. Thereafter, it was oxidized up to -0.8 V vs. Ag/AgCl (3 M KCl). This procedure was run for 50 cycles. In both cases, the current density of 2 mA cm^{-1} was applied. This current density was calculated based on the apparent surface area of the working electrode. In the first measurement, 500 mM of $ZnSO_4$ was used as an electrolyte; this is labeled as "pure electrolyte" in the graphs. In the second experiment, the same electrolyte containing 30 ppm of BPEI was applied as the electrolyte. This was marked "30 ppm BPEI" in the graphs. Figure 4-17 shows the electrodeposition efficiency of zinc for 50 cycles.

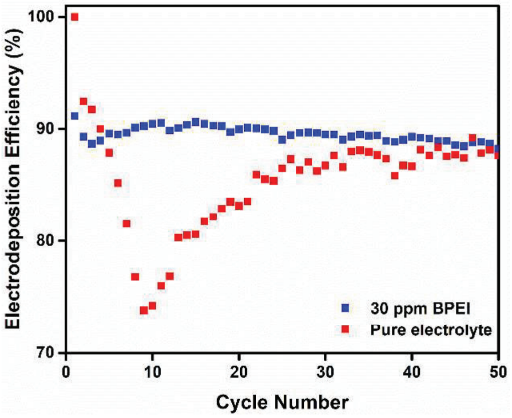

Figure 4-17: Zinc electrodeposition efficiency for 50 cycles in different electrolytes. The red dots show the electrodeposition efficiency in 500 mM of $ZnSO_4$ and the blue dots show the electrodeposition efficiency in the same electrolyte containing 30 ppm of BPEI as an additive.

In the first four cycles, the electrodeposition efficiency of the pure electrolyte was higher than 30 ppm BPEI. The electrodeposition efficiency of the pure electrolyte dramatically dropped to less than 75% after nine cycles and began to increase again to less than 88% after 50 cycles. In the presence of BPEI, the electrodeposition efficiency of the zinc remained almost constant, around 88%, after the same number of cycles. Therefore, adding the appropriate amount of organic additive to the electrolyte inhibited an abrupt drop in the electrodeposition efficiency and kept it almost stable during cycling.

As a means of illustrating the effect of adding BPEI to the electrolyte on the electrochemical response of the working electrode during zinc electrodeposition, a potential plot versus time for the first 10 cycles is presented in Figure 4-18.

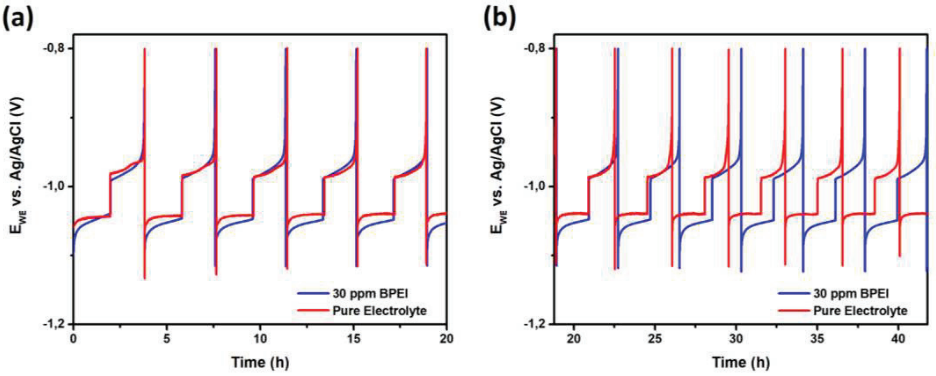

Figure 4-18: Potential plot of two different experiments versus time. (a) Cycles 1 to 5, and (b) Cycles 6 to 10.

From Figure 4-18, it can be seen that the presence of BPEI as an additive in the electrolyte had no effect on the oxidation step of the electrochemical reaction. This was determined from the superimposition of the potential plot of zinc oxidation in the pure electrolyte and 30 ppm BPEI. Moreover, the presence of BPEI in the electrolyte induced no additional overpotential at the end of the reduction step for the first cycle. With each increase in the cycle number, the additional cathodic overpotential was built up. The magnitude of the additional cathodic overpotential of 30 ppm BPEI with respect to the pure electrolyte reached 22 mV after 50 cycles. This additional cathodic overpotential induced surface polarization and more homogeneous current distribution during the zinc electrodeposition over the entire surface. Figure 4-18 also shows a longer oxidation time in the presence of 30 ppm BPEI, as a shift in the blue line with respect to the red line. This difference in oxidation time during cycling can be interpreted as additional proof of the role of an organic additive in the stabilization of zinc electrodeposition efficiency.

4.4. Conclusion

The efficiency of zinc electrodeposition on negative electrodes is of fundamental importance to improving the long-term performance of aqueous zinc-ion batteries. One approach to accomplishing this goal is introducing organic additives to the electrolyte. It has been shown that organic additives play an important role in modifying the surface roughness, grain size, and growth orientation of electrodeposited layers. This dissertation studied the mechanism of zinc electrodeposition with and without branched polyethyleneimine (BPEI) as an electrolyte additive at different current densities, as well as the effect of an additive on the electrodeposition efficiency of zinc.

In the absence of BPEI, two distinct growth mechanisms could be determined. When the current density was less than the limiting current density, a thin layer of zinc formed over the surface of the electrode without any preferential growth structure. Increasing the current density to more than the limiting current density thoroughly altered the growth mechanism and electrochemical reactions. The decomposition of water and hydrogen evolution became the predominant reactions during the first few seconds of the experiments; this resulted in an oscillation in the potential response of the working electrode within this period of time. As the reaction continued, the interval times of the oscillations got larger. After that, the potential of the working electrode became more stable. The growth of low surface energy planes was preferred over high surface energy planes, and the development of large hexagonal grains became the principle growth mechanism on the surface of the working electrode. The size of the hexagonal grains was decreased by increasing the applied current density.

The presence of BPEI as an additive to the electrolyte suppressed hexagonal grain growth at low, limiting, and high current densities. Adsorption of BPEI on the surface of the electrolyte decreased the surface area for zinc electrodeposition. Therefore, increasing the concentration of BPEI led to higher levels of adsorption of this additive on the surface of the working electrode and less surface area for zinc electrodeposition. This decreased the exchange current density for zinc electrodeposition. To compensate for this effect, the cathodic overpotential increased. Therefore, surface polarization was enhanced and the current distribution was modulated to be more homogenous. It was also demonstrated that the effect of BPEI as an additive on the morphology of electrodeposited zinc layers was concentration-dependent. High concentrations of the additive led to the heterogeneous electrodeposition mechanism, while low concentrations could not suppress the hexagonal growth at high current densities. Adding 30 ppm of BPEI introduced the best results in 500 mM of zinc sulfate.

Finally, the effect of the additive at low current densities on the electrodeposition efficiency of zinc was investigated. It was observed that the presence of the additive had no effect on the oxidation step, but it induced an additional cathodic overpotential after 50 cycles as compared to the pure electrolyte. This additional cathodic overpotential induced surface polarization and more homogeneous current distribution during zinc electrodeposition over the entire surface. Moreover, adding the appropriate amount of organic additive to the electrolyte inhibited an abrupt drop in the electrodeposition efficiency and kept it almost stable during cycling.

5. Layered Double Hydroxides as the Negative Electrode in Aqueous Zinc-Ion Batteries

It has already been shown that the level of hydrogen evolution is inversely proportional to the electrodeposition efficiency [132]. Therefore, increasing the efficiency of the zinc electrodeposition could be a means of suppressing hydrogen evolution on negative electrodes in aqueous zinc-ion batteries.

Layered double hydroxides (LDHs) are ionic lamellar compounds that perform well when used to increase the cyclability of negative electrodes in alkaline electrolytes [135–137]. To examine their performance in terms of zinc electrodeposition efficiency, a mixture of zinc and Zn-Al-Cu layered double hydroxide (LDH) was used as the negative electrode at a neutral pH. In this chapter, a brief introduction to LDH is presented. Thereafter, application of this compound in the field of energy storage, and particularly in rechargeable batteries, is discussed. Then, morphological and structural characterizations of as-synthesized LDH are presented via SEM and XRD. Next, a number of mixtures with different ratios of zinc to LDH are considered. Finally, the use of these mixtures as an active material in negative electrodes and the efficiency of zinc electrodeposition in 500 mM of zinc sulfate is examined.

5.1. An Introduction to Layered Double Hydroxides

Layered double hydroxides (LDHs) are ionic lamellar compounds [138] that were discovered in 1842 in Sweden. The exact formula of this structure was first introduced by Manasse in 1915 [139]. This structure is based on brucite [$Mg(OH)_2$]. A schematic construction of this compound is presented in Figure 5-1. In this structure, each magnesium ion is octahedrally surrounded by hydroxide ions. These octahedral components build two-dimensional sheets via edge sharing. The hydrogen bonding between the adjacent hydroxyl groups stacks these sheets together. These hydroxyl groups are perpendicular to the plane of octahedral units [140].

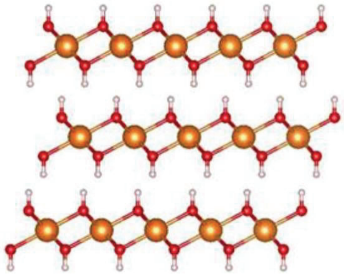

Figure 5-1: The structure of [$Mg(OH)_2$]: the orange spheres are magnesium atoms, red spheres are oxygen atoms, and white spheres are hydrogen atoms (reprinted from [141]).

LDH construction can be obtained when a part of the divalent cations in a brucite-like structure is substituted with trivalent cations. To compensate for the excess in positive charge, anions intercalate between the layers. A combination of hydrogen bonding and electrostatic effects bonds the interlayer anions to the octahedral sheets. Each anion balances a portion of the excess positive charge from the octahedral sheets. Therefore, the octahedral sheets are electrically stabilized by the two adjacent interlayers. To do so, the interlayer anions must interact with the polarized hydroxyl group, especially those that bond to the trivalent cations [140]. Thus, a generic formula for this type of compound can be written as follows:

$$[M_{1-x}^{2+}M_x^{3+}(OH)_2]^{x+}[A^{m-}]_{x/m} \cdot yH_2O \tag{5-1}$$

where M^{2+} and M^{3+} are metallic cations, A^{m-} represents the interlayer anions, and x can vary between 0.2 and 0.4 [138,142]. Usually, M^{2+} involves Zn^{2+}, Ni^{2+}, Mg^{2+}, or Cu^{2+}, while M^{3+} contains Al^{3+}, Fe^{3+}, Mn^{3+}, or Ga^{3+}. Interlayer anions (A^{m-}) can be organic or inorganic, such as Cl^-, $(SO_4)^{2-}$, $(CO_3)^{2-}$, or $(RCO_2)^-$ [138]. Water molecules also sit in the interlayer region. Different parameters such as the temperature, vapor pressure of the water, and nature of the anions affect the amount of water in that region. Therefore, accurately determining the nature of this layer can be intensely difficult [139]. LDH has widely been used as a catalyst [143], precursor for a catalyst [144,145], acid and CO_2 absorbent [146–148], electrochemical biosensor [149], DNA carrier [150], and anion exchanger [151,152]. In addition, this compound has often been applied in the field of energy storage, especially in Ni–Cd, Ni–Zn, and Ni–MH secondary alkaline batteries [135,153,154].

In 2002, Chen et al. [154] synthesized a series of Ni-Al LDHs, adding different weight percentages of zinc as a dopant. These researchers showed that adding zinc to the structure of LDH can improve the cyclability, reversibility, and discharge potential of the electrode in alkaline secondary batteries. Fan et al. [155] used Zn-Al LDH as a negative electrode in Ni-Zn secondary batteries. These researchers synthesized various LDHs with different ratios of zinc to aluminum, finding that a particular ratio can alter the electrochemical properties of LDH when it serves as an active material for negative electrodes. They also illustrated that this electrode is more stable than ZnO in alkaline media, and can be applied as a novel electrode for this type of battery. Yang et al. [156] mixed the same LDH as in [155] with nanostructured carbon nanotubes (CNTs) to form a LDH/CNT composite, which served as a high-performance electrode for Ni-Zn secondary batteries. They argued that the material has a superior cycle stability compared to conventional Zn-Al LDH. They also investigated the effects of silver as an additive on the electrochemical performance of Zn-Al LDH [157], finding that using silver as an additive can enhance the electrical conductivity of LDH and decrease the total polarization of the cell. Moreover, silver could be added to LDH in a more facile reaction than in the formation of an LDH/CNT composite. In another study [136], these same researchers proved that coating LDH sheets with silver could increase the activity of the negative electrode and decrease the charge-transfer resistance. This was another step towards increasing the stability of LDH during cycling.

In another study, Wang et al. [137,158] investigated tin and indium as additives in Zn-Al LDH, separately. Both compounds were synthesized by a hydrothermal method. In the case of tin, a more positive corrosion potential compared to the Zn-Al LDH was achieved. Moreover, reversibility and electrochemical performance were increased in the LDH as the anodic material in a Ni-Zn secondary cell. Adding indium increased the cycle stability of the anode from 300 to 800 cycles, without dendrite formation or a short circuit. Furthermore, Zn-Al-In LDH showed a higher rate capability and discharge capacity compared to Zn-Al LDH.

Wen et al. [159] evaluated the effects of copper as an additive in Zn-Al LDH on the electrochemical performance of the negative electrode in a Zn-Ni secondary battery. These researchers synthesized the compound via a constant pH co-precipitation method, finding that adding copper to the conventional LDH could increase the cycle stability of the electrode; the capacity of the electrode after 800 cycles was twice as large as that of the Zn-Al LDH. Moreover, higher reversibility and lower charge-transfer resistance was acquired, compared to the Zn-Al LDH. The morphology of the synthesized sample remained hexagonal, and the addition of copper had no negative effect on the morphology. The presence of a certain amount of copper actually increased the conductivity of the LDH. This can be explained by the fact that the standard electrode potential of $Cu(OH)_2/Cu$ is more positive than that of $Zn(OH)_2/Zn$. Therefore, the Cu^{2+} was reduced to metallic Cu in the initial cycles. This allowed it to attach to the lamellar structure of the LDH and provide a conductive network between the layers. Thus, the internal charge-transfer of the electrode was decreased. In other words, the conductivity was enhanced by using an appropriate amount of copper during the LDH preparation.

Finally, La Mantia et al. [132] used LDH to increase the zinc electrodeposition efficiency on the negative electrode of aqueous zinc-ion batteries at a neutral pH. This is understood as being the first time LDH was applied at a neutral pH. In that study, the researchers mixed conventional Zn-Al LDH with metallic zinc that served as the negative electrode in aqueous zinc-ion batteries, reporting that a certain ratio of zinc to LDH increased the electrodeposition efficiency from 85% to 98%.

Based on the aforementioned studies, Zn-Al-Cu LDH was synthesized in this research. The structure and morphology of the as-synthesized LDH was characterized by XRD and SEM, respectively. Finally, the performance of this material was examined in combination with different amounts of zinc to determine the electrodeposition efficiency of zinc in 500 mM of zinc sulfate.

5.2. Morphological and Structural Characterization of As-Synthesized Zn-Al-Cu LDH

The Zn-Al-Cu LDH was prepared as described in Chapter 2. The molar ratio of Zn:Al:Cu was 2.8:1.0:0.2. To determine the structural properties of this sample, a XRD measurement in the 2θ range between 5° to 80° was performed. The scan speed was 5 seconds and the step width was 0.025 degrees. The result of this experiment is illustrated in Figure 5-2.

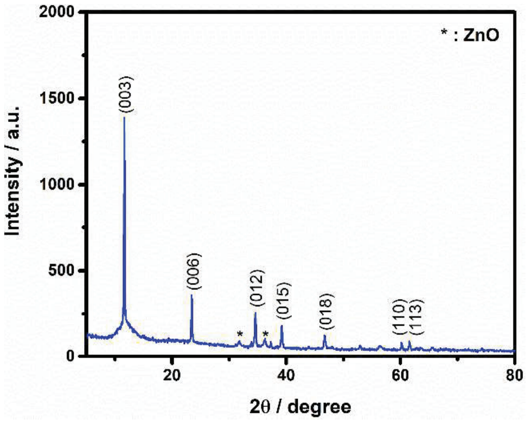

Figure 5-2: XRD data for the as-synthesized Zn-Al-Cu LDH powder.

The XRD data indicated two different phases in the powder. The first was the LDH and the second was ZnO. An analysis of the data showed that the sample contained 93% LDH and 7% ZnO. The formation of a minor amount of ZnO during LDH synthesis was common when the ratio of Zn to Al was larger than 2.3 [160]. The diffraction peaks of the as-synthesized LDH indicated that the sample was well-crystallized, because of the symmetrical and sharp peaks in the XRD pattern. These diffraction patterns were located at 2θ = 11.64°, 23.45°, 34.56°, 39.16°, 46.69°, 60.18°, and 61.54°, which corresponded to the space group of R-3m with the hexagonal lattice unit cell. A very intense peak at 2θ = 11.64° indicated a quality of crystallinity similar to that of hydrotalcite compounds. Therefore, adding the appropriate amount of copper to the LDH did not destroy the structure of this material.

Based on the aforementioned data, a hexagonal sheet-like morphology was expected. To form a better picture of the morphology of this sample, SEM images were taken. In order to obtain quality images, the sample was coated with a thin layer of a platinum and palladium alloy. These images are shown in Figure 5-3.

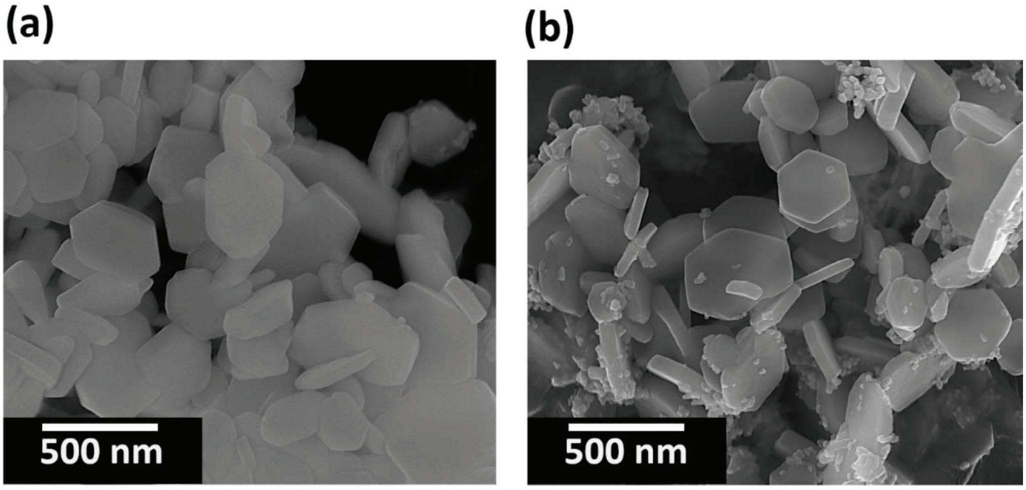

Figure 5-3: SEM images from the as-synthesized LDH powder in different positions.

As can be seen in this Figure, the morphology of the as-synthesized LDH was hexagonal and sheet-like. The sizes of the crystalline structures varied between 100 and 500 nm. This structure was homogeneously distributed throughout the sample. In addition, no crystal agglomeration was found in the powder. There were a number of small crystals; these can be observed in Figure 5-3(b). These crystals may have resulted from a breaking up of the larger crystals or a lack of crystal growth during the last step of the synthesis procedure. It should also be noted that the powder was unstable under the electron beam. To solve this problem, the energy of the electron beam was decreased to 10 KV. The other possible way of overcoming such a problem would have been to increase the scan rate of the SEM device. To investigate the ratio of zinc, aluminum, and copper elements throughout the structure, energy-dispersive X-ray spectroscopy (EDX) mapping was conducted. To do so, an area of 50×50 µm was chosen and the elemental distribution was analyzed in this area. To increase the count, the working voltage was raised to 50 KV. It should also be emphasized that the accuracy of the EDX instrument was 1 atomic percent. Therefore, any deviation less than this number can be attributed to instrument error. Figure 5-6 illustrates the result of this measurement.

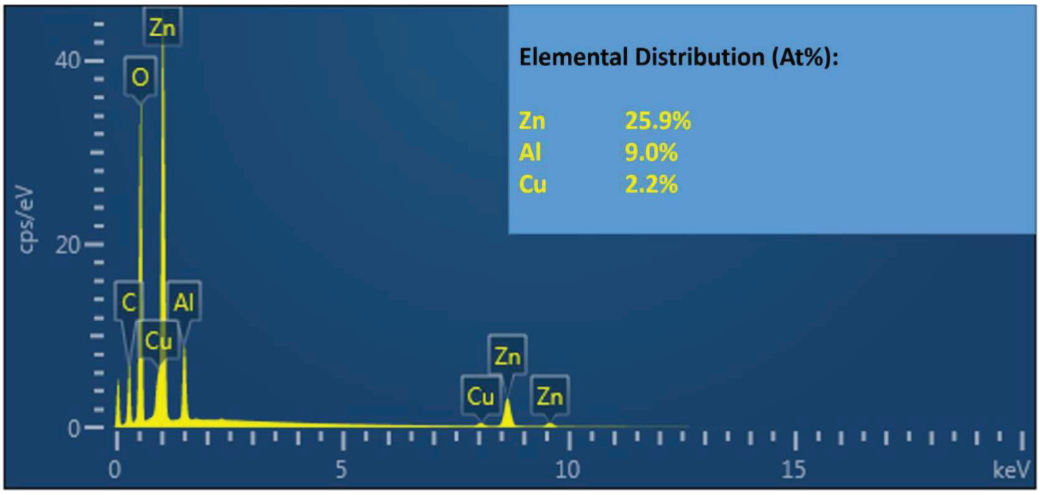

Figure 5-4: EDX mapping of an area of 50×50 µm.

The results indicated that the ratio of Zn, Al, and Cu in atomic percent was equal to 2.87:1.00:0.24. These results are in agreement with the elemental ratio determined during the synthesis of the LDH. In addition, EDX mapping was individually performed for each element in order to investigate the distribution of each in the structure of the as-synthesized LDH. Figure 5-5 shows the results; all elemental components were homogeneously distributed throughout the entire sample.

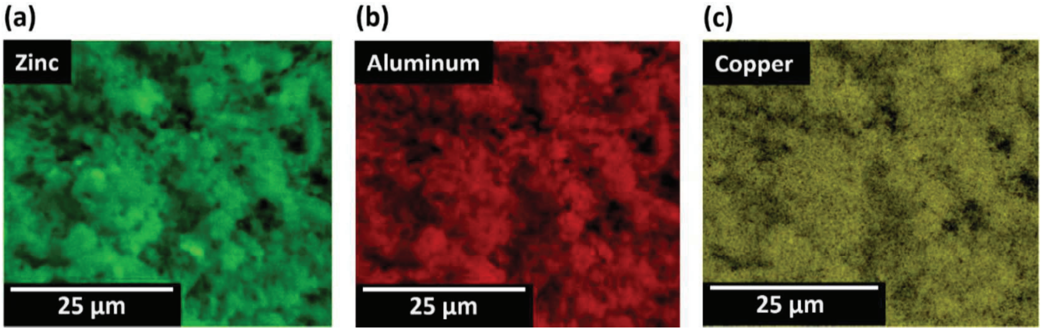

Figure 5-5: Elemental distribution throughout the sample: (a) zinc, (b) aluminum, and (c) copper.

Finally, three different points in this area were randomly selected and EDX measurements were individually performed at each. The results are shown in Figure 5-6.

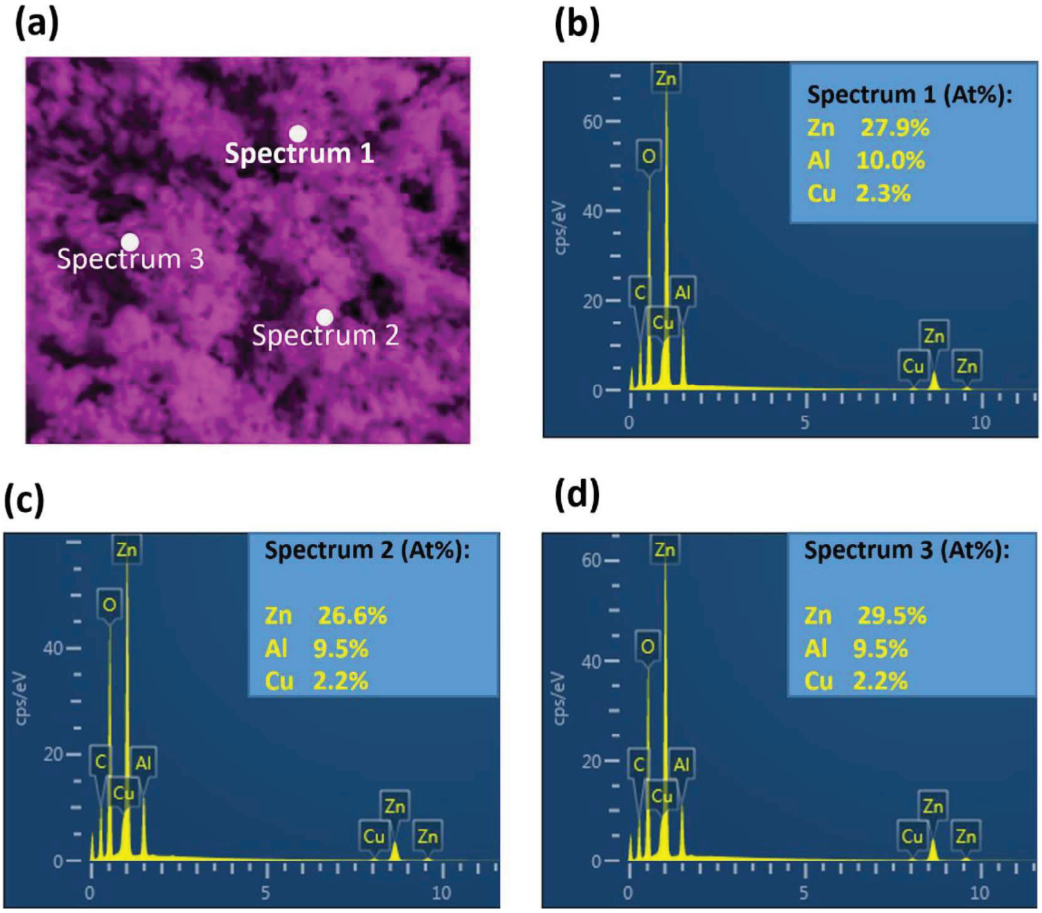

Figure 5-6: EDX data from three different points on the surface of the sample: (a) The position of the spectra and the elemental analysis at (b) Spectrum 1, (c) Spectrum 2, and (d) Spectrum 3.

The ratio of Zn:Al:Cu was equal to 2.79:1.00:0.25 in Spectrum 1. In Spectrums 2 and 3, this ratio was 2.80:1.00:0.23 and 3.14:1.00:0.23, respectively. The results of the EDX mapping, in combination with the SEM and XRD data, confirmed that the LDH was well-synthesized. The next section of this chapter is a description of this material being mixed with zinc in different ratios in order to investigate the electrodeposition efficiency of zinc in 500 mM of zinc sulfate.

5.3. Electrochemical Characterization of the Mixture of Zinc and LDH as a Negative Electrode in Aqueous Zinc-Ion Batteries

To study the performance of LDH as a negative electrode in aqueous zinc-ion batteries, the electrodeposition efficiency of zinc on this material was investigated. To do so, different electrodes with varying ratios of zinc to LDH were prepared. In total, four electrodes with Zn:LDH ratios of 1:0, 1:1, 2:1, and 1:2 were prepared. In all of the electrodes, the amount of PVDF in the NMP was kept constant. After the electrodes were prepared, they were reduced for two hours, up to half of the theoretical capacity of the zinc. Thereafter, they oxidized up to -0.8 V vs. Ag/AgCl (3 M KCl). In all cases, 500 mM of $ZnSO_4$ was used as the electrolyte. The results of these measurements are represented in Figure 5-7.

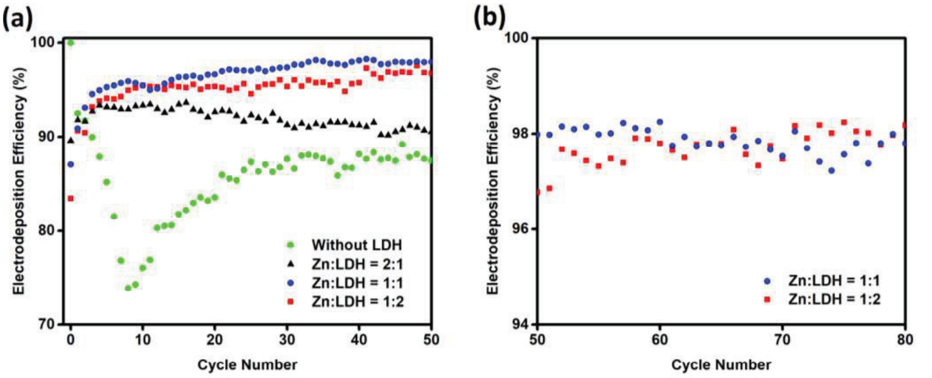

Figure 5-7: Efficiency of the electrodeposition of zinc on different negative electrodes in 500 mM of $ZnSO_4$: (a) The first 50 cycles for all four electrodes and (b) from cycle 50 to 80 for the electrodes with Zn:LDH = 1:1 and 1:2.

As illustrated in Figure 5-7(a), the electrodeposition efficiency of zinc varied on the different electrodes. When there was no LDH in the mixture, the electrodeposition efficiency was 100% in the first cycle. It then dramatically dropped to less than 75% after eight cycles and began to increase to less than 88% after 50 cycles. This can be explained by the fact that the zinc, upon contact with the water molecules, formed a thin layer of ZnO or $Zn(OH)_2$ on the surface; this decreased the electrodeposition efficiency. When this layer was electrochemically reduced, the zinc electrodeposition efficiency increased again.

After mixing the zinc with the LDH, the electrodeposition efficiency began with a magnitude of less than 90%. This magnitude was lower for the electrodes containing higher amounts of LDH. This can be attributed to the electrochemical inactivity of the LDH structure for zinc electrodeposition. When the ratio of zinc to LDH was 2 to 1, the electrodeposition efficiency reached 93% after 5 cycles and decreased to 88% at the end of the 50th cycle. In this mixture, the weight percent of the zinc was twice that of the LDH. Therefore, zinc became a dominant substrate for the electrodeposition reaction and reduced the efficiency of the electrodeposition at the end of the measurement. When the ratio of zinc to LDH was 1 to 1 or 1 to 2, an electrodeposition efficiency of more than 93% was achieved after the first three cycles. This can be attributed to the standard electrode potential of Cu^{2+}/Cu which is more positive than that of Zn^{2+}/Zn. Therefore, the Cu^{2+} was reduced to metallic Cu in the first cycles. This metallic coppers then attached to the lamellar structure of the LDH, which provided a conductive network between the layers. Thus, the internal charge-transfer of the electrode was decreased. In other words, the conductivity was enhanced by using an appropriate amount of copper during the LDH preparation. Moreover, the electrodeposition efficiency of more than 96% was recorded at 50th cycle for both electrodes. Therefore, the measurements for these two electrodes were continued up to 80 cycles. At the end of the 80th cycle, the electrode containing the mixture of 1 to 2 of Zn:LDH reached 98% of electrodeposition efficiency. This magnitude was 97.6% for the mixture of 1 to 1.

Although both mixtures reached almost the same electrodeposition efficiency at the end of the measurement, there was a significant difference between the results of these two electrodes. This difference was related to the number of cycles after which the electrodeposition efficiency of more than 97% was stabilized. This occurred after the 27th cycle in the case of Zn:LDH = 1:1 and the 52th cycle when the Zn:LDH = 1:2. The reason was the time the LDH structure required to be completely activated during the electrodeposition reaction. Increasing the amount of LDH in the active material of the electrode led to a longer amount of time for all LDH lamellar sheets to be electrochemically activated and became hosts for the zinc electrodeposition.

To study the effects of LDH on the potential drop at the beginning of the reduction step and sum of the anodic and cathodic overpotentials, the 1st, 25th, 50th, and 75th cycles of zinc electrodeposition efficiency for the different electrodes were sketched in Figure 5-8. Figure 5-8(a) shows the initial reduction and oxidation reactions for four different electrodes. When there was no LDH in the electrode, an electrodeposition efficiency of 100% was recorded. This became 89% in the case of Zn:LDH = 2:1, 87% when Zn:LDH = 1:1, and 83% when Zn:LDH = 1:2. Moreover, the electrode without LDH did not experience an intense potential drop at the beginning of the reduction reaction. The potential dropped to -1.060 V vs. Ag/AgCl (3 M KCl) and was flat in the rest of the experiment.

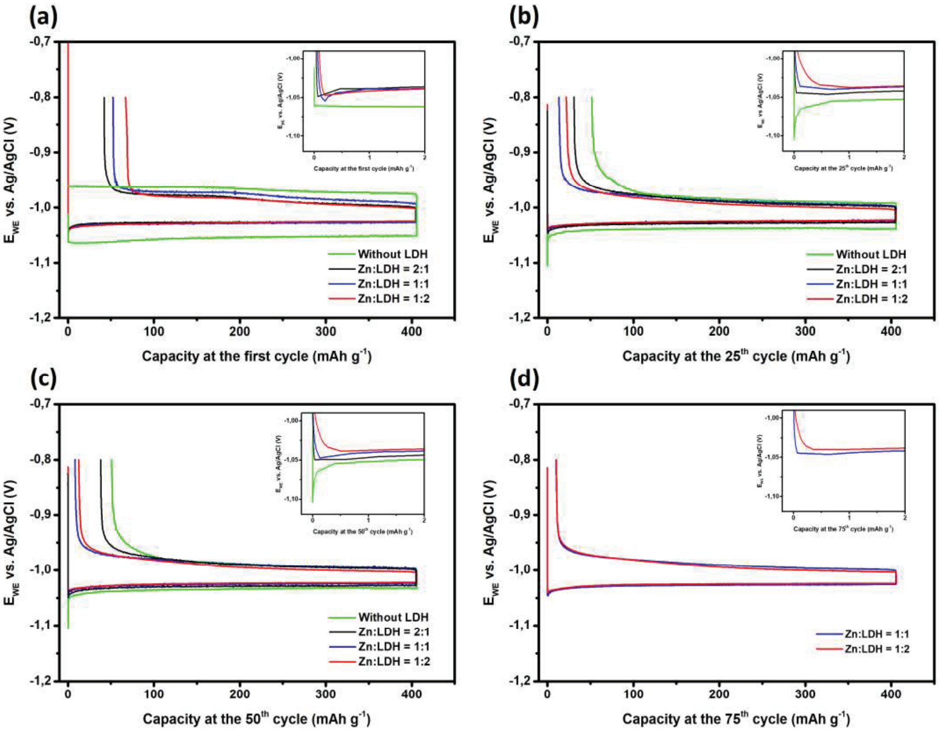

Figure 5-8: The zinc electrodeposition efficiencies of the different electrodes. The upper right graph is an enlargement of the potential drop at the beginning of the reduction: (a) 1st cycle, (b) 25th cycle, (c) 50th cycle, and (d) 70th cycle.

When the number of cycles reached 25 (see Figure 5-8(b)), an intense potential drop was observed at the beginning of the reduction reaction for the sample without LDH. The potential reached -1.105 V and then became flat at -1.050 V vs. Ag/AgCl (3 M KCl). This can be attributed to the surface morphology of the zinc electrode that caused an intense potential drop at the beginning of the reduction reaction and induced hydrogen evolution [132]. This behavior was also observed in the 50th cycle for the electrode without LDH, with the same magnitude of the potential drop as was recorded in the 25th cycle.

The electrochemical behavior of the electrodes containing LDH was completely different from that of the electrode without LDH. First, no evidence of an intense potential drop was detected at the beginning of the reduction reaction at the 1st, 25th, 50th, and 75th cycles. Therefore, using LDH as an active material for the negative electrode can decrease hydrogen evolution. Furthermore, increasing the amount of LDH in the electrodes decreased the level of cathodic overpotential. This is shown in the inserts of each graph in Figure 5-8. These images magnify the behaviors of different electrodes at the beginning of the reduction reaction. Although the potential drop in the electrodes containing LDH at the beginning of the reduction reaction in the first cycle varied randomly, this value changed in an ordered way in 25th, 50th, and 75th cycles. In particular, the potential drop, and consequently the cathodic overpotential, decreased with an increase in the percentage of LDH in the electrodes.

Finally, the sum of the anodic and cathodic potentials was studied in order to examine the kinetics of the reaction. Based on the Butler-Volmer equation, the kinetics were exponentially proportional to the magnitude of the overpotential. As discussed in Chapter 1, the kinetics of charging and discharging of a battery are important when using as ESS for grid-scale energy storage. Figure 5-8 illustrates that increasing the amount of LDH can decrease the sum of the anodic and cathodic overpotentials. This value was 42 mV when no LDH was used in the active material of the electrode, and decreased to 17 mV when the ratio of zinc to LDH was 1 to 2. The overpotentials values were 29 and 25 for Zn:LDH = 2:1 and Zn:LDH = 1:1, respectively. The reason for the decrease can be attributed to the lamellar structure of the LDH. Due to this structure, water molecules were able to diffuse between the layers. Therefore, zinc electrodeposition occurred on both sides of the lamellar structure, which increased the available surface of the electrode and kinetics of the reaction and decreased the sum of the cathodic and anodic overpotentials.

Based on the aforementioned properties, the electrode with the Zn:LDH = 1:2 was selected and its fast-cycling response in 500 mM of zinc sulfate was studied. To do so, the electrolyte was purged for 30 minutes before beginning the measurement to remove any residual oxygen. Next, the electrode was reduced under the current density of 0.5C for 10 cycles, up to half of the theoretical capacity of zinc, accompanied by an oxidation up to - 0.8 V vs. Ag/AgCl (3 M KCl) to activate the LDH structure. Finally, the current densities of 1C, 2C, 5C, and 1C were applied, each for 5 cycles. At each current density, a capacity of 410 mAh g^{-1} was achieved at the end of each reduction step and then the oxidation reaction was started. The results of this experiment are shown in Figure 5-9.

It should be noticed that the current density more than 5C was beyond the diffusion limiting current density of zinc electrodeposition in 500 mM of zinc sulfate. It meant that if the current density of 10C was applied, the reaction was under diffusion control that induced a high overpotential. Therefore, the results were not reliable.

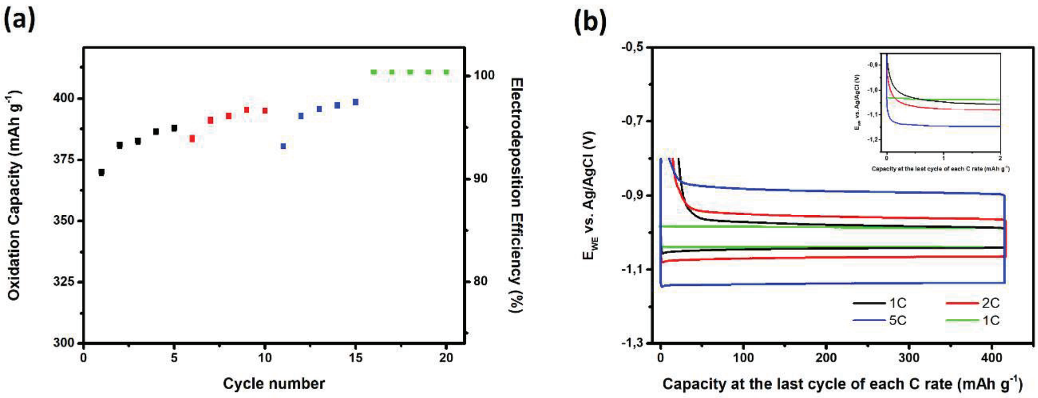

Figure 5-9: (a) The oxidation capacity and electrodeposition efficiency of Zn:LDH = 1:2 at different current densities and (b) The potential plot versus capacity at the 5th cycle of each current density in (a). The insert in (b) shows the potential drop at the beginning of the reduction reaction.

As represented in Figure 5-9(a), increasing the current density from 1C to 5C led to an increment in electrodeposition efficiency from 94 to 98%. Moreover, the oxidation capacity varied from 387 to 398 mAh g^{-1}. When the current density decreased from 5C to 1C again, the material have been experience an electrodeposition efficiency of 100%. Therefore, the oxidation capacity of 410 mAh g^{-1} was reached. This phenomena can be attributed to the more activated positions on the surface of the electrode at higher current densities. When the current density was increased, the ratio of zinc nucleation to the zinc growth was also increased. Therefore, the number of activated positions for zinc deposition at 5C was effectively enhanced. When the current density altered back from 5C to 1C, these activated positions on the surface of the electrode were appropriate spots for zinc electrodeposition and led to increase the efficiency to 100%. Finally, it can be observed that increasing the current density had no negative effect on potential drop at the beginning of the reduction reaction. This concluded from Figure 5-9(b) which is presented the potential profile at the last cycle of each current density. It is also obvious from this Figure that increasing the current density led to increase the sum of the anodic and cathodic overpotentials. This value was 51 mV for 1C, 98 mV for 2C, and 246 mV for 5C, respectively.

In the last experiment, the electrodeposition efficiency of the electrode containing the mixture of zinc and LDH with the ratio of 1 to 2 at 5C was studied. It means that the electrode was reduced to 410 mAh g^{-1} in 12 minutes and then oxidized up to -0.8 V versus Ag/AgCl (3 M KCl) as reference electrode. The results of this experiment are illustrated in Figure 5-10. For better resolution, the electrodeposition efficiency was recorded every 10 cycles in this graph.

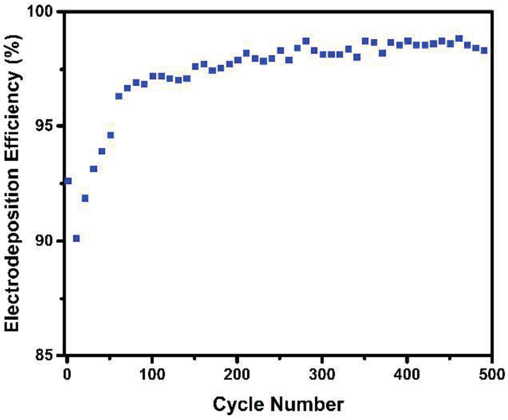

Figure 5-10: The zinc electrodeposition efficiency of Zn:LDH = 1:2 under current density of 5C for 500 cycles.

The electrodeposition efficiency of this electrode was 92.5% in the first cycle and dropped to 90% in the second cycle. Thereafter, it gradually increased up to more than 98%. It should be stressed that the efficiency reached more than 97% after 100th cycle and continued with the value equal or more than 97% in the following cycles. Moreover, the efficiency more than 98% reached after 250th cycle. The efficiency was more than 98% after this cycle. Therefore, this mixture can be applied at high current densities for long cycle life in grid scale energy storage systems where fast charging is a crucial parameter.

5.4. Conclusion

Layered double hydroxides (LDHs) are ionic lamellar compounds with a generic formula of $M_{1-x}^{2+}M_x^{3+}(OH)_2]^{x+}[A^{m-}]_{x/m} \cdot yH_2O$, where M^{2+} and M^{3+} are metallic cations and A^{m-} represents the interlayer anions. Usually M^{2+} involves Zn^{2+}, Ni^{2+}, Mg^{2+}, or Cu^{2+}, while M^{3+} is Al^{3+}, Fe^{3+}, Mn^{3+}, or Ga^{3+}. The LDH structure has widely been used as catalyst, precursor for a catalyst, acid and CO_2 absorbent, electrochemical biosensor, DNA carrier, and anion exchanger. In addition, it has often been applied in the field of energy storage devices, especially in Ni–Cd, Ni–Zn, and Ni–MH secondary alkaline batteries.

In this dissertation, Zn-Al-Cu LDH was synthesized and the structure and morphology characterized via XRD and SEM. The data indicated that the sample was highly crystalline, due to the symmetrical and sharp peaks in the XRD pattern. Moreover, the sample had a space group of R-3m, with a hexagonal lattice unit cell. A very intense peak at $2\theta = 11.64°$ indicated high crystallinity, similar to that of hydrotalcite compounds. Therefore, adding an appropriate amount of copper to the LDH did not destroy the structure of this material. The results of the SEM measurements for the as-synthesized LDH indicated that the morphology of the powders was hexagonal and sheet-like. The sizes of the crystalline structures varied between 100 and 500 nm. This structure was homogeneously distributed throughout the sample. The EDX results showed that the ratio of Zn to Al and Cu in atomic percent was equal to 2.87:1.00:0.24, respectively. These results were in agreement with the elemental ratio during the synthesis of the LDH.

Next, the performance of the LDH mixed with zinc and used as a negative electrode for aqueous zinc-ion batteries was electrochemically characterized. The best results were achieved when the ratio of the zinc to LDH was adjusted to 1 to 2. These results indicated that mixing the LDH with zinc could increase the electrodeposition efficiency of the zinc ions from 88% to 98% after 80 cycles. Moreover, the presence of LDH reduced the sum of the anodic and cathodic overpotentials during cycling from 42 to 17 mV. In addition, no evidence of an intense potential drop, which would have been a sign of the hydrogen evolution, was detected in the presence of the LDH being used as an active material for the negative electrode.

Finally, the performance of the Zn:LDH = 1:2 under a high current density was examined. The results showed that increasing the current density led to a slight increment in the electrodeposition efficiency. Therefore, a mixture of Zn:LDH = 1:2 could be a potential negative electrode in aqueous zinc-ion batteries where fast charging is a crucial parameter.

6. Water-in-Salt Electrolytes

As mentioned in previous chapters, the electrochemical stability window of pure water is 1.23 V under standard conditions. In such circumstances, elevating the cell voltage beyond 1.23 V is the primary reason for water electrolysis beginning on the surface of the electrodes. Water electrolysis produces molecular hydrogen and oxygen that leave the surface of the electrode in a gaseous form and provide free spaces for more electrolysis. Expanding the electrochemical stability window of the solution can suppress, or at least decelerate, the level of oxygen evolution on the surface of the positive electrode, and hydrogen evolution on the surface of the negative electrode. In rechargeable aqueous metal-ion batteries, hydrogen evolution occurs within a potential range of -0.24 to -1.07 V versus Ag/AgCl (3 M KCl). There are different methods of broadening the electrochemical stability windows of aqueous solutions. One approach is adding different salts to the water and adjusting the pH of the solution. Dushina et al. [46] demonstrated that the stability window of an electrolyte containing lithium sulfur as the salt can be increased up to 2.07 V, adjusting the pH to range between 6 and 8.

Another method for broadening the stability windows of aqueous electrolytes has recently been proposed; it involves using highly concentrated levels of salt in aqueous electrolytes [48]. This type of solution is called water-in-salt electrolytes. It shows a number of features that differentiate it from conventional electrolytes. First, due to having a lower number of water molecules than the amount required to make a formal solvation shell, distinctive physiochemical properties can be observed. These properties are present because of the dominance of interionic attractions. Moreover, changes in the solvation shell alter the electrochemistry of reactions at the interface between the electrode and electrolyte. Therefore, the electrochemical behavior of electrolytes can be controlled by manipulating the concentration of the salt [161].

It has already been shown that the electrochemical stability window of an aqueous solution containing 21 m of LiTFSI reached 3 V [48] (when m represents the ratio of mole of LiTFSI to kilogram of solvent). The reasons for selecting LiTFSI as the salt are its high solubility in water and great resistance to hydrolysis [162]. In addition, the ionic conductivity of this solution is almost ~10 mS cm^{-1}, which is similar to commercial organic electrolytes (9 mS cm^{-1}). Based on these properties, a number of studies have been devoted to the investigation of the performance of rechargeable batteries in water-in-salt electrolytes [163–170]. In all of these researches, cyclic voltammetry was applied as a characteristic method for determining the electrochemical stability window of the electrolyte. However, this technique is dynamic and not usually sensitive enough to measure the dependency of electrolyte decomposition on the potential [171]. In addition, rather than applying potential scan steps, most of the batteries are used at constant currents. Therefore, cyclic voltammetry has not been shown to be practical for determining the electrochemical stability window of an electrolyte in a battery.

Instead, it is better to apply a constant current density to examine the potential dependence of the electrolyte decomposition. Besides determining the electrochemical stability window, this method can also be used to make a direct assessment of the maximum cell voltage that can be applied for a particular rate of electrolyte decomposition. To perform such a measurement, two different experiments must be run in anodic and cathodic domains. For the anodic domain, a current density of 300 μA cm^{-2}, followed by 100 μA cm^{-2} and 10 μA cm^{-2}, must be applied for 30 minutes each. The measurement involves repeating the second and the third steps two additional times. Afterwards, the potential of the working electrode is recorded as the oxidation potential, E_a. The measurements in the cathodic domain are carried out by a means similar to that of the calculation for the anodic domain, but by applying negative current values. The recorded value of the potential is called the reduction potential, E_c. The stability window, ΔE, is the difference between E_a and E_c [46].

To run this experiment for this Ph.D. work, platinum (Pt) and glassy carbon (GC) electrodes were used as the working electrode. Platinum mesh, serving as the counter electrode, was placed around the working electrode, and Ag/AgCl (3 M KCl) was used as the reference electrode. Figure 6-1 shows the results of this experiment.

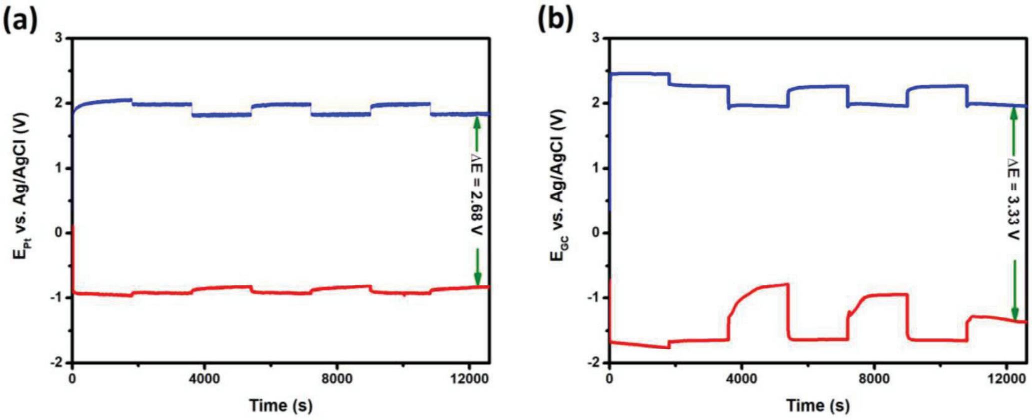

Figure 6-1: Electrochemical stability window of 21 m of LiTFSI on the (a) Platinum electrode, and (b) Glassy carbon electrode after applying different levels of a constant current.

The oxidation potentials, E_a, for 21 m of LiTFSI on the Pt and GC electrodes were equal to 1.85 and 1.96 V versus Ag/AgCl (3 M KCl), respectively. Subsequently, the values of the reduction potentials for these electrodes were determined to reach -0.82 and -1.37 V versus the same reference electrode. Therefore, the stability windows of the above mentioned solution were equal to 2.68 V with Pt as the working electrode, and 3.33 V with GC as the working electrode. These values are much higher than what has been previously achieved by adjusting the pH of the solution [46].

The reason the stability window of a water-in-salt solution expands as compared to conventional electrolytes can be explained by the formation of an electrolyte-electrode interphase [48]. This can increase the electrochemical stability windows of aqueous electrolytes beyond the thermodynamic value of water electrolysis. In conventional solutions, there is no possibility of the formation of a solid-electrolyte interphase (SEI), because none of the water decomposition that is comprised of H_2, O_2, or OH^- is capable of forming such an SEI layer. Therefore, the working potential and energy density of these batteries are restricted. Moreover, these batteries usually experience significant capacity fading during cycling.

In 1 m of LiTFSI solution, the ratio between the H_2O and Li^+ is 53.8. This ratio decreases to 2.6 in 21 m of LiTFSI solution [170]. Since the hydration shell of lithium ions usually contains six water molecules, the number of free water molecules in water-in-salt solutions is almost zero. Moreover, the absolute value of the $TFSI^-$ reduction is less than that of the water electrolysis. Thus, the formation of an SEI layer can be attributed to the reduction of bistrifluoromethanesulfonimidate (TFSI) on the surface of the negative electrode, which results in a passivation process [168]. It has already been shown that the $TFSI^-$ is electrochemically reduced to LiF [172]. Therefore, an SEI layer containing LiF is created on the surface of the negative electrode. This prevents water decomposition at the surface of the electrode, but permits lithium intercalation into the negative electrode [48]. On the other side, the potential for oxygen evolution is also shifted towards higher values. This can suppress, or at least decrease, the level of oxygen evolution when high-voltage cathodic materials are used in a battery system. The reason for this can be explained by the lower level of activity of the water molecules, due to a strong coordination with a high number of lithium ions and an increase in the presence of TFSI anions in the inner Helmholtz layer [48,170].

The other fact that can be extracted from Figure 6-1 is related to the difference between E_a and E_c in platinum and glassy carbon. In both cases, the absolute value of the potential is higher, when glassy carbon is applied as a working electrode. This difference in this work was equal to 100 mV in the case of oxidation potential; in reduction potential a difference of 550 mV was observed. Therefore, the difference in the cathodic domain was five times higher than in the anodic domain. In addition, the electrochemical stability window of the water-in-salt electrolyte showed a higher value when glassy carbon was used as the electrode than when platinum was used. This can be attributed to the high electrocatalytic feature of platinum for hydrogen evolution. This electrode showed a small Tafel slope and extremely high exchange current density for hydrogen evolution [173]. As compared to the platinum, the glassy carbon showed less catalytic activity for hydrogen evolution [174]. Therefore, the activity of the electrode for gas evolution was the main reason for the difference in the stability window when using different working electrodes. The accumulation of the TFSI anions could be another reason for such a behavior. More spectroscopic investigation is required to understand the role of anion accumulation in the electrochemical stability window of the electrolyte.

To better compare the electrochemical stability windows of different types of electrolytes, a floating column chart using standard lithium electrochemical reaction as a reference is included as Figure 6-2. Although the electrochemical stability window of an aqueous electrolyte is below that of organic electrolytes, applying a highly-concentrated electrolyte seems to be an excellent step forward toward improving grid-scale energy storage systems. A combination of 21 m of LiTFSI with $ZnSO_4$ could serve as an improved electrolyte for aqueous zinc-ion batteries.

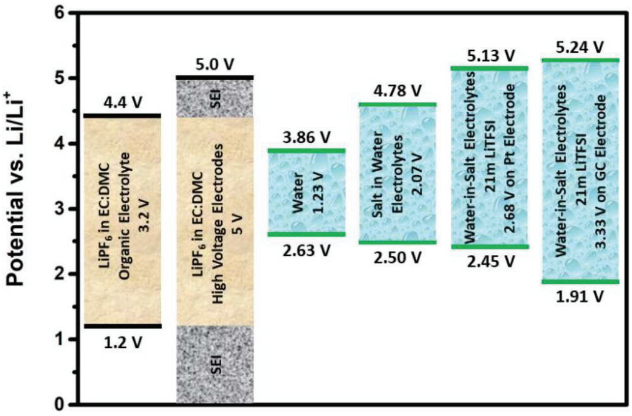

Figure 6-2: Electrochemical stability windows of different electrolytes.

7. Conclusions

One of the major challenges nowadays and in the future involves providing enough energy to meet global demands, without impacting the environment. Storing energy from renewable sources, such as wind and the sun, will soon be an indispensable means of addressing this problem. Rechargeable aqueous zinc-ion batteries are a promising energy storage system for this purpose, due to their low cost, high ionic conductivity, safety, non-flammability, and environmental friendliness. However, zinc-based negative electrodes suffer from hydrogen evolution, which negatively influences battery performance, hinders power density, and lowers the total specific energy. This can inversely influence the electrodeposition efficiency of the zinc during cycling. To further develop this type of battery, an electrochemical and morphological characterization of the interface at the negative electrode was required, in order to properly understand the main and side electrochemical reactions occurring therein.

To accomplish this goal, three different strategies were employed in this dissertation. First, a novel electrochemical cell was designed to observe gas evolution *in-operando* during battery cycling. In this way, more detailed information about the source of the gas evolution produced during cycling could be obtained. Second, a design of the components of the electrolyte was performed. It was believed that the electrolyte additives and water-in-salt solutions would suppress hydrogen evolution, stabilize electrodeposition efficiency, and expand the stability window of the electrolyte. Third, the active material of the negative electrode was mixed with solid-state additives to increase the zinc electrodeposition efficiency and lower the level of gas evolution.

To accomplish the first approach, two different electrochemical cells were designed and fabricated. Additionally, a unique setup for running DEMS measurements was introduced. Different parameters such as the position, size, and shape of the electrodes, flow of the carrier gas, and contact between the current connectors and electrodes were all analyzed. In particular, the best contact between the current connectors and electrodes in the second cell was obtained when a small spring properly affixed the electrode to the current connector. The first cell achieved an 85% of gas collection efficiency, and the second reached more than 98%. The performance of the cells was validated via a reliable combination of DEMS and CV measurements, in which benchmarked gas evolution during the lithium ion intercalation and deintercalation into and from the graphite electrode was used as standard test. The results were in complete agreement with previous outcomes.

Briefly, during the first reduction, ethylene evolution occured due to the decomposition of the electrolyte and formation of the SEI layer. Hydrogen evolution was also observed for all cycles accompanied by CO_2 evolution in the first cycle. This could be attributed to the residual water inside the electrode that decomposed to H^+ and OH^- during the first reduction of the graphite electrode. Thereafter, OH^- caused a ring to open in the ethylene carbonate molecules and reacted with them. This reaction produced alkyl di-alcoholates and CO_2. The latter could be detected with the mass spectrometer. The same results were obtained via a combination of GCPL and DEMS. It must be stressed that these DEMS cells indicated gas evolution throughout the entire system, and thus were not suitable for studying gas evolution in one individual electrode. The cells were also applied to observe hydrogen evolution in aqueous zinc-ion batteries. The results revealed that the magnitude of hydrogen evolution increased more than 10 times from the first cycle to the seventh, and then decreased moderately. This phenomenon can be explained by the fact that the zinc, upon contact with water, formed a thin layer of ZnO or $Zn(OH)_2$ on the surface; this blocked further hydrogen evolution. When this layer was electrochemically reduced, the hydrogen evolution began again. In addition, it was determined that increasing the concentration of the electrolyte decreased the amount of hydrogen evolution. This effect was comprehensively explained via electrochemical kinetics and thermodynamic considerations.

To perform the second approach, two distinct modifications were imposed on the electrolyte. In the first attempt, the mechanism of zinc electrodeposition efficiency in 500 mM of zinc sulfate was studied, and the effects of the additive on the electrodeposition efficiency of zinc were characterized. The results demonstrated that in the absence of an additive, two different growth mechanisms were distinguishable. If the current density was adjusted to be less than the limiting current density, no evidence of preferential growth was observed on the surface of the electrode. For current densities higher than this value, the growth of low surface energy planes was preferred over high surface energy planes, and the development of large hexagonal grains became the principle growth mechanism on the surface of the working electrode. The size of the hexagonal grains was decreased by increasing the applied current density. Moreover, the decomposition of water and hydrogen evolution became the predominant reactions during the first few seconds of the experiments; this resulted in an oscillation in the potential response of the working electrode within this period of time. The presence of BPEI as an additive in the electrolyte suppressed the hexagonal crystal growth at low, limiting, and high current densities. Adsorption of BPEI on the surface of the electrolyte decreased the exchange current density for zinc electrodeposition and increased the cathodic overpotential. Therefore, the surface polarization was enhanced and the current distribution was modulated to be more homogenous. It was also demonstrated that the effect of BPEI as an additive on the morphology of electrodeposited zinc layers was concentration-dependent. A high concentration of the additive led to a heterogeneous electrodeposition mechanism, while low concentrations could not suppress the hexagonal growth at high current densities. Adding 30 ppm of BPEI introduced the best results in 500 mM of zinc sulfate. Finally, the effect of the additive at a low current density on the electrodeposition efficiency of zinc was investigated. It was observed that adding the appropriate amount of organic additive to the electrolyte inhibited an abrupt drop in the electrodeposition efficiency and kept it almost stable during cycling.

In the second attempt to modify the electrolyte, the electrochemical stability window of water-in-salt electrolytes was studied. The results showed that the stability window of 21 m of LiTFSI was 2.68 V when platinum was used as the working electrode. This value was 3.33 V in the case of glassy carbon. The reason the reduction potential of a water-in-salt solution was more negative than that of conventional electrolytes was the formation of an SEI layer on the surface of the electrode. This was attributable to the reduction of $TFSI^-$ on the surface of the negative electrode, which results in a passivation process. The reason for a more positive oxidation potential as compared to conventional electrolytes was the lower level of activity of the water molecules, due to a strong coordination with a high number of lithium ions and an increase in the presence of TFSI anions in the inner Helmholtz layer of the positive electrode.

To accomplish the third part of this dissertation, the LDH structure was studied as a potential active material for the negative electrode. A sample of Zn-Al-Cu LDH was synthesized and the structure and morphology characterized via XRD and SEM. The data indicated that the sample was highly crystalline and had a space group of R-3m, with a hexagonal lattice unit cell. The results of the SEM measurements for the as-synthesized LDH showed that the morphology of the powders was hexagonal and sheet-like and their sizes varied between 100 and 500 nm. The EDX results showed that the ratio of Zn to Al and Cu in atomic percent was equal to 2.87:1.00:0.24, which was in agreement with the elemental ratio during the synthesis of the LDH. Next, the performance of the mixture of zinc and LDH as a negative electrode for aqueous zinc-ion batteries was electrochemically characterized. The best results were achieved when the ratio of the zinc to LDH was adjusted to 1:2. These results indicated that mixing the LDH with zinc could increase the electrodeposition efficiency of zinc ions from 88% to 98% after 80 cycles. Moreover, the presence of LDH reduced the sum of the anodic and cathodic overpotentials during cycling from 42 to 17 mV. The reason for this can be explained via the lamellar structure of LDH; water molecules were able to diffuse between the layers. Therefore, zinc electrodeposition occurred on both sides of the lamellar structure, which increased the kinetics of the reaction and decreased the sum of the cathodic and anodic overpotentials. In addition, no evidence of an intense potential drop, which would have introduced hydrogen evolution, was detected when LDH was used as an active material for the negative electrode. Finally, the performance of Zn:LDH = 1:2 under a high current density was examined. The results showed that increasing the current density led to a slight increment in the electrodeposition efficiency. Thus, a mixture of Zn:LDH = 1:2 could serve as a potential negative electrode in aqueous zinc-ion batteries in which fast charging is a crucial parameter.

To sum up, a differential electrochemical mass spectrometry technique was used to *in-operando* study gas evolution in aqueous zinc-ion batteries. It is believed that further developments of this DEMS technique will allow for more detailed studies of the main and side electrochemical reactions that occur during battery cycling, upon which the final performance is highly dependent. Moreover, increasing the specific surface area of the active material in the negative electrode, using highly-concentrated electrolyte, and modulating the current density over the entire surface are crucial to reducing hydrogen evolution, increasing electrodeposition efficiency, enhancing cyclability, and improving the performance of aqueous zinc-ion batteries.

8. Bibliography

[1] R.E. Smalley, Future Global Energy Prosperity: The Terawatt Challenge, MRS Bull. 30 (2005) 412–417. doi:10.1557/mrs2005.124.

[2] S. Randalls, History of the 2°C climate target, Wiley Interdiscip. Rev. Clim. Chang. 1 (2010) 598–605. doi:10.1002/wcc.62.

[3] P. Gerland, A. Raftery, H. Sevsikova, N. Li, N. Gu, T. Spoorenberg, World population stabilization unlikely this century, Science. 346 (2014) 234–237. doi:10.1126/science.1257469.

[4] H.D. Yoo, E. Markevich, G. Salitra, D. Sharon, D. Aurbach, On the challenge of developing advanced technologies for electrochemical energy storage and conversion, Mater. Today. 17 (2014) 110–121. doi:10.1016/j.mattod.2014.02.014.

[5] Climate Changes 2014, Synthesis report, 2014. https://www.ipcc.ch/pdf/assessment-report/ar5/syr/SYR_AR5_FINAL_full_wcover.pdf

[6] B. Pinnangudi, M. Kuykendal, S. Bhadra, Smart Grid Energy Storage, Elsevier Ltd, 2017. doi:10.1016/B978-0-12-805321-8.00004-5.

[7] G.A. Jones, K.J. Warner, The 21st century population-energy-climate nexus, Energy Policy. 93 (2016) 206–212. doi:10.1016/j.enpol.2016.02.044.

[8] B.P. Roberts, C. Sandberg, The Role of Energy Storage in Development of Smart Grids, Proc. IEEE. 99 (2011) 1139–1144. doi:10.1109/JPROC.2011.2116752.

[9] Grid integration of large-capacity Renewable Energy sources and use of large-capacity Electrical Energy Storage, 2012. http://www.iec.ch/whitepaper/pdf/iecWP-gridintegrationlargecapacity-LR-en.pdf.

[10] S. Lichtner, R. Bridle, L. Pack, Electric Power Industry Needs for Grid-Scale Storage Applications, (2010) 1–40. http://energy.gov/sites/prod/files/oeprod/DocumentsandMedia/Utility_12-30-10_FINAL_lowres.pdf.

[11] Electrical Energy Storage, 2011. http://www.iec.ch/whitepaper/pdf/iecWP-energystorage-LR-en.pdf.

[12] X. Luo, J. Wang, M. Dooner, J. Clarke, Overview of current development in electrical energy storage technologies and the application potential in power system operation, Appl. Energy. 137 (2015) 511–536. doi:10.1016/j.apenergy.2014.09.081.

[13] M. Mueller, L. Viernstein, C.N. Truong, A. Eiting, H.C. Hesse, R. Witzmann, et al., Evaluation of grid-level adaptability for stationary battery energy storage system applications in Europe, J. Energy Storage. 9 (2017) 1–11. doi:10.1016/j.est.2016.11.005.

[14] K.M. Colbow, J.R. Dahn, R.R. Haering, Structural and electrochemistry of the spinel oxides $LiTi_2O_4$ and $Li_{43}Ti_{53}O_4$, J. Power Sources. 26 (1989) 397–402. doi:10.1016/0378-7753(89)80152-1.

[15] P.G. Bruce, B. Scrosati, J.-M. Tarascon, Nanomaterials for rechargeable lithium batteries, Angew. Chem. Int. Ed. 47 (2008) 2930–2946. doi:10.1002/anie.200702505.

[16] Y. Mekonnen, A. Sundararajan, A.I. Sarwat, A Review of Cathode and Anode Materials for Lithium-Ion Batteries, Southeast Con(2016) 2–7. doi:10.1109/SECON.2016.7506639.

[17] K.C. Kam, M.M. Doeff, Electrode Materials for Lithium Ion Batteries, Mater. Matters. 7 (2012) 56–60.

[18] X. Chen, W. Shen, T.T. Vo, Z. Cao, A. Kapoor, An overview of lithium-ion batteries for electric vehicles, 2012 10th Int. Power Energy Conf. (2012) 230–235. doi:10.1109/ASSCC.2012.6523269.

[19] K. Kang, Y.S. Meng, J. Breger, C.P. Grey, G. Ceder, Electrodes with High Power and High Capacity for Rechargeable Lithium Batteries, Science. 311 (2006) 977–980. doi:10.1126/science.1122152.

[20] D. Mohanty, S. Kalnaus, R. a. Meisner, K.J. Rhodes, J. Li, E.A. Payzant, et al., Structural transformation of a lithium-rich $Li_{1.2}Co_{0.1}Mn_{0.55}Ni_{0.15}O_2$ cathode during high voltage cycling resolved by in situ X-ray diffraction, J. Power Sources. 229 (2013) 239–248. doi:10.1016/j.jpowsour.2012.11.144.

[21] N. Nitta, F. Wu, J.T. Lee, G. Yushin, Li-ion battery materials: present and future, Mater. Today. 18 (2015) 252–264. doi:10.1016/j.mattod.2014.10.040.

[22] M.S. Whittingham, Lithium batteries and cathode materials, Chem. Rev. 104 (2004) 4271–4301. doi:10.1021/cr020731c.

[23] A.K. Shukla, T.P. Kumar, Materials for next-generation lithium batteries, Curr. Sci. 94 (2008) 314–331.

[24] M. Islam, A. Omole, A. Islam, A. Domijan, Dynamic capacity estimation for a typical grid-tied event programmable Li-$FePO_4$ battery, IEEE Int. Energy Conf. Exhib. EnergyCon 2010. (2010) 594–599. doi:10.1109/ENERGYCON.2010.5771751.

[25] J.-F. Colin, V. Godbole, P. Novák, In situ neutron diffraction study of Li insertion in $Li_4Ti_5O_{12}$, Electrochem. Commun. 12 (2010) 804–807. doi:10.1016/j.elecom.2010.03.038.

[26] M. Wagemaker, D.R. Simon, E.M. Kelder, J. Schoonman, C. Ringpfeil, U. Haake, et al., A kinetic two-phase and equilibrium solid solution in spinel $Li_{4+x}Ti_5O_{12}$, Adv. Mater. 18 (2006) 3169–3173. doi:10.1002/adma.200601636.

[27] S. Scharner, W. Weppner, P. Schmid-Beurmann, Evidence of Two-Phase Formation upon Lithium Insertion into the $Li_{1.33}Ti_{1.67}O_4$ Spinel, J. Electrochem. Soc. 146 (1999) 857. doi:10.1149/1.1391692.

[28] D. Doughty, E.P. Roth, A General Discussion of Li Ion Battery Safety, Electrochem. Soc. Interface. (2012) 37–44. doi:10.1149/2.F03122if.

[29] Y. Wang, W.H. Zhong, Development of electrolytes towards achieving safe and high-performance energy-storage devices: A review, ChemElectroChem. 2 (2015) 22–36. doi:10.1002/celc.201402277.

[30] S.S. Zhang, A review on electrolyte additives for lithium-ion batteries, J. Power Sources. 162 (2006) 1379–1394. doi:10.1016/j.jpowsour.2006.07.074.

[31] Y. Zhu, F. Wang, L. Liu, S. Xiao, Y. Yang, Y. Wu, Cheap glass fiber mats as a matrix of gel polymer electrolytes for lithium ion batteries, Sci. Rep. 3 (2013) 3187. doi:10.1038/srep03187.

[32] C.G. Wu, M.I. Lu, H.J. Chuang, PVdF-HFP/P123 hybrid with mesopores: A new matrix for high-conducting, low-leakage porous polymer electrolyte, Polymer. 46 (2005) 5929–5938. doi:10.1016/j.polymer.2005.05.077.

[33] J. Wen, Y. Yu, C. Chen, A Review on Lithium-Ion Batteries Safety Issues: Existing Problems and Possible Solutions, Mater. Express. 2 (2012) 197–212. doi:10.1166/mex.2012.1075.

[34] K. Xu, Nonaqueous liquid electrolytes for lithium-based rechargeable batteries, Chem. Rev. 104 (2004) 4303–4417. doi:10.1021/cr030203g.

[35] D.R. MacFarlane, N. Tachikawa, M. Forsyth, J.M. Pringle, P.C. Howlett, G.D. Elliott, et al., Energy applications of ionic liquids, Energy Environ. Sci. 7 (2014) 232–250. doi:10.1039/c3ee42099j.

[36] R.A. DiLeo, A.C. Marschilok, K.J. Takeuchi, E.S. Takeuchi, Battery Electrolytes Based on Unsaturated Ring Ionic Liquids: Conductivity and Electrochemical Stability, J. Electrochem. Soc. 160 (2013) A1399-A1405. doi:10.1149/2.045309jes.

[37] M. Pasta, C.D. Wessells, R. a. Huggins, Y. Cui, A high-rate and long cycle life aqueous electrolyte battery for grid-scale energy storage, Nat. Commun. 3 (2012) 1149. doi:10.1038/ncomms2139.

[38] M. Pasta, C.D. Wessells, N. Liu, J. Nelson, M.T. McDowell, R.A. Huggins, et al., Full open-framework batteries for stationary energy storage, Nat. Commun. 5 (2014) 3007. doi:10.1038/ncomms4007.

[39] G. Li, Z. Yang, Y. Jiang, W. Zhang, Y. Huang, Hybrid aqueous battery based on $Na_3V_2(PO_4)_3$/C cathode and zinc anode for potential large-scale energy storage, J. Power Sources. 308 (2016) 52–57. doi:10.1016/j.jpowsour.2016.01.058.

[40] J. Liu, J. Hu, Q. Deng, J. Mo, H. Xie, Z. Liu, et al., Aqueous rechargeable batteries for large-scale energy storage, Isr. J. Chem. 55 (2015) 521–536. doi:10.1002/ijch.201400155.

[41] J.O.G. Posada, A.J.R. Rennie, S.P. Villar, V.L. Martins, J. Marinaccio, A. Barnes, et al., Aqueous batteries as grid scale energy storage solutions, Renew. Sustain. Energy Rev. 68 (2016) 1174–1182. doi:10.1016/j.rser.2016.02.024.

[42] J.F. Whitacre, T. Wiley, S. Shanbhag, Y. Wenzhuo, A. Mohamed, S.E. Chun, et al., An aqueous electrolyte, sodium ion functional, large format energy storage device for stationary applications, J. Power Sources. 213 (2012) 255–264. doi:10.1016/j.jpowsour.2012.04.018.

[43] Q. Wang, P. Ping, X. Zhao, G. Chu, J. Sun, C. Chen, Thermal runaway caused fire and explosion of lithium ion battery, J. Power Sources. 208 (2012) 210–224. doi:10.1016/j.jpowsour.2012.02.038.

[44] D. Lisbona, T. Snee, A review of hazards associated with primary lithium and lithium-ion batteries, Process Saf. Environ. Prot. 89 (2011) 434–442. doi:10.1016/j.psep.2011.06.022.

[45] W. Li, J.R. Dahn, Lithium-Ion Cells with Aqueous Electrolytes, J. Electrochem. Soc. 142 (1995) 1742–1746. doi:10.1149/1.2044187.

[46] A. Dushina, J. Stojadinović, F. La Mantia, Effect of the mass transport limitations on the stability window of electrolytes for metal-ion batteries, Electrochim. Acta. 167 (2015) 262–267. doi:10.1016/j.electacta.2015.03.182.

[47] J.-Y. Luo, W.-J. Cui, P. He, Y.-Y. Xia, Raising the cycling stability of aqueous lithium-ion batteries by eliminating oxygen in the electrolyte., Nat. Chem. 2 (2010) 760–765. doi:10.1038/nchem.763.

[48] L. Suo, O. Borodin, T. Gao, M. Olguin, J. Ho, X. Fan, et al., “Water-in-salt” electrolyte enables high-voltage aqueous lithium-ion chemistries, Science. 350 (2015) 938–943. doi:10.1126/science.aab1595.

[49] Y. Wang, Y. Xia, Hybrid Aqueous Energy Storage Cells Using Activated Carbon and Lithium-Intercalated Compounds, J. Electrochem. Soc. 153 (2006) A450-A456. doi:10.1149/1.2140678.

[50] J. Choi, E. Alvarez, T. A. Arunkumar, A. Manthiram, Proton Insertion into Oxide Cathodes during Chemical Delithiation, Electrochem. Solid-State Lett. 9 (2006) A241-A244. doi:10.1149/1.2184495.

[51] W. Tang, Y. Zhu, Y. Hou, L. Liu, Y. Wu, K.P. Loh, et al., Aqueous rechargeable lithium batteries as an energy storage system of superfast charging, Energy Environ. Sci. 6 (2013) 2093-2104. doi:10.1039/c3ee24249h.

[52] W. Tang, L. Liu, Y. Zhu, H. Sun, Y. Wu, K. Zhu, An aqueous rechargeable lithium battery of excellent rate capability based on a nanocomposite of MoO_3 coated with PPy and $LiMn_2O_4$, Energy Environ. Sci. 5 (2012) 6909-6913. doi:10.1039/c2ee21294c.

[53] Q. Qu, L. Fu, X. Zhan, D. Samuelis, J. Maier, L. Li, et al., Porous $LiMn_2O_4$ as cathode material with high power and excellent cycling for aqueous rechargeable lithium batteries, Energy Environ. Sci. 4 (2011) 3985-3990. doi:10.1039/c0ee00673d.

[54] V. Palomares, M. Casas-Cabanas, E. Castillo-Martínez, M.H. Han, T. Rojo, Update on Na-based battery materials. A growing research path, Energy Environ. Sci. 6 (2013) 2312-2337. doi:10.1039/c3ee41031e.

[55] M.M. Doeff, M.Y. Peng, Y. Ma, L. C. De Jonghe, Orthorhombic Na_xMnO_2 as a Cathode Material for Secondary Sodium and Lithium Polymer Batteries, J. Electrochem. Soc. 141 (1994) L145-L147. doi:10.1149/1.2059323.

[56] M. Pasta, R.Y. Wang, R. Ruffo, R. Qiao, H.-W. Lee, B. Shyam, et al., Manganese–cobalt hexacyanoferrate cathodes for sodium-ion batteries, J. Mater. Chem. A. 4 (2016) 4211–4223. doi:10.1039/C5TA10571D.

[57] H.-W. Lee, R.Y. Wang, M. Pasta, S. Woo Lee, N. Liu, Y. Cui, Manganese hexacyanomanganate open framework as a high-capacity positive electrode material for sodium-ion batteries, Nat. Commun. 5 (2014) 5280. doi:10.1038/ncomms6280.

[58] R.Y. Wang, B. Shyam, K.H. Stone, J.N. Weker, M. Pasta, H.W. Lee, et al., Reversible Multivalent (Monovalent, Divalent, Trivalent) Ion Insertion in Open Framework Materials, Adv. Energy Mater. 5 (2015) 1–10. doi:10.1002/aenm.201401869.

[59] C.D. Wessells, S. V. Peddada, R.A. Huggins, Y. Cui, Nickel hexacyanoferrate nanoparticle electrodes for aqueous sodium and potassium ion batteries, Nano Lett. 11 (2011) 5421–5425. doi:10.1021/nl203193q.

[60] W. Wu, A. Mohamed, J.F. Whitacre, Microwave Synthesized $NaTi_2(PO_4)_3$ as an Aqueous Sodium-Ion Negative Electrode, J. Electrochem. Soc. 160 (2013) A497-A504. doi:10.1149/2.054303jes.

[61] S. Il Park, I. Gocheva, S. Okada, J. Yamaki, Electrochemical Properties of $NaTi_2(PO_4)_3$ Anode for Rechargeable Aqueous Sodium-Ion Batteries, J. Electrochem. Soc. 158 (2011) A1067-A1070. doi:10.1149/1.3611434.

[62] J. Sun, H.W. Lee, M. Pasta, Y. Sun, W. Liu, Y. Li, et al., Carbothermic reduction synthesis of red phosphorus-filled 3D carbon material as a high-capacity anode for sodium ion batteries, Energy Storage Mater. 4 (2016) 130–136. doi:10.1016/j.ensm.2016.04.003.

[63] J. Sun, H.-W. Lee, M. Pasta, H. Yuan, G. Zheng, Y. Sun, et al., A phosphorene-graphene hybrid material as a high-capacity anode for sodium-ion batteries, Nat. Nanotechnol. 10 (2015) 980–985. doi:10.1038/nnano.2015.194.

[64] R. Guduru, J. Icaza, A Brief Review on Multivalent Intercalation Batteries with Aqueous Electrolytes, Nanomaterials. 6 (2016) 41. doi:10.3390/nano6030041.

[65] R. Trócoli, F. La Mantia, An Aqueous Zinc-Ion Battery Based on Copper Hexacyanoferrate, ChemSusChem. 8 (2015) 481–485. doi:10.1002/cssc.201403143.

[66] G. Li, Z. Yang, Y. Jiang, C. Jin, W. Huang, X. Ding, et al., Towards polyvalent ion batteries: A zinc-ion battery based on NASICON structured $Na_3V_2(PO_4)_3$, Nano Energy. 25 (2016) 211–217. doi:10.1016/j.nanoen.2016.04.051.

[67] L. Zhang, L. Chen, X. Zhou, Z. Liu, Towards high-voltage aqueous metal-ion batteries beyond 1.5 V: The zinc/zinc hexacyanoferrate system, Adv. Energy Mater. 5 (2015) 1–5. doi:10.1002/aenm.201400930.

[68] B. Lee, C.S. Yoon, H.R. Lee, K.Y. Chung, B.W. Cho, S.H. Oh, Electrochemically-induced reversible transition from the tunneled to layered polymorphs of manganese dioxide, Sci. Rep. 4 (2014) 6066. doi:10.1038/srep06066.

[69] C. Xu, B. Li, H. Du, F. Kang, Energetic zinc ion chemistry: The rechargeable zinc ion battery, Angew. Chemie - Int. Ed. 51 (2012) 933–935. doi:10.1002/anie.201106307.

[70] C. Yuan, Y. Zhang, Y. Pan, X. Liu, G. Wang, D. Cao, Investigation of the intercalation of polyvalent cations (Mg^{2+}, Zn^{2+}) into λ-MnO_2 for rechargeable aqueous battery, Electrochim. Acta. 116 (2014) 404–412. doi:10.1016/j.electacta.2013.11.090.

[71] C.D. Wessells, R. a Huggins, Y. Cui, Copper hexacyanoferrate battery electrodes with long cycle life and high power, Nat. Commun. 2 (2011) 550. doi:10.1038/ncomms1563.

[72] T. Gupta, A. Kim, S. Phadke, S. Biswas, T. Luong, B.J. Hertzberg, et al., Improving the cycle life of a high-rate, high-potential aqueous dual-ion battery using hyper-dendritic zinc and copper hexacyanoferrate, J. Power Sources. 305 (2016) 22–29. doi:10.1016/j.jpowsour.2015.11.065.

[73] R.S. Nicholson, Theory and Application of Cyclic Voltammetry for Measurement of Electrode Reaction Kinetics, Anal. Chem. 37 (1965) 1351–1355. doi:10.1021/ac60230a016.

[74] E. Madej, S. Klink, W. Schuhmann, E. Ventosa, F. La Mantia, Effect of the specific surface area on thermodynamic and kinetic properties of nanoparticle anatase TiO_2 in lithium-ion batteries, J. Power Sources. 297 (2015) 140–148. doi:10.1016/j.jpowsour.2015.07.079.

[75] P. Verma, P. Maire, P. Novák, A review of the features and analyses of the solid electrolyte interphase in Li-ion batteries, Electrochim. Acta. 55 (2010) 6332–6341. doi:10.1016/j.electacta.2010.05.072.

[76] T. Leung, Information obtained by XRD. http://leung.uwaterloo.ca/MNS/102/Lectures 2014/Lect_22cC_sv.pdf.

[77] D. Chen, S. Indris, M. Schulz, B. Gamer, R. Mönig, In situ scanning electron microscopy on lithium-ion battery electrodes using an ionic liquid, J. Power Sources. 196 (2011) 6382–6387. doi:10.1016/j.jpowsour.2011.04.009.

[78] P. Hovington, M. Dontigny, A. Guerfi, J. Trottier, M. Lagacé, A. Mauger, et al., In situ Scanning electron microscope study and microstructural evolution of nano silicon anode for high energy Li-ion batteries, J. Power Sources. 248 (2014) 457–464. doi:10.1016/j.jpowsour.2013.09.069.

[79] R.J. Hamers, Scanned Probe Microscopies in Chemistry, J. Phys. Chem. 100 (1996) 13103–13120. doi:10.1021/jp960054o.

[80] G. Zampardi, In-situ Analysis of Surface and Bulk Phenomena in Lithium-ion Batteries by means of Scanning Electrochemical Microscopy, Ruhr Universität Bochum, 2015.

[81] A. Bani Hashemi, F. La Mantia, Cell Design for Electrochemical Characterizations of Metal-Ion Batteries in Organic and Aqueous Electrolyte, Anal. Chem. 88 (2016) 7916–7920. doi:10.1021/acs.analchem.6b02138.

[82] K.O. Nayana, T. V. Venkatesha, Synergistic effects of additives on morphology, texture and discharge mechanism of zinc during electrodeposition, J. Electroanal. Chem. 663 (2011) 98–107. doi:10.1016/j.jelechem.2011.10.001.

[83] M.C. Li, L.L. Jiang, W.Q. Zhang, Y.H. Qian, S.Z. Luo, J.N. Shen, Electrodeposition of nanocrystalline zinc from acidic sulfate solutions containing thiourea and benzalacetone as additives, J. Solid State Electrochem. 11 (2007) 549–553. doi:10.1007/s10008-006-0194-z.

[84] S.J. Banik, R. Akolkar, Suppressing Dendrite Growth during Zinc Electrodeposition by PEG-200 Additive, J. Electrochem. Soc. 160 (2013) D519–D523. doi:10.1149/2.040311jes.

[85] S.J. Banik, R. Akolkar, Suppressing Dendritic Growth during Alkaline Zinc Electrodeposition using Polyethylenimine Additive, Electrochim. Acta. 179 (2015) 475–481. doi:10.1016/j.electacta.2014.12.100.

[86] G. Kasiri, R. Trócoli, A. Bani Hashemi, F. La Mantia, An electrochemical investigation of the aging of copper hexacyanoferrate during the operation in zinc-ion batteries, Electrochim. Acta. 222 (2016) 74–83. doi:10.1016/j.electacta.2016.10.155.

[87] L. Zhang, L. Chen, X. Zhou, Z. Liu, Morphology-Dependent Electrochemical Performance of Zinc Hexacyanoferrate Cathode for Zinc-Ion Battery, Sci. Rep. 5 (2016) 18263. doi:10.1038/srep18263.

[88] J. Vetter, M. Holzapfel, A. Wuersig, W. Scheifele, J. Ufheil, P. Novák, In situ study on CO_2 evolution at lithium-ion battery cathodes, J. Power Sources. 159 (2006) 277–281. doi:10.1016/j.jpowsour.2006.04.087.

[89] A. Wuersig, W. Scheifele, P. Novák, CO_2 Gas Evolution on Cathode Materials for Lithium-Ion Batteries, J. Electrochem. Soc. 154 (2007) A449A454. doi:10.1149/1.2712138.

[90] M. He, E. Castel, A. Laumann, G. Nuspl, P. Novák, E.J. Berg, In Situ Gas Analysis of $Li_4Ti_5O_{12}$ Based Electrodes at Elevated Temperatures, J. Electrochem. Soc. 162 (2015) A870–A876. doi:10.1149/2.0311506jes.

[91] D. Aurbach, B. Markovsky, I. Weissman, E. Levi, Y. Ein-Eli, On the correlation between surface chemistry and performance of graphite negative electrodes for Li ion batteries, Electrochim. Acta. 45 (1999) 67–86. doi:10.1016/S0013-4686(99)00194-2.

[92] H. Baltruschat, Differential electrochemical mass spectrometry, J. Am. Soc. Mass Spectrom. 15 (2004) 1693–1706. doi:10.1016/j.jasms.2004.09.011.

[93] Z. Jusys, H. Massong, H. Baltruschat, A New Approach for Simultaneous DEMS and EQCM: Electro-oxidation of Adsorbed CO on Pt and Pt-Ru, J. Electrochem. Soc. 146 (1999) 1093-1908. doi:10.1149/1.1391726.

[94] Z. Jusys, J. Kaiser, R.J. Behm, Composition and activity of high surface area PtRu catalysts towards adsorbed CO and methanol electrooxidation- A DEMS study, Electrochim. Acta. 47 (2002) 3693–3706. doi:10.1016/S0013-4686(02)00339-0.

[95] P.K. Shen, A. C. C. Tseung, Anodic Oxidation of Methanol on Pt/WO_3 in Acidic Media, J. Electrochem. Soc. 141 (1994) 3082-3090. doi:10.1149/1.2059282.

[96] T. Iwasita, E. Pastor, A DEMS and FTIR spectroscopic investigation of adsorbed ethanol on polycrystalline platinum, Electrochim. Acta. 39 (1994) 531–537. doi:10.1016/0013-4686(94)80097-9.

[97] F. La Mantia, F. Rosciano, N. Tran, P. Novák, Quantification of Oxygen Loss from $Li_{1+x}(Ni_{1/3}Mn_{1/3}Co_{1/3})_{1-x}O_2$ at High Potentials by Differential Electrochemical Mass Spectrometry, J. Electrochem. Soc. 156 (2009) A823–A827. doi:Doi 10.1149/1.3205495.

[98] E. Castel, E.J. Berg, M. El Kazzi, P. Novák, C. Villevieille, Differential Electrochemical Mass Spectrometry Study of the Interface of $xLi_2MnO_3\cdot(1-x)LiMO_2$ (M = Ni, Co, and Mn) Material as a Positive Electrode in Li-Ion Batteries, Chem. Mater. 26 (2014) 5051–5057. doi:10.1021/cm502201z.

[99] F. La Mantia, P. Novák, Online Detection of Reductive CO_2 Development at Graphite Electrodes in the 1 M $LiPF_6$, EC:DMC Battery Electrolyte, Electrochem. Solid-State Lett. 11 (2008) A84-A87. doi:10.1149/1.2890756.

[100] Introduction and operating principle of mass spectrometer, https://www.pfeiffer-vacuum.com/en/know-how/mass-spectrometers-and-residual-gas-analysis/introduction-operating-principle/.

[101] P. Novák, R. Imhof, Degradation of mixed carbonates electrolytes on li-ion battery graphite electrodes. An in-situ DEMS study, Proc. Symp. Batter. Portable Appl. Electr. Veh. (1997) 313–320.

[102] R. Imhof, P. Novák, In Situ Investigation of the Electrochemical Reduction of Carbonate Electrolyte Solutions at Graphite Electrodes, Electrochem. Soc. 145 (1998) 1081–1087. doi:10.1149/1.1838420.

[103] R. Imhof, P. Novak, Oxidative electrolyte solvent degradation in lithium-ion batteries - An in situ differential electrochemical mass spectrometry investigation, J. Electrochem. Soc. 146 (1999) 1702–1706. doi:10.1149/1.1391829.

[104] R. Dominko, M. Gaberscek, M. Bele, J. Drofenik, E.M. Skou, A. Würsig, et al., Understanding the Role of Gelatin as a Pretreating Agent for Use in Li-Ion Batteries, J. Electrochem. Soc. 151 (2004) A1058-A1062. doi:10.1149/1.1758813.

[105] M.E. Spahr, T. Palladino, H. Wilhelm, A. Würsig, D. Goers, H. Buqa, et al., Exfoliation of Graphite during Electrochemical Lithium Insertion in Ethylene Carbonate-Containing Electrolytes, J. Electrochem. Soc. 151 (2004) A1383-A1395. doi:10.1149/1.1775224.

[106] H. Buqa, A. Würsig, D. Goers, L.J. Hardwick, M. Holzapfel, P. Novák, et al., Behaviour of highly crystalline graphites in lithium-ion cells with propylene carbonate containing electrolytes, J. Power Sources. 146 (2005) 134–141. doi:10.1016/j.jpowsour.2005.03.106.

[107] J. Li, W. Yao, Y.S. Meng, Y. Yang, Effects of vinyl ethylene carbonate additive on elevated-temperature performance of cathode material in lithium ion batteries, J. Phys. Chem. C. 112 (2008) 12550–12556. doi:10.1021/jp800336n.

[108] B. Zhang, M. Metzger, S. Solchenbach, M. Payne, S. Meini, H.A. Gasteiger, et al., Role of 1,3-propane sultone and vinylene carbonate in solid electrolyte interface formation and gas generation, J. Phys. Chem. C. 119 (2015) 11337–11348. doi:10.1021/acs.jpcc.5b00072.

[109] A. Freiberg, M. Metzger, D. Haering, S. Bretzke, S. Puravankara, T. Nilges, et al., Anodic Decomposition of Trimethylboroxine as Additive for High Voltage Li-Ion Batteries, J. Electrochem. Soc. 161 (2014) A2255–A2261. doi:10.1149/2.0011501jes.

[110] F. La Mantia, F. Rosciano, N. Tran, P. Novák, Direct evidence of oxygen evolution from $Li_{1+x}(Ni_{1/3}Mn_{1/3}Co_{1/3})_{1-x}O_2$ at high potentials, J. Appl. Electrochem. 38 (2008) 893–896. doi:10.1007/s10800-008-9491-9.

[111] P. Lanz, H. Sommer, M. Schulz-Dobrick, P. Novák, Oxygen release from high-energy $xLi_2MnO_3.(1 - X)LiMO_2$ (M = Mn, Ni, Co): Electrochemical, differential electrochemical mass spectrometric, in situ pressure, and in situ temperature characterization, Electrochim. Acta. 93 (2013) 114–119. doi:10.1016/j.electacta.2013.01.105.

[112] H. Wang, E. Rus, T. Sakuraba, J. Kikuchi, Y. Kiya, H.D. Abruña, CO_2 and O_2 evolution at high voltage cathode materials of Li-ion batteries: a differential electrochemical mass spectrometry study, Anal. Chem. 86 (2014) 6197–6201. doi:10.1021/ac403317d.

[113] R. Bernhard, M. Metzger, H.A. Gasteiger, Gas Evolution at Graphite Anodes Depending on Electrolyte Water Content and SEI Quality Studied by On-Line Electrochemical Mass Spectrometry, J. Electrochem. Soc. 162 (2015) A1984–A1989. doi:10.1149/2.0191510jes.

[114] M. Metzger, C. Marino, J. Sicklinger, D. Haering, H.A. Gasteiger, Anodic Oxidation of Conductive Carbon and Ethylene Carbonate in High-Voltage Li-Ion Batteries Quantified by On-Line Electrochemical Mass Spectrometry, J. Electrochem. Soc. 162 (2015) A1123–A1134. doi:10.1149/2.0951506jes.

[115] M. Metzger, B. Strehle, S. Solchenbach, H.A. Gasteiger, Origin of H_2 Evolution in LIBs: H_2O Reduction vs. Electrolyte Oxidation, J. Electrochem. Soc. 163 (2016) A798–A809. doi:10.1149/2.1151605jes.

[116] B. Michalak, B.B. Berkes, H. Sommer, T. Bergfeldt, T. Brezesinski, J. Janek, Gas Evolution in $LiNi_{0.5}Mn_{1.5}O_4$/Graphite Cells Studied In Operando by a Combination of Differential Electrochemical Mass Spectrometry, Neutron Imaging, and Pressure Measurements, Anal. Chem. 88 (2016) 2877–2883. doi:10.1021/acs.analchem.5b04696.

[117] M. He, L. Boulet-Roblin, P. Borel, C. Tessier, P. Novák, C. Villevieille, et al., Effects of Solvent, Lithium Salt, and Temperature on Stability of Carbonate-Based Electrolytes for 5.0 V $LiNi_{0.5}Mn_{1.5}O_4$ Electrodes, J. Electrochem. Soc. 163 (2016) A83–A89. doi:10.1149/2.0201602jes.

[118] O. Wolter, J. Heitbaum, Differential Electrochemical Mass Spectroscopy (DEMS) - a New Method for the Study of Electrode Processes, Berichte der Bunsengesellschaft für phys. Chemie 88 (1984) 2–6. doi:10.1002/bbpc.19840880103

[119] S.J. Ashton, Design, Construction and Research Application of a Differential Electrochemical Mass Spectrometer (DEMS), 2012. doi:10.1007/978-3-642-30550-4.

[120] D. Tegtmeyer, J. Heitbaum, A. Heindrichs, Electrochemical on line mass spectrometry on a rotating electrode inlet system, Berichte Der Bunsengesellschaft Für Phys. Chemie. 93 (1989) 201–206. doi:10.1002/bbpc.19890930218.

[121] T. Hartung, H. Baltruschat, Differential Electrochemical Mass Spectrometry Using Smooth Electrodes: Adsorption and H/D-Exchange Reactions of Benzene on Pt, Langmuir. 6 (1990) 953–957. doi:10.1021/la00095a012.

[122] P. Novák, D. Goers, L. Hardwick, M. Holzapfel, W. Scheifele, J. Ufheil, et al., Advanced in situ characterization methods applied to carbonaceous materials, J. Power Sources. 146 (2005) 15–20. doi:10.1016/j.jpowsour.2005.03.129.

[123] S. Klink, E. Madej, E. Ventosa, A. Lindner, W. Schuhmann, F. La Mantia, The importance of cell geometry for electrochemical impedance spectroscopy in three-electrode lithium ion battery test cells, Electrochem. Commun. 22 (2012) 120–123. doi:10.1016/j.elecom.2012.06.010.

[124] F. La Mantia, C.D. Wessells, H.D. Deshazer, Y. Cui, Reliable reference electrodes for lithium-ion batteries, Electrochem. Commun. 31 (2013) 141–144. doi:10.1016/j.elecom.2013.03.015.

[125] A.J. Bard, L.R. Faulkner, ELECTROCHEMICAL METHODS Fundamentals and Applications, 2nd edition, John Wiley & Sons, Inc, New York, 2001. ISBN:978-0-471-40521-4.

[126] R.C. Snowdon, Electrolytic Precipitation of Zinc, Phys. Chem. 11 (1907) 369–381. doi:10.1021/j150086a003.

[127] K. Boto, Organic additives in zinc electroplating, Electrodepos. Surf. Treat. 3 (1975) 77–95. doi:10.1016/0300-9416(75)90048-6.

[128] Y. Oren, U. Landau, Growth of zinc dendrites in acidic zinc chloride solutions, Electrochim. Acta. 27 (1982) 739–748. doi:10.1016/0013-4686(82)85068-8.

[129] J.O. Bockris, Z. Nagy, A. Damjanovic, On the Deposition and Dissolution of Zinc in Alkaline Solutions, J. Electrochem. Soc. 119 (1972) 285–295. doi:10.1149/1.2404188.

[130] C.-P. Chen, J. Jorné, Fractal Analysis of Zinc Electrodeposition, J. Electrochem. Soc. 137 (1990) 2047-2051. doi:10.1149/1.2086862.

[131] D.P. Barkey, D. Watt, Z. Liu, S. Raber, The Role of Induced Convection in Branched Electrodeposit Morphology Selection, J. Electrochem. Soc. 141 (1994) 1206-1212. doi:10.1149/1.2054897.

[132] M.A. González, R. Trócoli, I. Pavlovic, C. Barriga, F. La Mantia, Layered double hydroxides as a suitable substrate to improve the efficiency of Zn anode in neutral pH Zn-ion batteries, Electrochem. Commun. 68 (2016) 1–4. doi:10.1016/j.elecom.2016.04.006.

[133] P.K. Leung, C. Ponce-De-Leon, C.T.J. Low, F.C. Walsh, Zinc deposition and dissolution in methanesulfonic acid onto a carbon composite electrode as the negative electrode reactions in a hybrid redox flow battery, Electrochim. Acta. 56 (2011) 6536–6546. doi:10.1016/j.electacta.2011.04.111.

[134] C.N. Lungu, M. V. Diudea, M. V. Putz, I.P. Grudziński, Linear and branched PEIs (Polyethylenimines) and their property space, Int. J. Mol. Sci. 17 (2016) 555. doi:10.3390/ijms17040555.

[135] J. Huang, Z. Yang, R. Wang, Z. Zhang, Z. Feng, X. Xie, Zn–Al layered double oxides as high-performance anode materials for zinc-based secondary battery, J. Mater. Chem. A. 3 (2015) 7429–7436. doi:10.1039/C5TA00279F.

[136] B. Yang, Z. Yang, R. Wang, Facile synthesis of novel two-dimensional silver-coated layered double hydroxide nanosheets as advanced anode material for Ni-Zn secondary batteries, J. Power Sources. 251 (2014) 14–19. doi:10.1016/j.jpowsour.2013.11.032.

[137] R. Wang, Z. Yang, B. Yang, T. Wang, Z. Chu, Superior cycle stability and high rate capability of Zn-Al-In-hydrotalcite as negative electrode materials for Ni-Zn secondary batteries, J. Power Sources. 251 (2014) 344–350. doi:10.1016/j.jpowsour.2013.11.071.

[138] Q. Wang, D. O'Hare, Recent advances in the synthesis and application of layered double hydroxide (LDH) nanosheets, Chem. Rev. 112 (2012) 4124–4155. doi:10.1021/cr200434v.

[139] A.I. Khan, D. O'Hare, Intercalation chemistry of layered double hydroxides: recent developments and applications, J. Mater. Chem. 12 (2002) 3191–3198. doi:10.1039/b204076j.

[140] D.G. Evans, R.C.T. Slade, Structural Aspects of Layered Double Hydroxides, Struct. Bond. 119 (2006) 1–87. doi:10.1007/430_005.

[141] http://www.2dsemiconductors.com.

[142] J. Liu, Y. Li, X. Huang, G. Li, Z. Li, Layered double hydroxide nano- and microstructures grown directly on metal substrates and their calcined products for application as Li-ion battery electrodes, Adv. Funct. Mater. 18 (2008) 1448–1458. doi:10.1002/adfm.200701383.

[143] B. Sels, D. De Vos, M. Buntinx, F. Pierard, A. Kirsch-De Mesmaeker, P. Jacobs, Layered double hydroxides exchanged with tungstate as biomimetic catalysts for mild oxidative bromination, Nature. 400 (1999) 855–857. doi:10.1038/23674.

[144] F. Li, Q. Tan, D.G. Evans, X. Duan, Synthesis of carbon nanotubes using a novel catalyst derived from hydrotalcite-like Co-Al layered double hydroxide precursor, Catal. Letters. 99 (2005) 151–156. doi:10.1007/s10562-005-2107-7.

[145] U. Costantino, F. Marmottini, M. Sisani, T. Montanari, G. Ramis, G. Busca, et al., Cu-Zn-Al hydrotalcites as precursors of catalysts for the production of hydrogen from methanol, Solid State Ionics. 176 (2005) 2917–2922. doi:10.1016/j.ssi.2005.09.051.

[146] Q. Wang, J. Luo, Z. Zhong, A. Borgna, CO_2 capture by solid adsorbents and their applications: current status and new trends, Energy Environ. Sci. 4 (2011) 42–55. doi:10.1039/C0EE00064G.

[147] Q. Wang, H.H. Tay, Z. Guo, L. Chen, Y. Liu, J. Chang, et al., Morphology and composition controllable synthesis of Mg-Al-CO_3 hydrotalcites by tuning the synthesis pH and the CO_2 capture capacity, Appl. Clay Sci. 55 (2012) 18–26. doi:10.1016/j.clay.2011.07.024.

[148] L. Lv, J. He, M. Wei, D.G. Evans, X. Duan, Uptake of chloride ion from aqueous solution by calcined layered double hydroxides: Equilibrium and kinetic studies, Water Res. 40 (2006) 735–743. doi:10.1016/j.watres.2005.11.043.

[149] D. Shan, W. Yao, H. Xue, Amperometric detection of glucose with glucose oxidase immobilized in layered double hydroxides, Electroanalysis. 18 (2006) 1485–1491. doi:10.1002/elan.200603545.

[150] L. Desigaux et al., Self-Assembly and Characterization of Layered Double Hydroxide / DNA Hybrids, Nano Latters. 6 (2006) 199–204. doi:10.1021/nl052020a

[151] I.C. Chisem, W. Jones, Ion-exchange properties of lithium aluminium layered double hydroxides, Chem. Mater. 12 (2000) 1990–1994. doi:10.1021/cm0002057

[152] F. Millange, R.I. Walton, L. Lei, D. O'Hare, Efficient Separation of Terephthalate and Phthalate Anions by Selective Ion-Exchange Intercalation in the Layered Double Hydroxide $Ca_2Al(OH)_6.NO3.2H_2O$, 0 (2012) 1–7. doi:10.1179/1743676112Y.0000000045.

[153] M. Gong, Y. Li, H. Zhang, B. Zhang, W. Zhou, J. Feng, et al., Ultrafast high-capacity NiZn battery with NiAlCo-layered double hydroxide, Energy Environ. Sci. 7 (2014) 2025–2032. doi:10.1039/c4ee00317a.

[154] H. Chen, J.M. Wang, T. Pan, H.M. Xiao, J.Q. Zhang, C.N. Cao, Effects of coprecipitated zinc on the structure and electrochemical performance of Ni/Al-layered double hydroxide, Int. J. Hydrogen Energy. 27 (2002) 489–496. doi:10.1016/S0360-3199(01)00175-6.

[155] X. Fan, Z. Yang, R. Wen, B. Yang, W. Long, The application of Zn-Al-hydrotalcite as a novel anodic material for Ni-Zn secondary cells, J. Power Sources. 224 (2013) 80–85. doi:10.1016/j.jpowsour.2012.09.101.

[156] B. Yang, Z. Yang, R. Wang, T. Wang, Layered double hydroxide/carbon nanotubes composite as a high performance anode material for Ni-Zn secondary batteries, Electrochim. Acta. 111 (2013) 581–587. doi:10.1016/j.electacta.2013.08.052.

[157] B. Yang, Z. Yang, Z. Peng, Q. Liao, Effect of silver additive on the electrochemical performance of ZnAl-layered double hydroxide as anode material for nickel-zinc rechargeable batteries, Electrochim. Acta. 132 (2014) 83–90. doi:10.1016/j.electacta.2014.03.126.

[158] T. Wang, Z. Yang, B. Yang, R. Wang, J. Huang, The electrochemical performances of Zn-Sn-Al-hydrotalcites in Zn-Ni secondary cells, J. Power Sources. 257 (2014) 174–180. doi:10.1016/j.jpowsour.2014.02.006.

[159] X. Wen, Z. Yang, X. Xie, Z. Feng, J. Huang, The effects of element Cu on the electrochemical performances of Zinc-Aluminum-hydrotalcites in Zinc/Nickel secondary battery, Electrochim. Acta. 180 (2015) 451–459. doi:10.1016/j.electacta.2015.08.142.

[160] V. Rivers, Layered Double Hydroxides: Synthesis and Post-synthesis Modification, Nova science publishers, Inc., ISBN: 1-59033-060-9.

[161] K. Xu, Electrolytes and Interphases in Li-Ion Batteries and Beyond, Chem. Rev., 2014, 114 (23) 11503–11618. doi:10.1021/cr500003w

[162] S.F. Lux, L. Terborg, O. Hachmöller, T. Placke, H.-W. Meyer, S. Passerini, et al., LiTFSI Stability in Water and Its Possible Use in Aqueous Lithium-Ion Batteries: pH Dependency, Electrochemical Window and Temperature Stability, J. Electrochem. Soc. 160 (2013) A1694–A1700. doi:10.1149/2.039310jes.

[163] R.-S. Kühnel, D. Reber, A. Remhof, R. Figi, D. Bleiner, C. Battaglia, “Water-in-salt” electrolytes enable the use of cost-effective aluminum current collectors for aqueous high-voltage batteries, Chem. Commun. 52 (2016) 10435–10438. doi:10.1039/C6CC03969C.

[164] A. Gambou-Bosca, D. Bélanger, Electrochemical characterization of MnO_2-based composite in the presence of salt-in-water and water-in-salt electrolytes as electrode for electrochemical capacitors, J. Power Sources. 326 (2016) 595–603. doi:10.1016/j.jpowsour.2016.04.088.

[165] K. Xu, C. Wang, Batteries: Widening voltage windows, Nat. Energy. 1 (2016) 16161. doi:10.1038/nenergy.2016.161.

[166] L. Suo, F. Han, X. Fan, H. Liu, K. Xu, C. Wang, “Water-in-Salt” electrolytes enable green and safe Li-ion batteries for large scale electric energy storage applications, J. Mater. Chem. A. 4 (2016) 6639–6644. doi:10.1039/C6TA00451B.

[167] J. Zhao, Y. Li, X. Peng, S. Dong, J. Ma, G. Cui, et al., High-voltage Zn/$LiMn_{0.8}Fe_{0.2}PO_4$ aqueous rechargeable battery by virtue of “water-in-salt” electrolyte, Electrochem. Commun. 69 (2016) 6–10. doi:10.1016/j.elecom.2016.05.014.

[168] L. Smith, B. Dunn, Opening the window for aqueous electrolytes, Science 350 (2015) 918–918. doi:10.1126/science.aad5575.

[169] L. Suo, O. Borodin, W. Sun, X. Fan, C. Yang, F. Wang, et al., Advanced High-Voltage Aqueous Lithium-Ion Battery Enabled by “Water-in-Bisalt” Electrolyte, Angew. Chemie - Int. Ed. 55 (2016) 7136–7141. doi:10.1002/anie.201602397.

[170] L. Coustan, G. Shul, D. Bélanger, Electrochemical behavior of platinum, gold and glassy carbon electrodes in water-in-salt electrolyte, Electrochem. Commun. 77 (2017) 89–92. doi:10.1016/j.elecom.2017.03.001.

[171] C. Wessells, R.A. Huggins, Y. Cui, Recent results on aqueous electrolyte cells, J. Power Sources. 196 (2011) 2884–2888. doi:10.1016/j.jpowsour.2010.10.098.

[172] A. V Cresce, S.M. Russell, D.R. Baker, K.J. Gaskell, K. Xu, In situ and quantitative characterization of solid electrolyte interphases, Nano Lett. 14 (2014) 1405–1412. doi:10.1021/nl404471v.

[173] Y. Zheng, Y. Jiao, Y. Zhu, L.H. Li, Y. Han, Y. Chen, et al., Hydrogen evolution by a metal-free electrocatalyst, Nat. Commun. 5 (2014) 1–8. doi:10.1038/ncomms4783.

[174] J.B. Raoof, R. Ojani, S.A. Esfeden, S.R. Nadimi, Fabrication of bimetallic Cu/Pt nanoparticles modified glassy carbon electrode and its catalytic activity toward hydrogen evolution reaction, Int. J. Hydrogen Energy. 35 (2010) 3937–3944. doi:10.1016/j.ijhydene.2010.02.073.

9. Publications

Parts of this thesis have been published or submitted in the following peer-reviewed scientific journals:

1- A. Bani Hashemi, F. La Mantia, Cell Design for Electrochemical Characterizations of Metal-Ion Batteries in Organic and Aqueous Electrolyte, Anal. Chem. 88 (2016) 7916–7920. doi:10.1021/acs.analchem.6b02138.

2- A. Bani Hashemi, G. Kasiri, F. La Mantia, The Effect of Polyethyleneimine as an Electrolyte Additive on Zinc Electrodeposition Mechanism in Aqueous Zinc-Ion Batteries, submitted to Electrochimica Acta.